Universität Zürich
Physik-Institut

www.physik.unizh.ch

Wissenschaftlicher Jahresbericht

April 2007 - März 2008

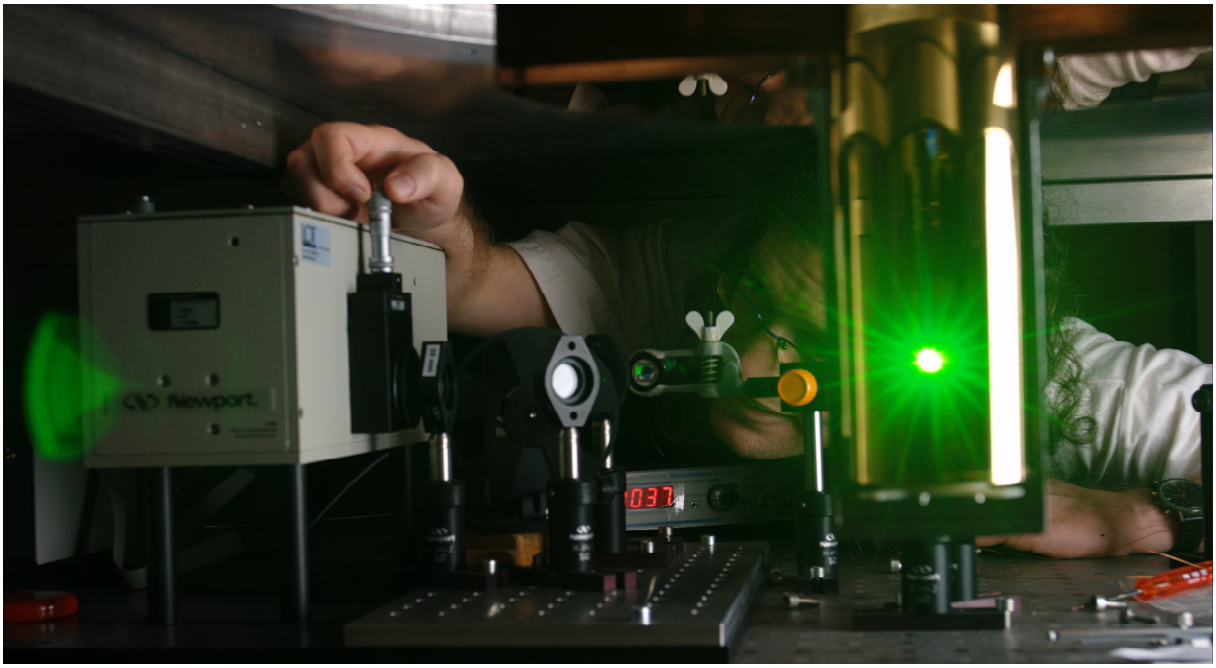

Winterthurerstrasse 190, CH-8057 Zürich/Schweiz

Universität Zürich
Physik-Institut

www.physik.unizh.ch

Wissenschaftlicher Jahresbericht

April 2007 - März 2008

Winterthurerstrasse 190, CH-8057 Zürich/Schweiz

The picture on the front shows Dr. Andreas Engel (group of Prof. Schilling) who is adjusting the optics that is used for testing nano-structured single-photon counters at cryogenic temperatures (see Sec. 11).

Sekretariat	044 635 5721	secret@physik.uzh.ch
Prof. C. Amsler	044 635 5784 022 767 2914	amsler@cern.ch
Prof. L. Baudis	044 635 5777	lbaudis@physik.uzh.ch
Prof. H.-W. Fink	044 635 5801	hwfink@physik.uzh.ch
Prof. H. Keller	044 635 5748	keller@physik.uzh.ch
Prof. J. Osterwalder	044 635 5827	osterwal@physik.uzh.ch
Prof. A. Schilling	044 635 5791	schilling@physik.uzh.ch
Prof. U.D. Straumann	044 635 5768	strauman@physik.uzh.ch

The annual reports are available on the internet: http://www.physik.uzh.ch/reports.html.

Begleitwort

Die experimentelle Forschung am Physik-Institut umfasst ein breites Spektrum verschiedener Gebiete der modernen Physik: von der Untersuchung biologischer Systeme über die Oberflächenphysik und die Physik magnetischer und supraleitender Materialien bis hin zu fundamentalen Wechselwirkungen und Systemen in der Elementarteilchen- und Astroteilchenphysik. Alle Forschungsgruppen arbeiten in einem breit abgestützten internationalen Umfeld. Wie dieser Bericht und die zahlreichen Publikationen belegen, wurden in den verschiedenen Forschungsprojekten auch in diesem Jahr wieder beachtliche Resultate von hohem internationalem Niveau erzielt.

Im August 2007 hat Frau Prof. Dr. Laura Baudis ihre Tätigkeit am Physik-Institut aufgenommen. Prof. Baudis verstärkt und erweitert die Forschungsaktivitäten in der Astroteilchenphysik. Ihr Team sucht nach den Teilchen der *Dunklen Materie* mit einem Flüssigxenon-Detektor am Gran Sasso Untergrundlabor (Italien) und mit Ge- und Si-Detektoren in der Soudan Mine (USA), sowie nach dem neutrinolosen Doppelbetazerfall in angereicherten ^{76}Ge-Detektoren. Die Gruppe betreibt auch einen Flüssigxenon-Detektor am Physik-Institut zur Entwicklung von Lichtdetektoren für die nächste Generation von Experimenten zur Suche nach *Dunkler Materie*.

Im August besuchte das Physik-Institut die Anlagen des CERN in Genf, wo im Sommer 2008 der grösste Beschleuniger der Welt, der *Large Hadron Collider* (LHC), in Betrieb genommen wird. Das Institut ist im Rahmen grosser internationaler Kollaborationen an zwei LHC-Projekten beteiligt, CMS und LHCb. In diesen Experimenten werden das Higgs-Boson und supersymmetrische Teilchen gesucht, bzw. Symmetrien zwischen Materie und Antimaterie untersucht. Unsere Werkstatt hat in Zusammenarbeit mit den Forschungsgruppen wichtige Komponenten für die Detektoren der beiden Experimente entwickelt und fertiggestellt.

Die Forschungsprojekte am Physik-Institut wurden im Berichtsjahr vom *Schweizerischen Nationalfonds* und von Beiträgen aus der *K. Alex Müller Stiftung*, der *Gebert-Rüf Stiftung* und des *Zürcher Universitätsvereins*, sowie durch Drittmittelbeiträge des *Paul Scherrer Institutes*, und des *IBM Forschungslaboratoriums Rüschlikon* unterstützt. Das Physik-Institut ist am Nationalen Forschungskompetenzzentrum (NCCR) MaNEP (*Materials with Novel Electronic Properties*) beteiligt. Es stellt gegenwärtig den Vorsitzenden des *Swiss Institute of Particle Physics* (CHIPP) und den wissenschaftlichen Delegierten der Schweiz im CERN-Rat. Drei Forschungsgruppen des Physik-Instituts sind an EU-Projekten beteiligt, nämlich auf dem Gebiet der Nanowissenschaften an den beiden Projekten *Nanomesh Boron Nitride Nanomesh as a Scaffold for Nanocatalysts, Nanomagnets and Functional Surfaces* und *Obtaining Atomically Resolved Structural Information on Individual Bio-Molecules using Electron Holography*, sowie auf dem Gebiet der kondensierten Materie am Projekt *Controlling Mesoscopic Phase Separation*. Die beiden ersten EU-Projekte werden von Mitgliedern des Physik-Instituts geleitet.

Ich danke allen Mitarbeiterinnen und Mitarbeitern, die mit grossem Engagement zu den vielen Erfolgen im Berichtsjahr beigetragen haben, sowie den forschungsfördernden Institutionen für ihre nachhaltige Unterstützung.

Zürich, im Mai
Prof. Dr. Hugo Keller

Mitarbeiter

Wissenschaftliches Personal

Enver	Alagöz	CMS
Yves	Allkofer	DIRAC
Prof. Claude	Amsler	ArDM, DIRAC, CMS
Sebastian	Arrenberg	CDMS
Ali	Askin	XENON
Holger	Bartolf	PTM
Prof. Laura	Baudis	CDMS, GERDA, XENON
Simon	Berner	Oberflächenphysik
Dr. Roland	Bernet	LHCb
Vittorio	Boccone	ArDM
Tobias	Bruch	CDMS
Thomas	Brugger	Oberflächenphysik
Angela	Büchler	LHCb
Dr. Vincenzo	Chiochia	CMS
Nicola	Chiapolini	LHCb
Raffaele	Dell'Amore	PTM
Jan-Hugo	Dil	Oberflächenphysik
Dr. Andreas	Engel	PTM
Conrad	Escher	Bio-Physik
Dr. Dmitry	Eshchenko	Supraleitung & Magnetismus
Dr. Alfredo	Ferella	GERDA, XENON
Prof. Hans-Werner	Fink	Bio-Physik
Francis	Froborg	GERDA
Dr. Carine	Galli Marxer	Oberflächenphysik
Matthias	Germann	Bio-Physik
Luis	Gómez	PTM
Prof. Thomas	Greber	Oberflächenphysik
Marijke	Haffke	XENON
Viktor	Hangartner	LHCb
Dr. Matthias	Hengsberger	Oberflächenphysik
Stefan	Heule	UCN
Sosuke	Horikawa	DIRAC
Prof. Hugo	Keller	Supraleitung & Magnetismus
Dr. Rustem	Khasanov	Supraleitung & Magnetismus
Alexander	Kish	XENON
Andreas	Knecht	UCN
Fabio	La Mattina	Supraleitung & Magnetismus
Dr. Tatiana	Latychevskaia	Bio-Physik
Dominik	Leuenberger	Oberflächenphysik
Jean-Nicolas	Longchamp	Bio-Physik
Alexander	Maisuradze	Supraleitung & Magnetismus
Dr. Mihael	Mali	Supraleitung & Magnetismus
Thomas	Mattle	Oberflächenphysik

Wissenschaftliches Personal (cont)

Aaron	Manalaysay	XENON
Fabian	Meier	Oberflächenphysik
Martin	Morscher	Oberflächenphysik
Prof. K. Alex	Müller	Supraleitung & Magnetismus
Dr. Katharina	Müller	H1
Krzysztof	Nowak	H1
Prof. Jürg	Osterwalder	Oberflächenphysik
Dr. Christian	Regenfus	CMS, ArDM, DIRAC
Mark	Reibelt	PTM
Dr. Peter	Robmann	CMS, H1, $\pi \to e\nu$
Tanja	Rommerskirchen	CMS
Dr. Josef	Roos	Supraleitung & Magnetismus
Rosmarie	Rössel	Studienberatung
Silvan	Roth	Oberflächenphysik
Christophe	Salzmann	LHCb
Dr. Roberto	Santorelli	GERDA, XENON
Prof. Andreas	Schilling	PTM
Jeanette	Schmidlin	Oberflächenphysik
Alexander	Schmidt	CMS
Carsten	Schmitz	H1
Prof. Toni	Schneider	Supraleitung & Magnetismus
Stefan	Siegrist	PTM
Dr. Thomas	Speer	CMS
Dr. Olaf	Steinkamp	LHCb
Elvira	Steinwand	Bio-Physik
Simon	Strässle	Supraleitung & Magnetismus
Prof. Ulrich	Straumann	H1, LHCb, $\pi \to e\nu$, UCN
Michal	Tarka	CDMS, GERDA
Prof. Peter	Truöl	H1, $\pi \to e\nu$
Dimitrios	Tsirigkas	CMS
Dr. Eirini	Tziaferi	XENON
Dr. Andries	van der Schaaf	$\pi \to e\nu$
Dr. Jeroen	van Tilburg	LHCb
Dr. Achim	Vollhardt	Elektronik, LHCb
Dimitro	Volyanskyy	LHCb
Andreas	Wenger	DØ, LHCb
Stephen	Weyeneth	Supraleitung & Magnetismus
Lotte	Wilke	CMS
Bastian M.	Wojek	Supraleitung & Magnetismus
Dr. Hirofumi	Yanagisawa	Oberflächenphysik

Technisches und administratives Personal

Cornel	Andreoli	Bio-Physik
Eva	Baby	Sekretariat
Kurt	Bösiger	Werkstatt
Tiziano	Crudeli	Zeichnen
Walter	Fässler	Dokumentation, Elektronik
Omid	Fardin	Werkstatt
Ruth	Halter	Sekretariat
Claudia	Heger	Sekretariat
Martin	Klöckner	Oberflächenphysik
Bruno	Lussi	Werkstatt
Reto	Maier	Werkstatt
Hanspeter	Meyer	Elektronik, CMS
Tizian	Naterop	Werkstatt
Lucien	Pauli	Vorlesungsbetrieb
Rolf	Reichen	Werkstatt
Jacky	Rochet	CMS, ArDM, DIRAC
Monika	Röllin	Sekretariat
Marcel	Schaffner	Werkstatt
Jacqueline	Schenk	Sekretariat
Silvio	Scherr	Werkstatt
Jürg	Seiler	Vorlesungsbetrieb
Peter	Soland	Elektronik
Stefan	Steiner	CAD, CMS, LHCb

Contents

1 Search for dark matter with liquid argon

C. Amsler, V. Boccone, H. Cabrera[1], S. Horikawa, C. Regenfus, J. Rochet, and M. Thomann[2]

In collaboration with:
CIEMAT, ETHZ, Soltan Institute (Warsaw), Universities of Granada and Sheffield

(ArDM Collaboration)

We are building a one ton liquid argon time projection chamber to detect recoil nuclei from the scattering of Weak Interacting Massive Particles. WIMPs (in particular the lightest supersymmetric particle, the neutralino), are among the favorite candidates for the missing non-baryonic matter in the universe. Details on the experiment can be found in our previous annual reports.

In 2007 the Zurich group concluded its laboratory development program for the light readout system and the ArDM collaboration started to assemble the full-scale one ton apparatus. A sketch of the detector is shown in Fig. 1.1. The working principle is as follows: in liquid argon a WIMP collision leading to 30 keV nuclear recoils produces about 400 VUV (128 nm) photons, together with a few free electrons. The latter are drifted in a strong vertical electric field and are detected in the gas phase by a large electron multiplier above the surface of the liquid, while the VUV scintillation light is shifted into blue light by a wavelength shifter (WLS) and detected by cryogenic photomultipliers at the bottom of the vessel.

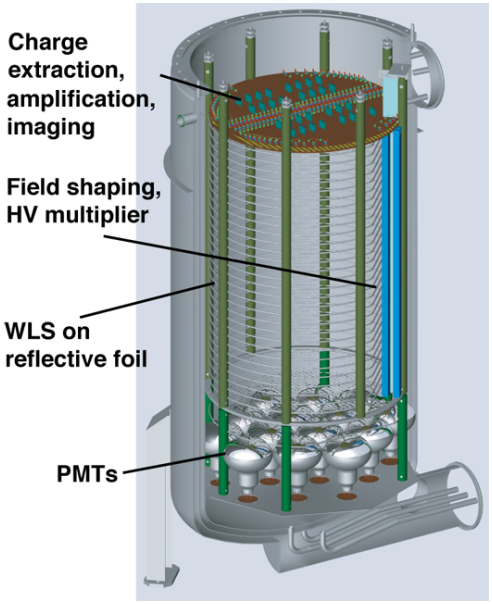

Figure 1.1: Sketch of the ArDM detector.

From extensive tests performed by our group we concluded that the highest light collection efficiency would be achieved with WLSs made of a 254 μ thick Teflon fabric (Tetratex) coated with $\approx$1 mg/cm^2 tetraphenyl butadiene (TPB) (1) (see below). We constructed a large evaporation chamber capable of coating a 1.4 m long and 0.3 m wide sheet of Tetratex. Twelve sheets were coated to cover the cylindrical side walls inside the electric field shapers (Fig. 1.2). The light detection system consists of fourteen 8" hemispherical PMTs in a staggered arrangement at the bottom of the vessel (Fig. 1.3. We have investigated PMTs for their functionality and quantum efficiency at low temperature. The best result was obtained with Hamamatsu PMTs (R5912-MOD) manufactured with Pt-underlay. A light but sufficiently strong mechanical support was constructed to withstand the buoyant force ($\approx$ 1kN) acting on the PMTs in liquid argon. Eight PMTs were installed for readout tests. The PMT glass was coated with a thin wavelength shifting layer of a transparent TPB-paraloid compound to increase the VUV light

[1]Master student
[2]Bachelor student

yield. Vacuum feedthroughs, cables for the high voltage and signal lines were installed, as well as parts of the data acquisition system.

The ratio of primary scintillation light to ionization charge collected after a given drifttime in an external electric field is different for nuclear recoils and minimum ionizing particles, being very high for the former, due to quenching. This provides the main discrimination between WIMPs and background. In liquid, on the other hand, the VUV photons are produced by ionization from the spin singlet and triplet states of the excited dimer A_2^* which have different lifetimes (τ = 7 ns, resp. 1.6 μs in liquid). These states are populated differently according to the excitation process: for heavy ionization (such as nuclear recoils) the singlet dominates, while for minimum ionizing particles (such as electrons) the triplet dominates. Hence the discrimination of decay time allows a further separation between WIMP induced recoils and background from γ or electrons.

A considerable effort was devoted in 2007 to measure the mean decay lives of the fast (12 ns) and slow (3.2 μs) components of argon luminescence in argon gas at NTP (which are different from liquid) and to determine the population ratio between the slow and fast components. We used a ^{210}Pb-source emitting 5.3 MeV α-particles and 1.2 MeV electrons. This work initiated in ref. (2) is the subject of a recent publication (3). Figure 1.4 shows for instance that the mean life of the slow component strongly depends on argon purity.

We have also determined that the fast decaying component in gaseous argon at NTP stems from UV-light from the so-called (4) third continuum above 160 nm, while the slow component is due to 128 nm photons from the second continuum. This appears to be in contrast to liquid in which both components are due to 128 nm VUV-photons. The measurement was performed by inserting a thin quartz plate in

Figure 1.2: HV divider, WLS foils and photomultipliers under UV illumination.

Figure 1.3: PMT support structure built by our group with three of the fourteen 8" (Hamamatsu R5912-MOD) PMTs.

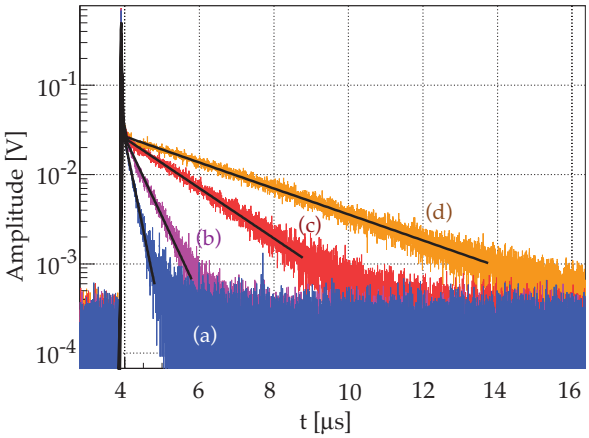

Figure 1.4: Time distribution from an α-source in gaseous argon as a function of contaminating residual air pressure for 10^{-2} (a), 10^{-3} (b), 2.3×10^{-4} (c) and 10^{-5} mbar (d) (from [3]).

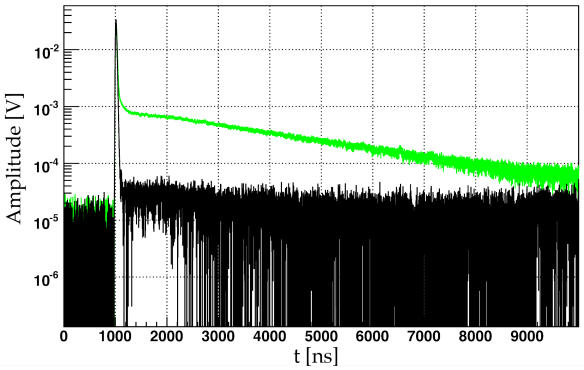

Figure 1.5:
Time distribution without (green) and with (black) absorbing quartz plate.

front of the PMT photocathode to absorb radiation below 200 nm. Figure 1.5 shows that the fast component is not affected, while the slow component is absorbed (3).

Similar measurements were made in liquid argon (5). In liquid we noticed that the light yield was slowly decreasing with time after liquefaction. However, the decay time of the second component (τ = 1.6 μs) was not affected. The origin of this effect is not understood yet, but could be interpreted either as due to the slow cooling of the dynodes (poor heat conductance of the PMT leads) or due to impurities which are absorbing the UV-light.

We also measured the light yield dependence on the WLS thickness of evaporated specular reflectors foils. The measurements were made with a small cell containing gaseous argon at atmospheric pressure. Two materials were selected, Tetratex and ESR-foils from 3M, and the optimum thickness of the TPB layer on the reflector was determined experimentally (1). The best conversion efficiency, uniformity and reproducibility were achieved by evaporating TPB on the reflector. Several disks of ESR foils (diameter 70 mm) were covered with TPB layers of different thicknesses. The TPB thickness was determined by weighing the disks before and after evaporation. The increase in brightness with TPB thickness is apparent under UV illumination (300 nm) (Fig. 1.6). The response to 128 nm light was determined using scintillation light from gaseous argon and an α-source. The light yield of the slow component (3.2 μs in gas) is shown in Fig. 1.7 as a function of thickness. The data are consistent with a satura-

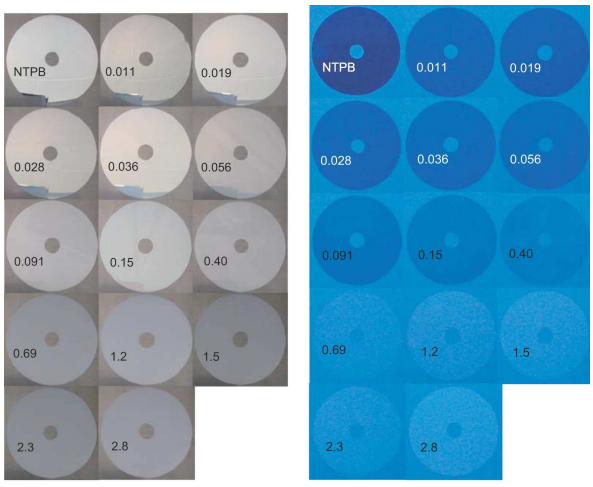

Figure 1.6: Disks of ESR-foils covered with TPB under ambient and UV light.

tion of VUV conversion efficiency above 1 mg $\cdot$ cm^{-2}. Tetratex coated with 1 mg $\cdot$ cm^{-2} TPB was finally chosen for the one ton detector.

As mentioned above, impurities in argon strongly reduce the lifetime of the slow scintillation component. We have therefore built a liquid-argon purity monitor based on the measurement of the lifetime of the triplet excimer state. A small liquid argon cell containing a ^{210}Pb-source emitting both α and β is viewed by a photomultiplier with MgF_2 window and CsTe photocathode which is sensitive to 128 μm VUV-photons (quantum efficiency $\sim$ 20%). Figure 1.8 shows the correlation between the fraction R of the fast ($<$ 50 ns) scintillation component and the total pulse height. The α-signal is clearly separated from the β-signal and noise. The decay time distribution is shown in Fig. 1.9 for α-particles. A simple exponential fit leads to a mean life of $\sim$ 470 ns for the slow component (while 1.6 μs is expected) and hence indicates a sizeable impurity contamination in the liquid.

The ArDM detector is being assembled at CERN for preliminary readout measurements. We envisage to first install the detector in one of the former LEP pits (OPAL area) for background studies, before moving to a deep underground site.

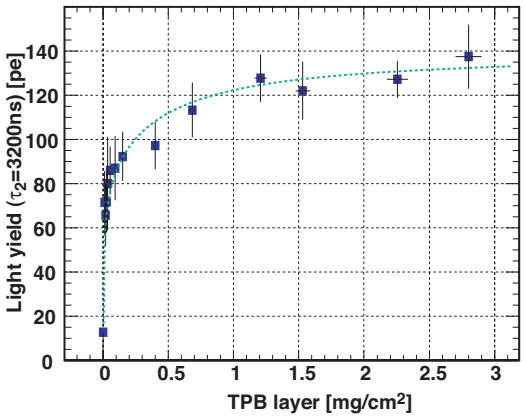

Figure 1.7: Number of photoelectrons (pe) as a function of WLS thickness.

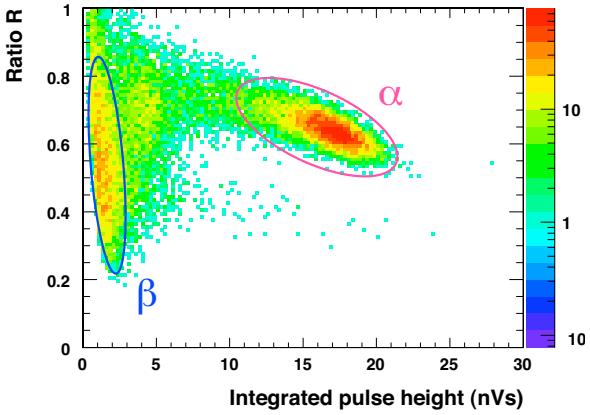

Figure 1.8: Ratio of the fast ($<$50 ns) signal to the total signal in liquid argon vs. total signal in the purity monitor.

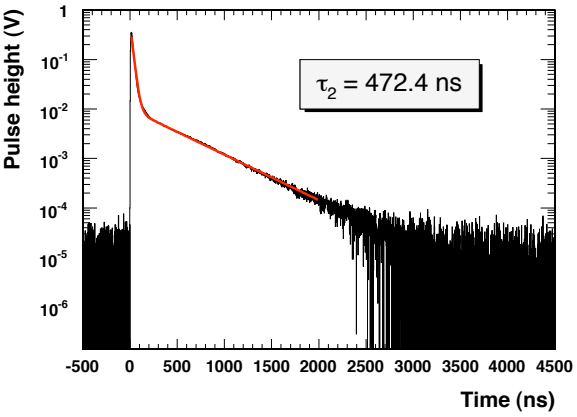

Figure 1.9: Decay time distribution for α-particles.

[1] H. Cabrera, Master Thesis, Universität Zürich (2007).

[2] A. Büchler, Bachelor Thesis, Universität Zürich (2006).

[3] C. Amsler *et al.*, Journal of Instrumentation **3** (2008) P02001.

[4] W. Krötz *et al.*, Phys. Rev. **A 43** (1991) 6089.

[5] M. Thomann, Bachelor Thesis, Universität Zürich (2008).

2 Search for Cold Dark Matter with CDMS-II

S. Arrenberg, L. Baudis, T. Bruch, M. Tarka

In collaboration with:
Brown, California Inst. of Technology, Case Western, FNAL, BNL, MIT, Queen's, Santa Clara, Stanford, Syracuse, Berkeley, Santa Barbara, Denver, Gainesville, Minneapolis

(CDMS-II Collaboration)

The Cryogenic Dark Matter Search (CDMS) experiment searches for Weakly Interacting Massive Particles (WIMPs), which are leading candidates for the non-baryonic matter in our Universe. The experiment has been operating successfully in a low-background facility at the Soudan Underground Laboratory since October 2003, and has delivered the world's best limits on the direct detection of WIMPs (1; 2).
At the experiment's core are Z(depth)-sensitive ionization and phonon-mediated (ZIP) detectors, which are cylindrical high-purity Ge (250 g) or Si (100 g) crystals kept at a base temperature of ∼40 mK. A particle interacting in a ZIP detector causes an electron or a nuclear recoil, depositing its energy into the crystal through charge excitations (electron-hole pairs) and lattice vibrations (phonons). The charge excitations are drifted in a low field (3V/cm) and collected with electrodes on the two sides of the ZIP detector. The phonon signal is detected by quasiparticle-trap electrothermal-feedback transition-edge sensors photolithographically patterned onto one of the crystal faces. Nuclear recoils produce less electron-ion pairs than electron recoils, thus the ionization yield, defined as $y = E_{charge}/E_{recoil}$, is smaller for nuclear recoils ($y \sim 0.3$ for Ge and ~ 0.25 for Si) than for electron recoils ($y = 1$) of the same energy. It provides the technique to reject the electron-recoil events which produce most of the background. A picture of the inner CDMS cryostat is shown in Fig. 2.1. A detailed description of the CDMS apparatus and shield is given in (2).

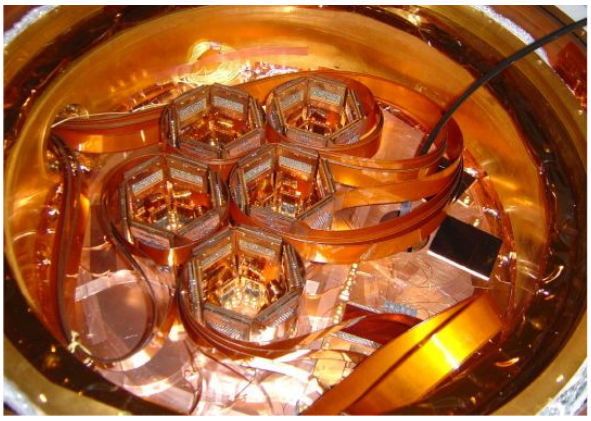

Figure 2.1: Open CDMS copper cryostat, showing the top of the 5 tower structures containing the field efect transistor cards for the ionization and the SQUID cards for the phonon readout, as well as the Cu kapton striplines which are used to carry the signals to room temperatures. Each tower contains 6 ZIP detectors (not seen here).

2.1 Analysis of the CDMS WIMP search runs

The CDMS-II experiment is operating five towers (19 Ge and 11 Si ZIP detectors) with 4.5 kg of Ge and 1.1 kg of Si, in stable WIMP search mode since October 2006. The data acquired between October 2006 and July 2007, yielding an exposure of 121.3 kd d in Ge, have been analyzed and the results were recently submitted (3). A blind analysis resulted in zero observed events, the deduced upper limit on WIMP-nucleon spin-independent cross section is 6.6×10^{-44}cm^2 (4.6×10^{-44}cm^2

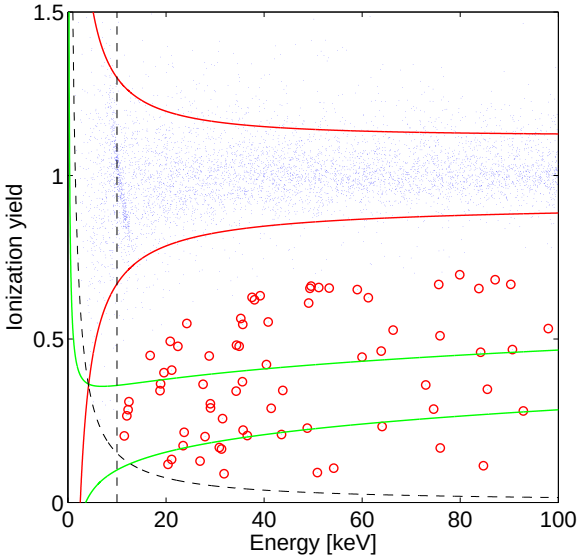

Figure 2.2: Low background data for one ZIP in the ionization yield - energy plane. Electromagnetic background events lie in the (red/upper) electron recoil band, whereas signal events are expected in the (green/lower) nuclear recoil band. The signal region is populated with low yield events (red circles), which are rejected by the surface event timing cut.

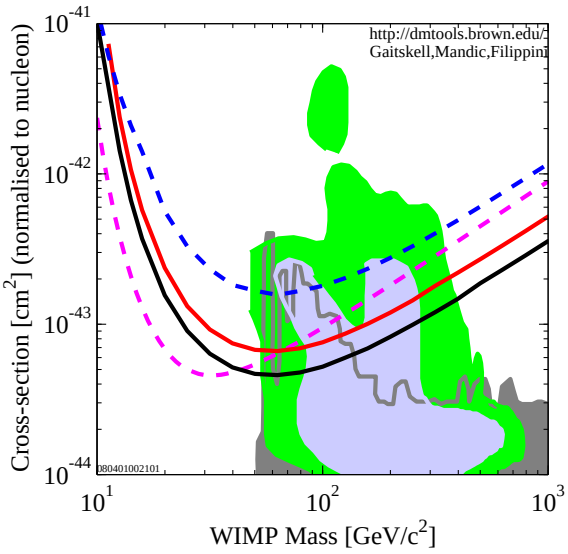

Figure 2.3: Upper limits (90% C.L.) on the spin-independent WIMP-nucleon cross section versus WIMP mass. The upper (blue/dash-dot) curve is a result of a re-analysis of the previous CDMS-II data. The thick (intermediate/red) curve represents the limit derived from the current CDMS-II run. The thick (lower/black) is the combined CDMS-II limit. For comparison the exclusion limit obtained by the XENON10 experiment (orange/dashed) is shown. The filled regions indicate parameter ranges expected from different SUSY models.

when combined with previous CDMS Soudan data) for a WIMP mass of 60 GeV/cm^2 (3). This limit improves upon the sensitivity of XENON10 for WIMP masses above 42 GeV/cm^2, providing the current best sensitivity for dark matter WIMPs above this mass (see also Figs. 2.2 and 2.3). Our group was strongly involved in the analysis of this run (development and tests of analysis cuts, MC simulations of calibration sources and comparison with data, as well as gamma and neutron background studies), and in the operation of the experiment at the Soudan Lab. At the time of this writing, we have accumulated more than an additional $\sim$330 live days, the analysis of this data is ongoing. The expected sensitivity is 2.1×10^{-44}cm^2 for spin-independent WIMP-nucleon cross section at 60 GeV/c^2 WIMP mass by the end of 2008.

The main resposibility of our group are background studies, with focus in understanding the origin and minimizing the sources of background in the ZIP detectors. We performed Monte Carlo simulations of the gamma, beta and internal neutron background using the GEANT4 toolkit, considering contaminations from the $^{238}_{92}$U and $^{232}_{90}$Th chains and decays of $^{60}_{27}$Co and $^{40}_{19}$K in the various materials. The Monte Carlo results were normalized with previously measured activities of these materials. In the case of the gamma background, the predictions could be directly compared to the five tower data, showing an excellent agreement and leaving no unidentifed spectral lines which would indicate an unknown contamination.

The electromagnetic background can be dis-

tinguished from a WIMP signal based on the ionization yield parameter, yielding the two well separated bands shown in Fig. 2.2. However, events interacting in the first few microns of the crystal have incomplete charge collection and thus a suppresed ionization yield. Such events can potentially leak into the signal region (given by the lower band) mimicking a WIMP nuclear recoil. These so called low-yield events are identifed as the population below the electron recoil band. Our studies give an average low-yield event rate of 3×10^{-3} counts/(day kg keV) for the current run, with an ambient gamma induced component in the range of 20%. The remaining 80% comes from ^{210}Pb decays on the surface of the detectors. To discriminate between low-yield and nuclear recoil events the timing properties of the phonon signals are used.

Neutrons with MeV energies cause nuclear recoil events identical to the expected signal, however they multiply scatter providing a method to distinguish them from WIMPs. We calculated the neutron spectra and fluxes from $(\alpha, n)-$ and spontaneous fission (SF) reactions for the inner CDMS components (Cu cryostat and ZIP housings) and for the PE and Pb shields. After normalization, the spectra were used in Monte Carlo simulations as neutron-emission probability functions to estimate the induced rates in the ZIP detectors. We expect to detect a total of $\sim 3.1 \cdot 10^{-2}$ ($\sim 1.5 \cdot 10^{-2}$) single neutron recoils in Ge (Si) from internal neutrons for the currently analyzed CDMS exposure (121.3 kg d). The inferred mean single to multiple event ratio is $\sim$1.64.

2.2 Limits on Kaluza-Klein dark matter

In theories with flat universal extra dimensions (UED) (4), two well studied dark matter candidate are $\gamma_{(1)}$, the Kaluza-Klein (KK) photon and Z_1, the KK-Z boson. Their thermal relic density has been calculated (5; 6), including all the relevant coannihilation processes. It is compatible with WMAP results for a wide range of particle masses, and depends for instance on the masses of the first level KK-quarks (5; 6). We have investigated the direct detection of KK dark matter candidates in five and six dimensional UED models. We have compared obtained limits with theoretical predictions for the cross sections and WIMP-nucleon couplings, including both spin-independent and spin-dependent interactions. We have also compute limits on two parameters of the theory, the Higgs mass and the degeneracy parameter Δ_{q_1} defined by

$$\Delta_{q_1} \equiv \frac{m_{q^{(1)}} - m_{L^{(1)}}}{m_{L^{(1)}}} \ ,$$

which imposes a relation between the assumed to be totally degenerate level one quark masses $m_{q^{(1)}}$ and the mass of the lightest Kaluza-Klein mode $m_{L^{(1)}}$. We were particularly interested in the region of small mass splittings Δ_{q_1}, which is problematic for collider searches, but promising for direct detection.

In Fig. 2.4 we present a combination of results for the case of (a) γ_1 and (b) Z_1 lightest KK-mode in the five dimensional UED. The two most relevant parameters are the mass (m_{γ_1} or m_{Z_1}), and the mass splitting Δ_{q_1}. For simplicity, we assume that the $SU(2)_W$-doublet KK quarks and the $SU(2)_W$-singlet KK quarks are degenerate, so that there is a single mass splitting parameter. Experiments such as CDMS-II and XENON10 can already contrain part of the parameter space (especially for small mass splitting1), while future, 1 ton scale experiments could contrain a significant part of the cosmologically relevant parameter space. A detailed publication with these and further results is in preparation (8).

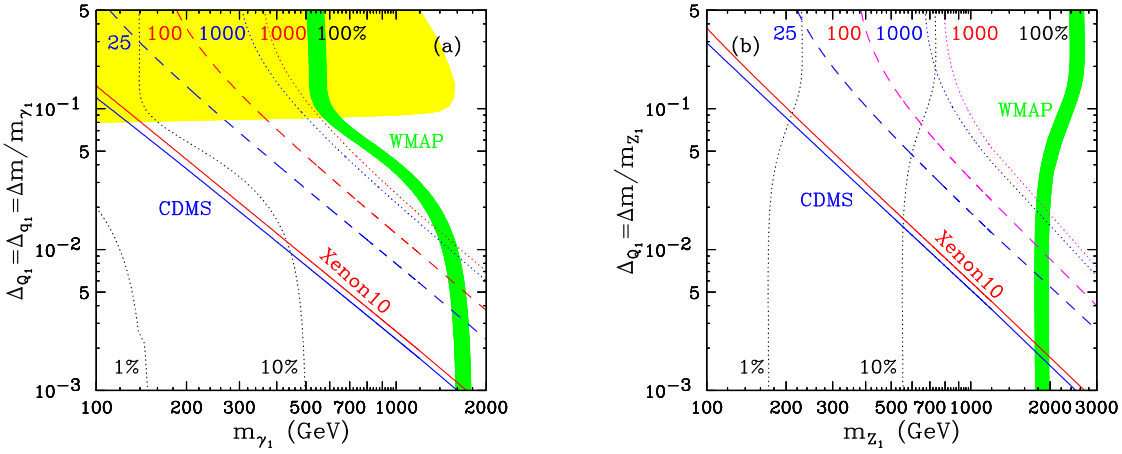

Figure 2.4: Combined plot of the direct detection limits on the spin-independent cross section, the limit from the relic abundance and the LHC reach for (a) γ_1 and (b) Z_1, in the parameter plane of the lightest KK-mode mass and the mass splitting Δ_{q_1}. The SM Higgs mass is m_h=120 GeV. The green band shows the WMAP range for the relic density, 0.1037$< \Omega_{CDM}h^2 <$ 0.1161, accounting for 100% of the dark matter. The two black dotted lines show 10% and 1%, respectively. The blue (red) solid line labeled CDMS (XENON10) show the CDMS (XENON10) limit and the dashed and dotted lines represent projected limits for the larger detectors. In the case of γ_1, 1 ton scale experiments rule out most of parameter space while there is little parameter space left in the case of Z_1. The yellow region in the case of γ_1 shows the parameter space that could be covered by the collider search in $4\ell + \not{E}_T$ channel at the LHC with a luminosity of 100 fb^{-1} [7].

[1] D. Akerib *et al.* (CDMS Collaboration), Phys. Rev. Lett. 96 (2006) 011302.

[2] D. Akerib *et al.* (CDMS Collaboration), *Phys.Rev.* D **72** (2005) 052009.

[3] D. Akerib *et al.* (CDMS Collaboration), submitted to PRL.

[4] T. Appelquist, H.-C. Cheng and B.A. Dobrescu, Phys. Rev. D **64** (2001) 035002.

[5] G. Servant and T. Tait, Nucl.Phys. B **650** (2003) 391-419.

[6] K. Kong and K.T. Matchev, JHEP **0601** (2006) 038.

[7] H.-C. Cheng, J.L. Feng and K.T. Matchev, Phys.Rev.Lett. **89** (2002) 211301.

[8] S. Arrenberg, L. Baudis, K.C. Kong, K. Matchev, J. Yoo, in preparation.

3 Search for the Neutrinoless Double Beta Decay with GERDA

L. Baudis, A. Ferella, F. Froborg, R. Santorelli, M. Tarka

In collaboration with: LNGS, Cracow, Dresden, Dubna, Geel, Heidelberg, Germany, Milano, INR Russian Academy of Sciences, Moscow, Kurchatov Institute, München, Padova, Tübingen

(GERDA Collaboration)

One of the most interesting questions in particle physics is related to the absolute mass and nature of neutrinos. While we have strong evidence from solar, atmospheric, reactor and accelerator neutrino experiments that neutrinos have a finite mass, these experiments only measure mass differences, Δm^2=$|m_2^2 - m_1^2|$. Oscillation experiments have established a lower limit for one of the neutrino masses, $\sqrt{\Delta m^2_{atm}} \simeq$0.05 eV, but can not determine the absolute scale of the mass eigenstates. Moreover, the results do not depend on the charge conjugation properties of neutrinos, thus we don't yet know if they are Dirac or Majorana particles. The observation of neutrinoless double beta decay would prove that neutrinos are Majorana particles, that lepton number is violated in Nature and would give us information on the so-called effective Majorana neutrino mass, m_{ee} (1). Current experimental limits on m_{ee} are of the order $m_{ee} \leq 0.3 - 1.0$ eV, with the most stringent upper limits coming from the former Heidelberg-Moscow (2) and IGEX (3) experiments, which searched for the neutrinoless double beta decay with enriched ^{76}Ge detectors.

GERDA is a new experiment to search for the neutrinoless double beta decay in enriched ^{76}Ge detectors in Hall A of the Gran Sasso Underground Laboratory (LNGS) in Italy. The aim of GERDA Phase I and II is to reach a sensitivity for the effective Majorana neutrino mass of 270 meV and 110 meV, respectively. This is achieved by operating bare HPGe crystals in a large volume (70 m^3) of liquid argon (LAr), which serves as a passive shield against the external radioactivity and is in addition surrounded by a water shield instrumented with light detectors.

3.1 Status of the GERDA experiment

GERDA Phase I will operate 17.9 kg of existing enriched ^{76}Ge detectors, which belonged to the former Heidelberg-Moscow and IGEX collaborations. The double walled, stainless steel cryostat holding the LAr has been delivered at LNGS on March 5, 2008. The water tank (10 m high, and 10 m diameter) will be installed before September 2008, when the installation of the clean room on top of the tank, and of the muon veto will start. Installation of the gas handling system, and of the detector holders will be finalized in April 2009. It is planned to start taking Phase I science data by early summer 2009. However, the phase I enriched Ge detectors will already be operated in the LArGe Facility in the GERDA detector lab at LNGS starting in mid 2008. Apart from providing first tests of these detectors in an ultra-low-background facility, first science data will also be taken. For GERDA Phase I, our group is responsible for the calibration system: calibration sources, collimators, hardware for insertion/parking in the cryostat, Monte Carlo simulations of possible configurations, source strengths and efficiency of pulse shape discrimination.

Figure 3.1 shows the GERDA cryostat shortly after its arrival at LNGS. The cryostat and infrastructure being built for Phase I will also be used in Phase II. An additional 14 enriched HPGe

Figure 3.1:
The GERDA stainless steel cryostat shortly after its arrival at LNGS in March 2008.

detectors are planned for this second phase. At present, the GERDA collaboration is in the possession of 37.5 kg of enriched Ge material (in the form of GeO_2), with an additional 20 kg of enriched material needed. This material will be cleaned by the process of polyzone refinement at PPM Pure Metals in Germany (July-September 2008), after which crystals will be grown at the Institut fuer Kristallzüchtung (IKZ) Berlin (until end of 2009, the period including test runs with natural, and depleted Ge). The actual detectors will be produced at Canberra, France (until about mid 2010). All these steps will occur under close collaboration with the GERDA collaborating Institutions.

Apart from the calibration system and material screening with a new facility run by our group at LNGS (so far operated mainly for XENON), we are building a GERDA detector test facility in our lab at the Physics Institute. The goal is to characterize segmented, natural Ge detectors which will serve to test the entire production process, before the actual enriched detectors will be fabricated.

3.2 Monte Carlo simulations

For the Monte Carlo simulations we are using the Geant4 based framework MaGe (4) which was designed for the GERDA (5) and Majorana (6) projects. The scope is to determine which sources will be used, in which configuration, position and strength, and how often. The sources will be employed to determine and monitor the stability of the energy scale and resolution of the detectors with time, as well as to establish and monitor the efficiency of the pulse shape analysis method which will be used to distinguish single-site interactions (as expected from a double beta decay event) from multiple scatters (for instance, multiple Compton scatters, or neutron interactions). Possible sources are for instance ^{60}Co, ^{228}Th and ^{133}Ba. We will design and construct the collimator and the structures which will be used to insert the sources into the LAr cryostat and bring them in suitable positions near the Ge crystals. The structure will be manufactured from ultra-pure materials (high-purity Cu or W, to be decided, and PTFE) and will fit within the current design of the super-insulated stainless steel cryostat.
For a first estimation of the needed source strengths 10^6 ^{60}Co events with random angular distribution were generated. Figure 3.2

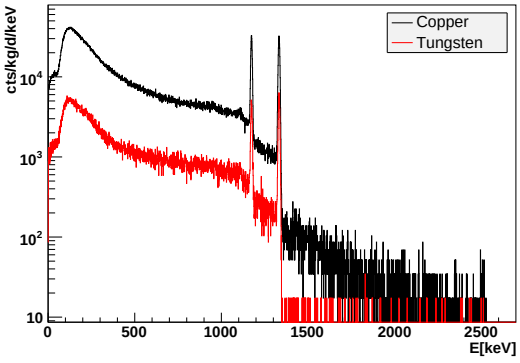

Figure 3.2: Monte Carlo simulation of ^{60}Co energy spectra for different collimator materials (Cu and W) in the non-segmented HPGe detectors of GERDA Phase I.

shows the sum of the full energy spectra in the HPGe detectors. First simulations of the influence of the calibration source in the parking position inside the cryostat show that independent of the collimator material the source (with reasonable activities) produces no significant background. For copper as collimator material, a minimum activity for a ^{60}Co source of around 20 kBq is required. The Monte Carlo study of other calibration sources is in progress.

3.3 GERDA test facility

GERDA Phase II will use new, 18-fold segmented, enriched ^{76}Ge detectors. Before operating these detectors at LNGS, it is essential to test the performance of non-isotopically-enriched prototype devices. We are building a detector test facility, in which we will first operate a commercial naked Ge-crystal immersed directly in liquid argon. The aim of this first step is to develop the infrastructure for the detector storage in vacuum, to test the cooling and warming-up procedures avoiding any condensation on the detector surfaces, to test low-noise electronics for detector operation and to validate the Monte Carlo simulations of calibration sources. A schematic view of the test facility is shown in Fig. 3.3.

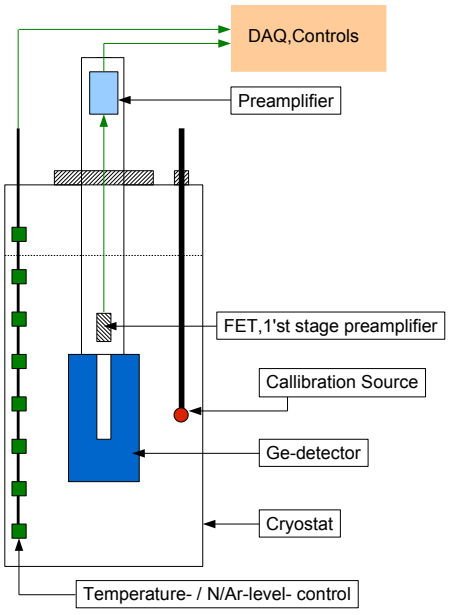

Figure 3.3: Schematic view of the test facility for the operation of naked Ge-detectors immersed in LAr. In the first phase, a bare, commercial HPGe crystals will be operated in a LAr cryostat.

3.4 GERDA sensitivity to solar axions

As an ultra low background experiment, GERDA may have the potential to detect other rare events, such from interactions caused by solar axions. Axions are proposed as an extension to the Standard Model of particle physics to explain the absence of charge-parity (CP) symmetry violation in the strong interaction (7). These neutral, very light (mass in the range 10^{-5}eV to 10 eV) particles interact very weakly with ordinary matter and relic axions from the early Universe could contribute to the dark matter in our galaxy. Axions could also be created near the strong electric field inside the hot plasma core of the Sun. Photons can be converted into axions, then stream freely to Earth where they can be in principle detected. While the primordial axion distribution on Earth is expected to be uniform, the solar axions flux exhibits a preferred direction depending on the relative orientation of an experimental set-up and the Sun, resulting in a modulation of the detection signal.

Figure 3.4 shows the differential flux of solar axions as expected on Earth (8). The mean axion energy is 4.2 keV and the interesting axion search window lies between $\sim$1-8 keV. Responsible for the axion-production in the Sun is the Primakoff effect, which allows a coupling between the axion and the electromagnetic fields with a coupling constant $g_{a\gamma\gamma}$. Following the calculations in (9) a first, conservative sensitivity of GERDA in the coupling constant versus axion mass parameter space was determined. It is shown in Fig. 3.5 along with

theoretical predictions and existing direct and indirect constraints. The preliminary limit of $g_{a\gamma\gamma} < 8 \cdot 10^{-10}\text{GeV}^{-1}$ was calculated for an assumed background of $1 \cdot 10^{-2}$ events/(keV kg year) in the low-energy region, for a total mass of 40 kg Ge and an exposure of 2 years. A more detailed study of the GERDA sensitivity to solar axions including the expected signal modulation, as well as of the background and energy threshold requirements of the detectors is in progress.

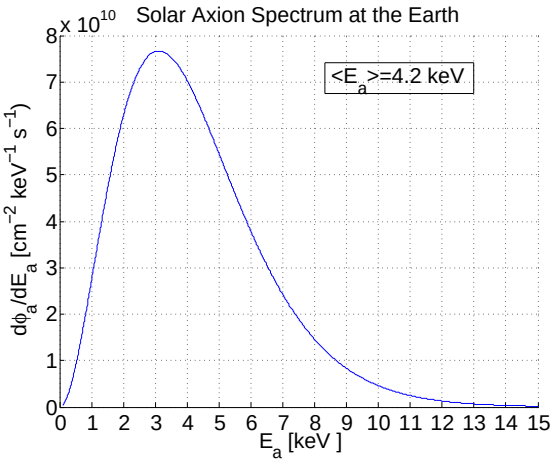

Figure 3.4: Solar axion flux produced by the Primakoff conversion in the Sun as expected on Earth.

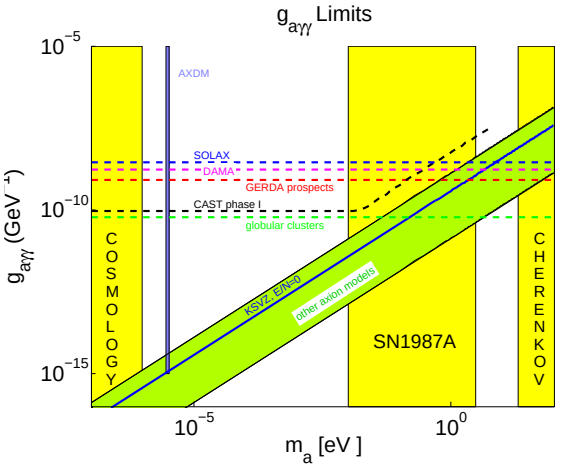

Figure 3.5: Limits on the coupling constant as predicted by different axion-models (green) in comparison with direct (SOLAX, DAMA, CAST) and indirect (cosmology, SN1987A, globular clusters) bounds and the potential GERDA limit ($g_{a\gamma\gamma} \sim 8 \cdot 10^{-10}\text{GeV}^{-1}$) with an assumed background of $1{\cdot}10^{-2}$ events/(keV kg year) in the low-energy region, 40 kg of mass and 2 years of exposure.

[1] S. R. Elliott and P. Vogel, Ann.Rev.Nucl.Part.Sci. **52** (2002) 115.

[2] L. Baudis et al. (Heidelberg-Moscow collaboration), Phys.Rev.Lett. **83** (1999) 41.

[3] I.G. Irastorza et al. (IGEX Collaboration), Phys.Rev. D **65** (2002) 092007.

[4] Y.-D. Chan et al., arXiv:0802.0860v1 [nucl-ex] (2008).

[5] I. Abt et al, GERDA: The GERmanium Detector Array for the search of neutrinoless $\beta\beta$ decays of ^{76}Ge at LNGS, Proposal to LNGS P38/04, September 2004.

[6] C.E. Aalseth et al. (Majorana Collaboration), Phys.Atom.Nucl. **67** (2004) 2002.

[7] R. D. Peccei and H. Quinn, Phys. Rev. Lett. 38 (1977) 1440 and Phys. Rev. D16 (1977) 1791.

[8] K. van Bibber, P. M. McIntyre, D. E. Morris and G. G. Raffelt, Phys. Rev. D **39** (1989) 2089.

[9] S. Cebrian *et al.*, Astropart. Phys. **10** (1999) 397 [arXiv:astro-ph/9811359].

4 Search for Cold Dark Matter Particles with XENON

A. Askin, L. Baudis, A. Ferella, M. Haffke, A. Kish, A. Manalaysay, R. Santorelli, E. Tziaferi

In collaboration with: Columbia, INFN, LLNL, Brown, CWRU, Coimbra, Rice, Yale

(XENON Collaboration)

Dark matter detectors based on liquid noble elements (Ar, Xe) are rapidly evolving and are providing sensitivities comparable to the ones of cryogenic mK-experiments. The best prospects for the unambiguous identification of a Weakly Interacting Massive Particle (WIMP) lie in detectors having negligible background competing with the dark matter signal. This can be achieved by using nuclear recoil discrimination in order to veto competing electron recoil events, by effective neutron shielding, and through the operation of a large homogeneous detector volume with 3-D position resolution. The latter information can be used to select single hit events characteristic of a WIMP interaction while rejecting multiple hit events associated with backgrounds that propagate from the edge of the detector into the fiducial volume. In order to achieve an increase in scattering rate sensitivity to $\sigma \sim 10^{-46}\mathrm{cm}^2$ (10^{-10}pb) a fiducial target mass on the order of 1 ton will be required which will yield $\sim$10 events per year. An increase in target mass alone is not sufficient, unless the competing backgrounds are eliminated. Efficient and redundant background rejection schemes are thus a key requirement for any WIMP experiment, along with the capability to observe nuclear recoil energy depositions as low as a few keV. Liquid argon (LAr) and xenon (LXe) have excellent properties as dark matter targets. They are intrinsic scintillators, with high scintillation (λ = 128 nm for Ar, λ = 178 nm for Xe) and ionization yields. They are available in large quantities and can be purified to 1 ppt (parts per trillion)-levels. Scintillation in LAr and LXe is produced by the formation of excimer states, which are bound states of ion-atom systems. If a high electric field ($\sim$1 kV/cm) is applied, ionization electrons can also be detected, either directly or through the secondary process of proportional scintillation. Measuring both the primary scintillation signal and a secondary process yields a method of discriminating between electron and nuclear recoils. Our group is involved in the 3-phased XENON project. The first phase, XENON10, has been successfully operated at the Gran Sasso Underground Laboratory (LNGS) and has provided the most stringent limits on spin-independent and spin-dependent, pure-neutron, WIMP-nucleon cross sections. XENON100 is currently being commissioned at LNGS, while the first studies for the next step, XENON1t, have been started.

4.1 The XENON10 and XENON100 experiments

The XENON10 detector was a 15 kg active mass, dual-phase (liquid and gas) xenon time projection chamber, operated in WIMP search mode at LNGS from August 2006 to February 2007. It used two arrays of UV-sensitive photomultipliers (PMTs) to detect the prompt and proportional light signals induced by particles interacting in the sensitive liquid xenon (LXe) volume. The bottom array of 41 PMTs was located below the cathode, fully immersed in LXe, and mainly detected the prompt light signal. The 48 PMTs of the top array were located in the cold gas above the liquid, detecting the proportional light signal

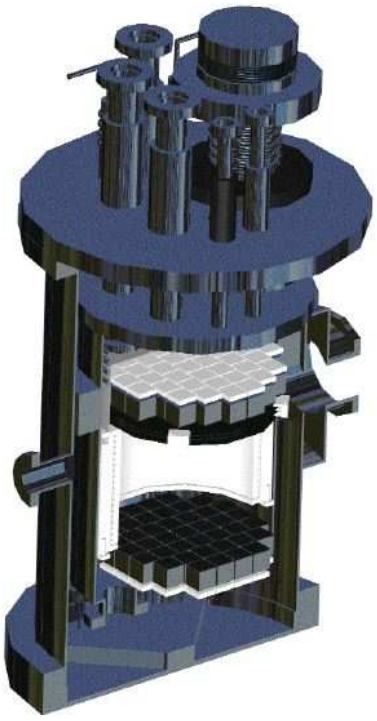

Figure 4.1: A schematic view XENON10 time projection chamber. Two UV-sensitive PMT arrays are used to detect the scintillation light produced by particles interacting in the 15 kg of active liquid xenon mass.

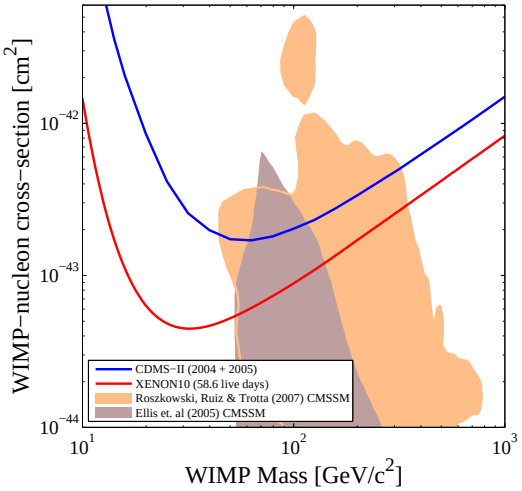

Figure 4.2: Limits on the Spin-Independent WIMP-nucleon cross section from XENON10 (red). Also shown are the CDMS-II 2005 result (blue) and theoretical predictions from supersymmetric models (filled regions).

which is created by the collision of extracted electrons with Xe atoms in the gas phase (the drift field was 1 kV/cm). Figure 4.1 shows a schematic view of the detector. The experiment had been calibrated with external gamma (^{57}Co, ^{137}Cs), an AmBe neutron source and with a small amount of neutron activated Xe gas, allowing a uniform energy and position calibration across the LXe active volume. The two Xe meta-stable states, ^{131m}Xe and ^{129m}Xe decay with 164 keV and 236 keV gamma rays with half-lives of 11.8 and 8.9 days, respectively. XENON10 had full 3D position sensitivity: the time separation between the two pulses of direct and proportional light (with a of maximum 75 μs) provided the event depth of an interaction with $<$1 mm resolution, the hit pattern in the top PMT array providing the x-y position with a resolution of a few mm.

The XENON10 results, using $\sim$136 kg-days exposure after cuts, demonstrated that LXe can be used for stable, homogeneous, large scale dark matter detectors, providing excellent position resolution and discrimination against the electron recoil background. The derived upper bound on the SI cross section on nucleons is 4.5 $\times 10^{-8}$pb for a WIMP mass 30 GeV/c^2. Figure 4.2 shows the SI limit as a function of WIMP mass, along with theoretical predictions for the neutralino. Since natural Xe contains ^{129}Xe (26.4%) and ^{131}Xe (21.2%) isotopes, each of these having an unpaired neutron, the XENON10 results substantially constrain the SD WIMP-nucleon cross section.

Our group was involved in several aspects for XENON10, such as measurements of the light yield with a small LXe prototype, material screening with a high-purity Ge detector in a new low-background facility at LNGS, Monte Carlo geometry of the detector and simulations of the gamma, alpha and neutron backgrounds, calibrations with n and γ sources, data processing and analysis as well as operations at LNGS. Some of these will be highlighted in the following sections.

Figure 4.3: The XENON100 TPC, fully assembled. The PTFE structures for the TPC and PMT holder were built at the UZH Physik Institut.

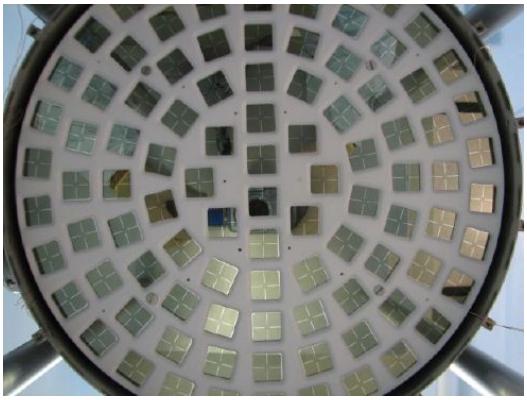

Figure 4.4: A picture of the XENON100 top PMT array with 98 square, UV-sensitive PMTs.

The 100 kg scale experiment, XENON100, is presently being commissioned at LNGS. Figure 4.3 shows a picture of the assembled inner structure. A picture of the top PMT array is shown in Fig. 4.4. XENON100 will operate a total of 170 kg (70 kg fiducial) of xenon, viewed by 242 PMTs, in a dual-phase TPC in an improved XENON10 shield. While the fiducial mass is increased by more than a factor of 10, the background will be lower by about a factor of 100 (through careful selection of ultra-low background materials, the placing of cryogenic devices and high-voltage feedthroughs outside of the shield and by using 100 kg of active LXe shield) compared to XENON10. The aim is to start the first science run in fall 2008, probing WIMP-nucleon SI cross sections down to $\sim 2 \times 10^{-9}$ pb.

The main activities of our group are testing and calibrations of XENON100 PMTs, material screening with the HPGe detector, Monte Carlo geometry, simulations of backgrounds and light collection efficiency simulations, energy calibrations with various sources, production of the inner TPC structures, as well as commissioning, operations, data processing and analysis.

4.2 Measurement of the liquid Xenon scintillation yield from low-energy nuclear recoils

When particles interact in LXe, they produce prompt scintillation photons and ionized electrons. The *yield*, defined as the number of quanta produced per unit energy, depends on the particle species interacting in the medium. The XENON10 experiment (1) has pushed the energy threshold of LXe detectors down to values where the yield for nuclear recoils is poorly understood. This lack of knowledge was the largest source of systematic uncertainties for the XENON10 results. In LXe dark matter experiments the energy scale of particle interactions is determined by the scintillation signal, thus the relevant quantity is not the full yield, but the scintillation yield of nuclear recoils. The low-energy electronic recoil energy scale is in general calibrated by using the photo-absorption line of 122 keV gammas from ^{57}Co.

The scintillation yield of nuclear recoils relative to the scintillation yield of 122 keV gammas is known as $\mathcal{L}_{eff}$. We have recently measured $\mathcal{L}_{eff}$ at the Radiological Research Accelerator Facility (RARAF) at Columbia University (in collaboration with the Columbia group). In previous measurements the behavior of $\mathcal{L}_{eff}$ at higher energies was flat at approximately 0.19, while more recent measurements suggested that below 20 keV $\mathcal{L}_{eff}$ departed from this (2; 3) value. Our new results from the measurement at the RARAF, shown in Fig. 4.5, tested $\mathcal{L}_{eff}$ down to 5 keV nuclear recoil energies and is not in agreement with previous results at these low energies. A publication of our results and their implication for the XENON10 dark matter limits is in progress.

Another quantity of interest for LXe dark matter detectors is the ionization yield of nuclear recoils at low energies. First measurements down to 20 keV exist (4); however the energy threshold of XENON10 was 4.5 keV and extrapolations from higher energies were necessary. To perform new, lower energy measurements using a mono-energetic neutron beam, a dedicated dual phase xenon time projection chamber is currently being constructed at the Physik Institut.

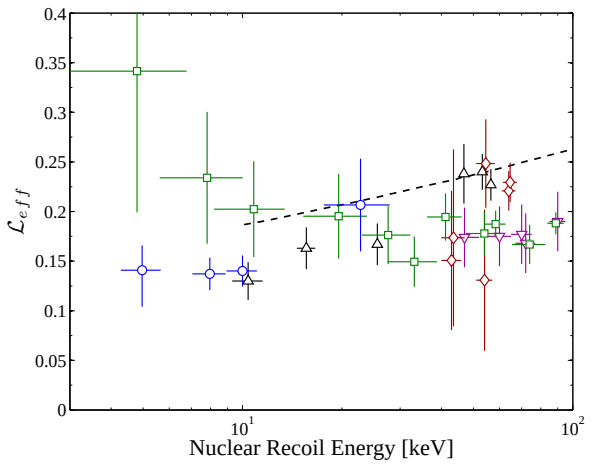

Figure 4.5: Recent measurements of $\mathcal{L}_{eff}$. Symbols correspond to (○)–this work; (□)–Chepel et al. [3]; (△)–Aprile et al. [2]; (◊)–Akimov et al. [6]; (▽)–Arneodo et al. [5]. Also shown is the theoretical prediction from Hitachi (dashed line) [7].

4.3 Material screening with a HPGe detector in a new low-background facility

To understand the residual radioactivity of materials and shields in terms of their U, Th, K and Co contaminations and model the expected backgrounds of the XENON experiments, we have installed an ultra-low background, high purity germanium detector (GATOR) at LNGS. A picture of the detector in its completed low-background shield is shown in Fig. 4.6.

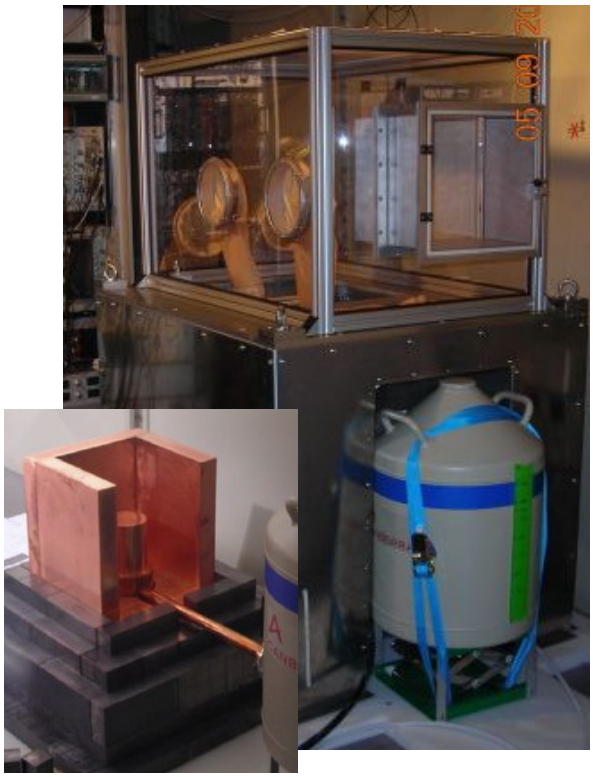

Figure 4.6: The HPGe detector in its completed shield structure at LNGS. The inset shows the detector in its open low-background Cu and Pb shield structure.

In Fig. 4.7 we show the comparison between the background of GATOR in its new facility, in its old shield at the Soudan Lab along

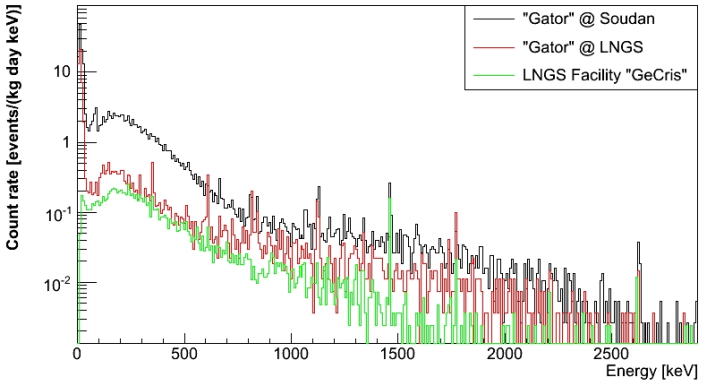

Figure 4.7:
Background spectra of Gator at Soudan (black), of Gator at Gran Sasso (red) and of a high purity germanium detector at Gran Sasso screening facility.

with the background of one of the world's most sensitive HPGe detectors, operated at LNGS. The background of GATOR is thus comparable to best existing HPGe detectors, and it will further improve with the decay of cosmogenic activities with typical half-lifes of 1 year.

To calculate GATOR's efficiency for each screening sample and to understand the detector's residual backgrounds we have implemented its detailed geometry into GEANT4. We have simulated ^{238}U, ^{232}Th, ^{60}Co, ^{40}K decays inside the copper cryostat and shield, ^{54}Mn, ^{65}Zn, ^{57}Co, ^{60}Co decays (cosmogenic nuclides) inside the Ge crystal and the Cu, as well as residual ^{222}Rn decays inside the N_2-purged sample chamber. An optimization of the background model is currently in progress.

We have screened several XENON10 and XENON100 materials (a subset of results are shown in Table 4.1) and have identified low-background materials, such as the stainless steel used for the cryostat and the high-voltage grids.

4.4 Gamma and neutron background studies for XENON100

The GATOR screening results are used to predict the gamma- and neutron-induced backgrounds in XENON100, which are mainly caused by the natural radioactive contamination of detector materials and shields. We have coded the detailed detector geometry in GEANT4 (a picture is shown in Fig. 4.8) and have simulated the main background contributions. The total predicted gamma background for XENON100 (shown in Fig. 4.9) in the WIMP search energy region (4.5 keV–30 keV) is at the level of 10×10^{-3} events/(kg day keV), before the yield based background discrimination. The breakdown of the different contributions is shown in table 4.2.

Table 4.1: **A subset of materials screened with the GATOR HPGe detector installed at LNGS.**

Material	Unit	^{238}U [mBq/unit]	^{232}Th [mBq/unit]	^{40}K [mBq/unit]	^{60}Co [mBq/unit]
PMT bases	base	0.71 ± 0.05	0.10 ± 0.03	NA	NA
22 PMTs	PMT	< 0.240	0.18 ± 0.05	11.5 ± 2.0	0.55 ± 0.1
12 PMTs	PMT	< 0.13	0.13 ± 0.05	13 ± 2	0.7 ± 0.1
Poly (I)	kg	2.426	< 0.674	< 4.658	< 0.536
Poly (II)	kg	< 3.80	< 2.69	< 5.88	< 0.684
S. Steel	kg	3.6 ± 0.8	1.8 ± 0.5	7 ± 1	< 4.92

We have also simulated the neutrons from spontaneous fission of ^{238}U and (α,n) reactions in the XENON100 detector and shield materials. Table 4.3 shows the resulting rates, with a total rate of $\sim 3 \times 10^{-6}$ events/(kg day keV) averaged over the 4.5 keV–30 keV energy region. Figure 4.10 shows the expected WIMP spectrum for a WIMP mass of 100 GeV/c^2 and a WIMP-nucleon cross-section of 2×10^{-45} cm^2, along with the predicted neutron background spectrum.

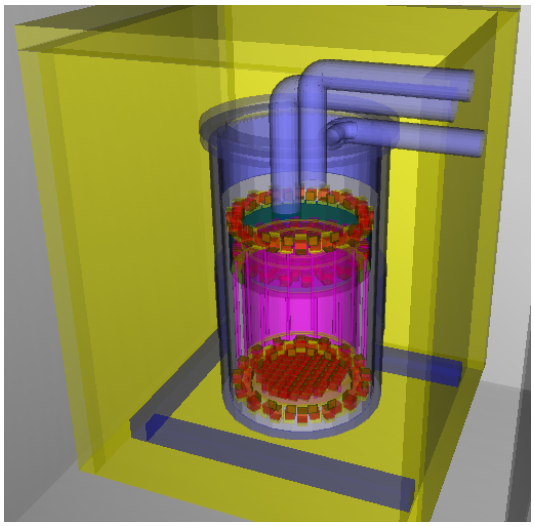

Figure 4.8: Geant4 geometry of the XENON100 detector and the inner shield.

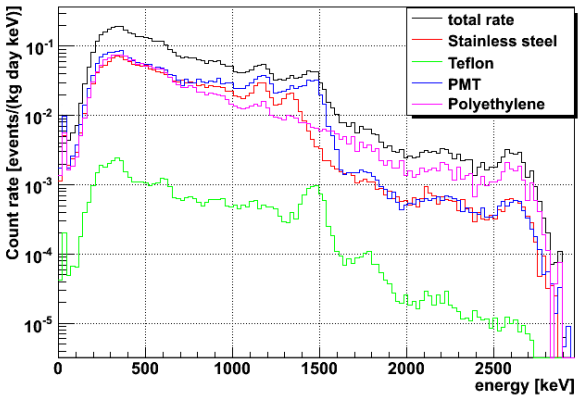

Figure 4.9: Predicted gamma background for XENON100, using measured residual radioactivity values for the detector and shield materials.

Table 4.2: Predicted gamma background rate in the WIMP search energy region (4.5 keV–30 keV) of XENON100.

Material	Rate of single scatters (10^{-3}events/(kg day keV))
Stainless Steel	2.01 ± 0.22
Teflon	0.68 ± 0.04
PMT	4.91 ± 0.60
Polyethylene	3.09 ± 0.29
Copper	0.026 ± 0.002
Total	10.72 ± 0.69

Table 4.3: Predicted neutron background rate in the WIMP search energy region (4.5 keV–30 keV) of XENON100.

Material	Rate of single nuclear recoils (10^{-7}events/(kg day keV))
Stainless Steel	2.93 ± 0.03
PMTs	3.18 ± 0.02
Teflon	6.26 ± 0.08
Copper	0.11 ± 0.02
Lead	0.38 ± 0.02
Polyethylene	4.87 ± 0.10
Liquid Xenon	1.07 ± 0.01
Total	28.8 ± 0.20

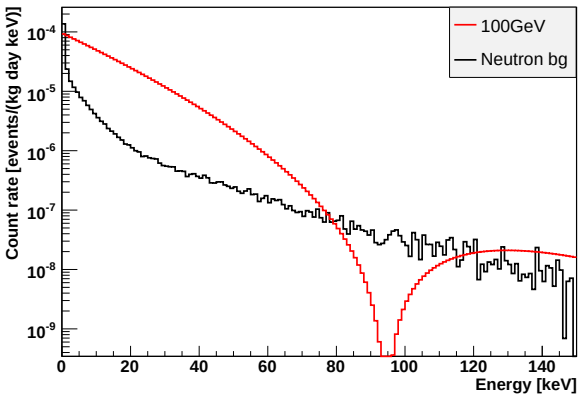

Figure 4.10: Predicted total neutron background (black) and expected WIMP spectrum (red) for a WIMP mass of 100 GeV/c^2 and a WIMP-nucleon cross-section of 2×10^{-45} cm^2.

An additional source of (high-energy) neutrons are interactions of fast cosmic muons with the rock and the Pb shield surrounding the detector. The angular distribution and energy spectrum of muons at the Gran Sasso Laboratory depth is known, and was used in propagating muons through a few meters of rock and into the XENON100 shields and detector. These simulations are currently in progress; the rate of single neutron interactions in the active volume is however expected to be lower than the one from the radioactivity of materials. Apart from background simulations, we are responsible for simulating the calibration sources ($^{57}_{27}$Co, $^{60}_{27}$Co, $^{137}_{55}$Cs, $^{228}_{90}$Th, Am-Be) and for light collection efficiency simulations and position reconstruction via neuronal network techniques.

4.5 Tests of XENON100 UV-sensitive photomultipliers

In order to determine the functionality of the PMTs used for XENON100 (Hamamatsu R8520), a PMT test facility was built at LNGS. The main aim of the test was to check each PMT before being placed inside the detector, rejecting poorly working devices, and selecting the best devices in terms of various parameters. The PMTs have been listed according to their measured gain, peak to valley ratio, resolution on single electrons and quantum efficiency (QE); the best PMTs have been selected to be placed in the most critical locations. In order to maximize the light detection of the tiny primary signal, the PMTs with highest QE have been placed on the bottom array. The PMTs showing the best single electron spectrum (in terms of the peak to valley ratio and resolution) have been placed in the outer ring of the top array where the position resolution, based on the analysis of the proportional light pattern, has to be precisely determined. More than 200 PMTs (in batches of 6) have been tested in a custom built black box containing a blue LED. The PMT signals have been integrated through a charge preamplifier and amplified through a shaping amplifier, before being acquired by a MCA. For each PMT several spectra were recorded according to different amounts of light stimulation (from 1 phe to some hundreds of phe's) and supplied voltage (from 650 V to 900 V).

In addition, the PMTs have been tested before and after having been kept for 48 h in dry ice in order to check their capability to work at cryogenic temperatures and to detect any noticeable change in their performance. From all the tested PMTs, 20 demonstrated a slightly worse performance and have been kept as spares, while 14 have been returned to the factory because of bad single electron response or failures after the cooling test.

[1] J. Angle et al. (XENON Collaboration), Phys. Rev. Lett. **100**, 021303 (2008).

[2] E. Aprile et al., Phys. Rev. D **72**, 072006 (2005).

[3] V. Chepel et al., Astropart. Phys. **26**, 58 (2006).

[4] E. Aprile et al., Phys. Rev. Lett. **97**, 081302 (2005).

[5] F. Arneodo et al., Nucl. Inst. and Meth. A **449**, 147 (2000).

[6] D. Akimov et al., Phys. Lett. B **524**, 245 (2002).

[7] A. Hitachi, Astropart. Phys. **24**, 247 (2005).

[8] J. Angle *et al.* [XENON10 Collaboration], Phys. Rev. Lett. **100** 021303 (2008).

[9] G.Carugno et al., Nucl. Inst. and Met. **A292** 580-584 (1990).

5 Precision measurements in pion decay

P. Robmann, A. van der Schaaf and U. Straumann

in collaboration with: University of Virginia, Charlottesville, USA; Institute for Nuclear Studies, Swierk, Poland; JINR, Dubna, Russia; Paul Scherrer Institut, Villigen, Switzerland and Rudjer Bošković Intitute, Zagreb, Croatia

(PEN Collaboration)

Within the Standard Model the decay $\pi \to e\nu$ is helicity suppressed ($\Gamma_{\pi\to e\nu}/\Gamma_{\pi\to\mu\nu} \approx m_e^2/m_\mu^2/(1-m_\mu^2/m_\pi^2)^2 \approx 1.2\times10^{-4}$) which makes it sensitive to a number of hypothetical exotic contributions. In the radiative decay $\pi \to e\nu\gamma$ the trivial inner-bremsstrahlung contribution is helicity suppressed as well and structure-dependent contributions dominate in large parts of the observable phase space. For the decay $\pi \to e\nu$ data taking just started. New results from our $\pi \to e\nu\gamma$ measurements have recently become available (1).

5.1 Testing lepton universality, the $\pi^+ \to e^+\nu$ decay

The experiment aims at improving the accuracy in the determination of the $\pi \to e\nu/\pi \to \mu\nu$ branching ratio by an order of magnitude (2). See past year's annual report for an introduction to the concept of lepton universality and a discussion of theoretical scenarios that might result in violations.

During a three-months measuring period in 2007 feasibility tests were performed at a pion stop rate of only 10^3/s. Our institute supplied a new set of beam counters and the associated 8 GHz transient recorders. We also refurbished the cylindrical scintillator hodosope situated in between the tracking detectors and the spherical CsI calorimeter. A preliminary analysis revealed no show-stoppers and the PSI program advisory committee gave green light to a first production run in 2008. By the time of writing data are taken at a 5×10^3/s stop rate which soon will be increased to 10^4/s giving 3×10^4 observed $\pi \to e\nu$ decays per day which should bring down the statistical error to O(10^{-3}) in 2008, significantly below the present uncertainty of the world average for the branching ratio (1.231(4) $\times$ 10^{-4}).

5.2 Pion substructure revealed in the $\pi^+ \to e^+\nu\gamma$ decay

In the standard description of radiative pion decay the decay amplitude has contributions from inner bremsstrahlung (IB), structure dependent radiation (SD$^\pm$), and interference terms. The structure dependent amplitude is parameterized by F_V and F_A, vector and axial vector form factors, respectively (see Ref. (3) for a comprehensive review). The conserved vector current (CVC) hypothesis relates F_V to the π^0 lifetime, yielding F_V=0.0259(9). Chiral symmetry (ChPT) calculations (4; 5; 6) give a value for F_A in the range 0.010–0.014.

Early experimental studies were limited by relatively low event statistics. The authors evaluated $\gamma \equiv F_A/F_V$ resulting in overall uncertainties ranging from 12 % to 56 % (7; 8; 9; 10; 11; 12). None of these measurements considered the dependence of the form factors on the invariant mass of the $e^+\nu$ pair.

During the years 1999 - 2001 a first data set with a 16 fold pre-scaled trigger was collected as a byproduct of the PIBETA $\pi^+ \to \pi^0 e^+\nu$ branching ratio measurement (13). The analy-

sis of the data resulted in a significant improvement in the accuracy of γ=0.443(15) (14) but also noted a substantial deficit of observed events in the high-E_γ/low-E_{e^+} kinematic region. For this reason a dedicated experiment was performed during 2004 after Zürich joined the new PEN collaboration. During these measurements the pion stop rate was reduced by almost an order of magnitude to $\sim 10^5$ /s. The reduced stop rate resulted in a dramatic reduction of accidental $e\gamma$ coincidences which allowed us to observe the decays in a much larger region of phase space.

In order to keep accidental background under control the trigger for data readout required at least one cluster of CsI crystals with a total energy above 52 MeV, the endpoint energy in muon decay. Candidate events exhibit one neutral shower in the calorimeter coincident in time with a positron track. Three kinematic regions were investigated:

region	E_{e^+} (MeV)	E_γ (MeV)	events
I	52 - 70	52 - 70	36k
II	10 - 52	52 - 70	16k
III	52 - 70	10 - 52	13k

with relative angle $\theta_{e\gamma}$ >40° for all regions. Under these conditions the decay is completely dominated by the SD$^+$ structure-dependent term proportional to $(F_V + F_A)^2$ (3).

The values of F_V, F_A, and a (defined by $F_V(q^2) = F_V(0)(1 + a \cdot q^2)$, $F_A(q^2) = F_A(0)$, and $q^2 = 1 - (2E_\gamma/m_\pi)$) were fit to the measured data by χ^2 minimization:

$$\begin{aligned} F_A &= +0.0117(17) \\ F_V &= +0.0258(17) \\ a &= +0.095(58) \end{aligned}$$

which represent a fourteen-fold improvement over previous measurements. The excellent agreement between the measured and calculated distributions for the best-fit parameter values (see

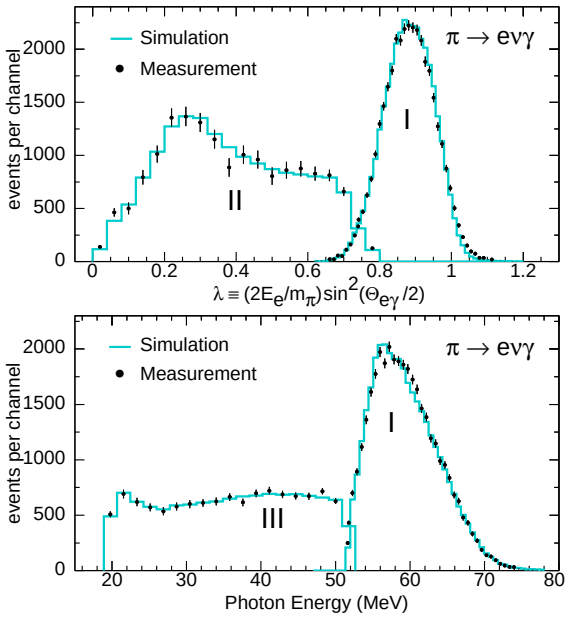

Figure 5.1: Background-subtracted $\pi^+ \to e^+\nu\gamma$ distribution of the kinematic variable $\lambda \equiv (2E_e/m_\pi)\sin^2(\theta_{e\gamma}/2)$ for regions I and II (top panel), and of the photon energy for regions I and III (bottom panel). For the simulation the best-fit values of F_V, F_A, and a were used.

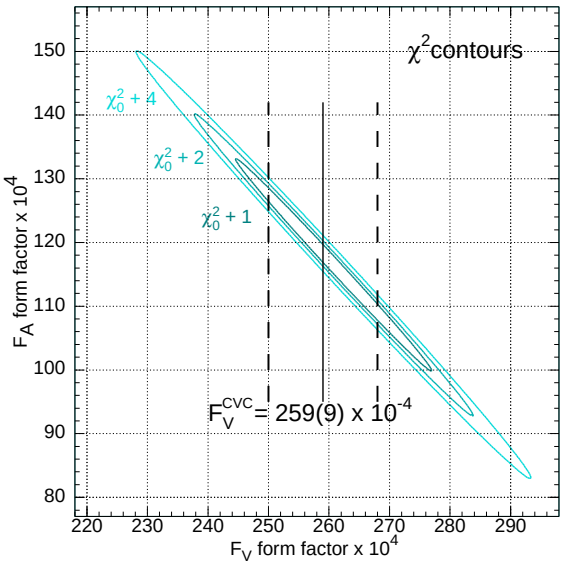

Figure 5.2: Contour plot of loci of constant χ^2 for the minimum value χ^2_0 plus 1, 2, and 4 units, respectively, in the $F_V \times F_A$ parameter plane, keeping the parameter a=0.041. The range of the CVC prediction, F_V = 0.0259(9) is indicated.

Fig. 5.1) reflects the perfect description of the data by CVC and standard $V-A$ theory in all regions of phase space. As discussed above the data are most sensitive to the combination $F_A + F_V$ which is illustrated in Fig. 5.2.

Conclusions

- The best-fit value of F_A agrees well with ChPT calculations, tending to the middle of the reported range (4; 5; 6).
- A more precise measurement of $\tau_{\pi 0}$ is needed to make full use of our data in determining F_A.
- The deficit of observed events in the high-E_γ/low-E_{e^+} has not been confirmed.
- The branching ratio for $\mathrm{E}_\gamma > 10$ MeV and $\theta_{e\gamma} > 40^o$ is measured to be $73.9(5)\times 10^{-8}$.
- The pion polarizability can be determined as follows: using the one-parameter fit we obtain $\alpha_E = -\beta_M = (2.78 \pm 0.02_{exp} \pm 0.10_{Fv}) \times 10^{-4}\,\mathrm{fm}^3$, where the first uncertainty comes from the fit and the second from the current CVC-derived value of F_V; alternatively, one obtains $2.7^{+0.6}_{-0.5} \times 10^{-4}\,\mathrm{fm}^3$ based on our unconstrained fit of F_A and F_V.
- In addition, we use the latter fit result and CVC to make an independent determination of the neutral pion lifetime: $\tau_{\pi 0} = (8.5 \pm 1.1) \times 10^{-17}\,\mathrm{s}$.

[1] M. Bychkov et al., **New Precise Measurement of the Pion Weak Form Factors in the $\pi^+ \to e^+\nu\gamma$ Decay**, submitted to Phys. Rev. Lett., arXiv:0804.1815 [hep-ex].

[2] PEN Collaboration, PSI experiment R-05-01, D. Pocanic and A. van der Schaaf, spokespersons.

[3] D. A. Bryman et al., Phys. Rep. 88, 151 (1982).

[4] B. R Holstein, Phys. Rev. D 33, 3316 (1986).

[5] J Bijnens and P. Talavera, Nucl. Phys. B 489, 387 (1997).

[6] C. Q Geng et al., Nucl. Phys. B 648, 281 (2004).

[7] P. Depommier et al., Phys. Lett. 7, 285 (1963).

[8] A. Stetz et al., Nucl. Phys. B 138, 285 (1978).

[9] A. Bay et al., Phys. Lett. B 174, 445 (1986).

[10] L. E Piilonen et al., Phys. Rev. Lett. 57, 1402 (1986).

[11] C. A Dominguez and J. Solc, Phys. Lett. B 208, 131 (1988).

[12] V. N Bolotov et al., Phys. Lett. B 243, 308 (1990).

[13] D. Počanić et al. (PIBETA Collaboration), Phys. Rev. Lett. 93, 181803 (2004).

[14] E. Frlež et al. (PIBETA Collaboration), Phys. Rev. Lett. 93, 181804 (2004).

6 Search for $K\pi$-atoms

Y. Allkofer, C. Amsler, A. Benelli[3], S. Horikawa, C. Regenfus, and J. Rochet

In collaboration with: Basel, Bern, Bucharest, CERN, Dubna, Frascati, KEK, Kyoto, Messina, Moscow, Prague, Protvino, Santiago and Tokyo.

(DIRAC-II Collaboration)

The $K\pi$-scattering length is of interest to test chiral perturbation predictions involving the s-quark. The low energy $K\pi$-phase shifts (S-wave isospin 1/2 and 3/2 phases) are poorly known below 1 GeV/c and hence their extrapolations to zero energy are very uncertain. We are therefore searching for the electromagnetically bound $K^+\pi^-$ (and $K^-\pi^+$) system to measure its mean life τ which is related to the S-wave $K\pi$-scattering length. We intend to measure τ (predicted to be about 3.7 fs) with a precision of 10%.

Details on the DIRAC apparatus can be found in Ref. (1). We have developed and built the aerogel Čerenkov counters and the heavy gas system required to identify kaons from the dissociation of $K\pi$-atoms, and are responsible for the analysis of the corresponding data. More on these detectors can be found in previous annual reports and in a recent publication (2).

The aerogel detector is located in the left (positive charge) arm of the DIRAC spectrometer and consists of three independent modules. Two of them have aerogel with the refractive index $n = 1.015$ (24ℓ) for kaon-proton separation between 4 and 5.5 GeV/c , and the third one (13ℓ) has the lower index $n = 1.008$ for 5.5 to 8 GeV/c kaons. The loss due to light absorption is compensated by using a wavelength shifter and also by increasing the radiator thickness at the center of the detector (pyramid geometry). A cosmic ray test showed that, thanks to the pyramid design, the light yield did not depend significantly on the impact position. For the 1.015 detector we obtained about 6.4 photoelectrons for cosmic muons, implying $\sim$ 5 photoelectrons for 4 GeV/c kaons. The performance of the 1.008 counter could not be tested with cosmic rays.

Figure 6.1 shows the aerogel counters installed in the DIRAC experiment in the West hall at CERN. The operation of the DIRAC-II experiment, originally planned for summer 2006, was postponed by one year due to repeated failures of a switching magnet in the CERN primary proton beam line. The defective magnet was successfully replaced by CERN in spring 2007 and DIRAC-II could finally be commissioned in June 2007. The aerogel counters worked in the beam according to expectations, although we had first to strengthen

Figure 6.1: Photograph of the three aerogel modules (black) in the experimental area. The scintillation hodoscopes and the N_2-Čerenkov counter (blue) are also visible.

[3]Visitor from the University of Basel

the magnetic shielding of the (vertical) photomultipliers with additional μ-metal to protect them from the fringe field of the DIRAC dipole magnet, which is also vertical.

The trigger rejects electrons with the N_2-Čerenkov detector in anticoincidence and selects symmetric tracks in the two spectrometer arms. Mainly pions and protons are present, as well as a few kaons. The pions are shown by the green ellipse and protons by the red ellipse in Fig. 6.2. The horizontal accumulation of events at low amplitudes (blue ellipse) is due to the ADC pedestals for triggers with protons below Čerenkov threshold, including electronic noise. Kaons are not visible at this point due to their low intensity.

Data were also taken with inverted polarities to study the proton contamination, i.e. by triggering on negative tracks in the aerogel arm, in which case the contribution from antiprotons is negligible. The normalized ADC spectra were then subtracted, leaving essentially protons in the positive charge spectrum which was then subtracted from the distribution shown in Fig. 6.2, leading to a pure K^+-spectrum. Figure 6.3 shows the distribution of the light amplitude which agrees with cosmic ray measurements. The peak at low amplitudes is due to the one-photon contribution. Cutting at one photoelectron one obtains a proton rejection efficiency of about 93.2%, while the kaon detection efficiency is 94.2%. The proton contribution can also be studied with $\Lambda \to \pi^- p$ decays (see Fig. 6.4).

We have also built the C_4F_{10} heavy gas system for the Čerenkov counters in both arms to veto pions. The counters were delivered by our collaborators from Dubna. The system has been running since June 2007 without interruption. However, the rate of C_4F_{10} loss was found to be larger than initially estimated and be modified. The design of the improved scheme has been done (Fig. 6.5) and the construction will be completed for the 2008 runs.

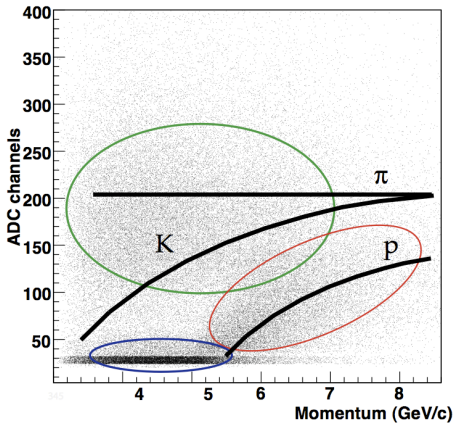

Figure 6.2: Signal amplitude (in ADC counts) as a function of momentum for one of the n=1.015 aerogel modules. The curves show the expected light yields. The ellipses show the pions (green), the protons (red) and the electronics noise (blue).

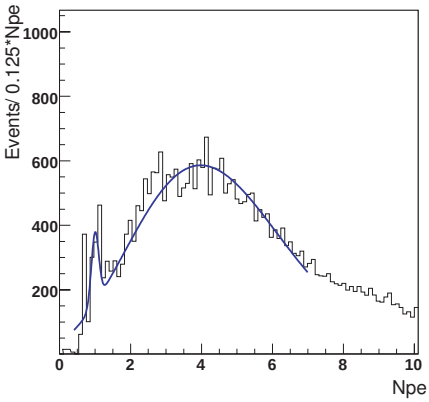

Figure 6.3: Distribution of the light output (in photoelectrons, N_{pe}) for positive kaons traversing the heavy aerogel counter (see text). The curve is a fit.

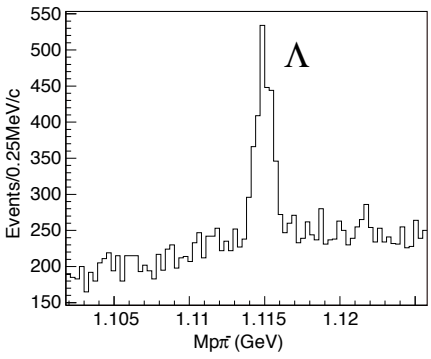

Figure 6.4:
Λ-signal in the $\pi^- p$-invariant mass distribution.

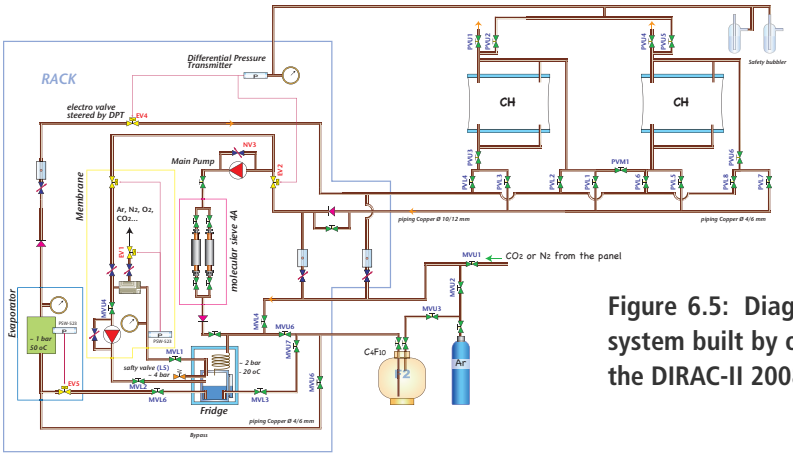

Figure 6.5: Diagram of the radiator-gas recirculation system built by our group (improved in robustness for the DIRAC-II 2008 runs).

Figure 6.6 shows an amplitude spectrum for electrons from the C_4F_{10}-detector, obtained by triggering on the N_2-Čerenkov counter. Dividing the mean amplitude by that of the single-photoelectron peak, we obtain the mean number of photoelectrons $N_{\rm pe} = 28.0 \pm 0.2$.

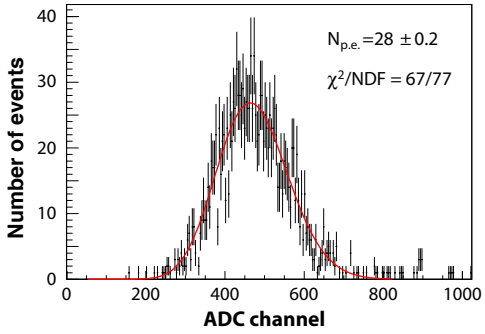

Figure 6.6: Amplitude spectrum of electrons in the heavy gas counter.

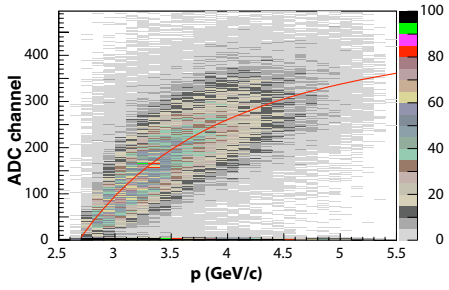

Figure 6.7: Pulse height distribution for pions as a function of momentum.

Figure 6.7 shows the signal amplitude for pions as a function of momentum. The curve is a fit in which the refractive index of the radiator and the number of photoelectrons were set as free parameters, assuming a velocity $\beta = 1$. The fit leads to a refractive index $n = 1.00137$ which corresponds to a wavelength of 300 nm for Čerenkov photons and is consistent with the Čerenkov spectrum convoluted with the spectral response of the UV-glass photomultiplier. The pion detection efficiency is found to be larger than 99.5% at 4 GeV/c.

The yield of $K\pi$- atoms is expected to be about 25 $\times$ lower than for $\pi^+\pi^-$-atoms (3). Assuming equal acceptances and the increase in beam flux between the former DIRAC I experiment (which studied $\pi^+\pi^-$-atoms) and DIRAC II by a factor of two, this should lead to about 1'400 reconstructed $K^+\pi^-$- (and $K^-\pi^+$-) atoms in the 2007 sample. DIRAC II will take data at least until the end of 2009.

[1] B. Adeva *et al.*, Nucl. Instr. and Meth. in Phys. Research **A 515** (2003) 467.

[2] Y. Allkofer *et al.*, Nucl. Instr. Meth. in Phys. Research **A 582** (2007) 497.

[3] B. Adeva *et al.* (DIRAC Collaboration), Phys. Lett. **B 619** (2005) 50.

7 Particle Physics at DESY/HERA (H1)

Katharina Müller, K. Nowak, P. Robmann, C. Schmitz, A. Schöning, U. Straumann, and P. Truöl

in collaboration with: N. Berger, M. Del Degan, C. Grab, G. Leibenguth, M. Sauter and T. Zimmermann, Institut für Teilchenphysik der ETH, Zürich; S. Egli, R. Eichler, M. Hildebrandt, and R. Horisberger, Paul Scherrer Institut, Villigen, and 37 institutes outside Switzerland

(H1 - Collaboration)

7.1 Summary

Two data taking periods with the proton energy reduced from its nominal value of 920 GeV between March 21, 2007 and June 30, 2007 ended the experimental phase of the H1-collaboration at the HERA electron-proton storage ring. Since then the detector has been dismantled and the collaboration concentrates on the analysis of the different data sets from the post-upgrade HERA-II phase (2004-2007, $\mathcal{L}$ =238 pb^{-1} e^-, $\mathcal{L}$ =219 pb^{-1} e^+) and the pre-upgrade HERA-I phase (1993-2000, $\mathcal{L}$ =118 pb^{-1} $e^\pm$). Figure 7.1 shows how the integrated luminosity was accumulated over the years. During the low energy run 6.2 pb^{-1} and 12.4 pb^{-1} were collected with 27.4 GeV positrons colliding with 575 or 460 GeV protons, respectively.

Eleven publications ((1)-(11)) and a fair number of contributions to the summer 2007 high-energy physics conference EPS2007 in Manchester ((12),(13)-(31)) attest to the continuing effort of the collaboration exploring proton structure and testing quantum chromodynamics (QCD) predictions. This program entails the precise determination of the neutral and charged electroweak current cross sections at high momentum transfer leading to parton density functions (PDF) in pre-HERA inaccessible domains of Bjorken x and momentum transfer Q^2, precise measurements of the running coupling constant α_s, diffractively produced final states, hidden and open charm and beauty production as well as searches for states outside the Standard Model.

Our analysis effort concentrated on events with isolated photons produced in either photoproduction ($Q^2 \approx 0$), as discussed below (Sec. 7.3), or deep inelastic scattering ($Q^2 > 4$ GeV^2) as described in the thesis of Carsten Schmitz (32), the publication which resulted from it (9) or in previous annual reports (33) in some detail. The technical paper dealing with our hardware contribution to the upgraded H1-detector, the five-layer inner multiwire proportional chamber (CIP2000) and the z-vertex trigger derived from it, has appeared too (34).

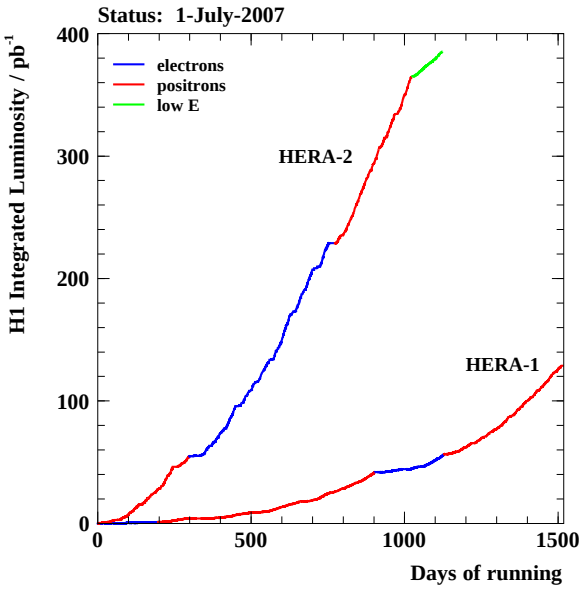

Figure 7.1:
Integrated luminosity as a function of running time 1993-2000 (HERA-I), and 2004-2007 (HERA-II).

New results, partly preliminary (35), which deserve to be mentioned, concern the following topics:

- direct measurement of the longitudinal structure function F_L at medium Q^2; combined PDF-fit of ZEUS and H1 data (HERA I);
- multi-jets at high and low Q^2 leading to an improved determination of α_s;
- photo-produced diffractive dijets, diffractive ρ- and ϕ-mesons, inelastic J/ψ- and D^*-mesons, and prompt photons;
- searches for leptoquarks, lepton flavor violation, excited neutrinos, and exotic baryons (charmed pentaquark);
- strangeness and D^*-meson production in deep inelastic scattering, and charm fragmentation.

7.2 Structure functions

The primary goal of the low energy runs was the determination of the longitudinal structure function F_L appearing in the inclusive deep inelastic cross section as (see also last years annual report (33)):

$$\frac{d^2\sigma}{dxdQ^2} = \frac{2\pi\alpha^2 Y_+}{Q^4 x}\left[F_2(x,Q^2) - f(y)\cdot F_L(x,Q^2)\right] ,$$

with $y \equiv Q^2/sx$, $Y_+ \equiv 1+(1-y)^2$ and $f(y) \equiv y^2/Y_+$. It is possible to extract F_L directly from two or more cross section measurements at fixed Bjorken x and negative momentum transfer squared Q^2 by varying the fractional electron energy loss y, which is possible by changing the centre-of-mass energy $\sqrt{s} = \sqrt{4E_eE_p}$ via the proton beam energy. F_L is then determined from a Rosenbluth plot of $F_2(x,Q^2)$ versus y^2/Y_+ using the different values of s available. This procedure has been successfully applied already,

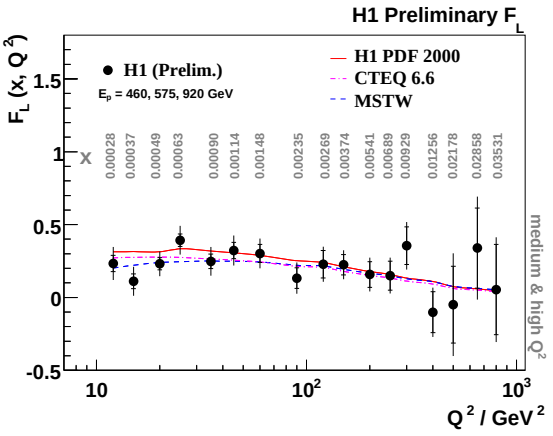

Figure 7.2: Longitudinal structure function as function of Q^2. The value of x for each data point is indicated [35].

as shown in Fig. 7.2, to the medium Q^2 2007 data. The new data confirm the behavior predicted by the PDF-analysis of HERA-I data. The latter have now been incorporated in a combined analysis of the data from both HERA-collaborations, results of which are shown in Figs. 7.3 and 7.4. A consistent treatment of the systematic uncertainties of both data sets,

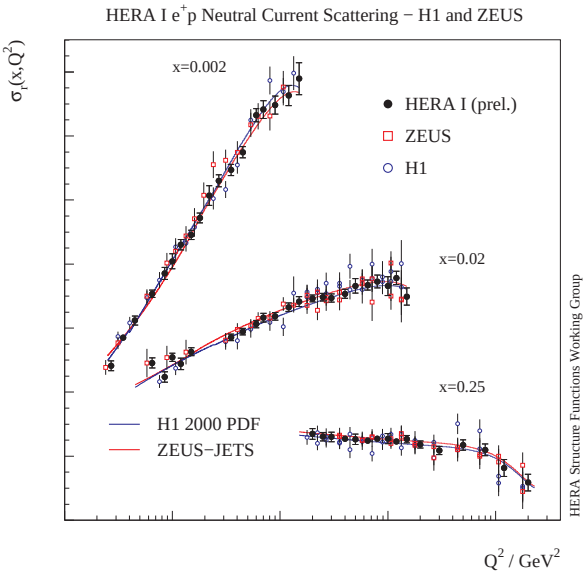

Figure 7.3: Examples of HERA-I data sets from the ZEUS- and the H1-collaborations entering the common PDF-fit.

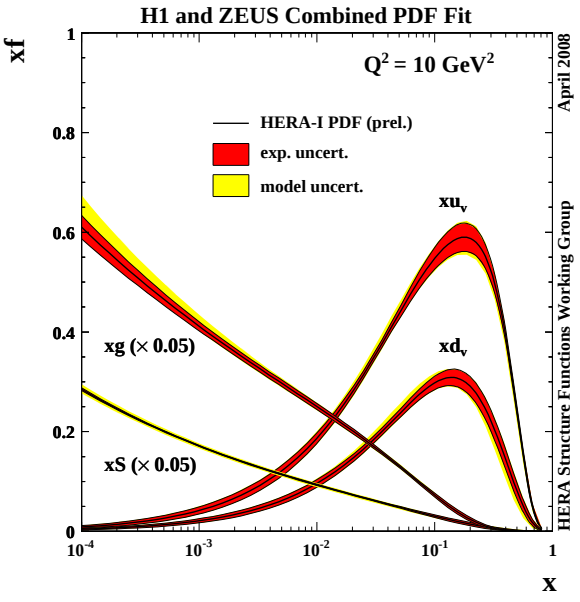

Figure 7.4:
A typical result at Q^2=10 GeV^2 indicates a better constrained gluon distribution at high and low x.

choice of parametrisation at the momentum transfer Q_0^2, where the DGLAP-evolution of the PDF's is started, incorporation of correlations and a suitable exploits the full potential for precision of the HERA-data. At present the consequences are most visible for the gluon density at low x. Clearly it is planned to continue with this work, once the even higher statistics HERA-II data have been analyzed completely, particularly in view of the need for accurate PDF's for theoretical predictions at the Large Hadron Collider (LHC).

7.3 Isolated photons in photoproduction and deep inelastic scattering

In the past years our analysis group, lead by Dr. Katharina Müller, focused on the analysis of events with isolated photons. The analyses profit a lot from a close collaboration with the local theory group of Thomas Gehrmann.

Isolated photons with high transverse momentum in the final state are a direct probe of the dynamics of the hard scattering process, since they are directly observable without large corrections due to hadronisation and fragmentation. A good understanding of the standard model production mechanism of isolated photons is important for the understanding of the background to a light Higgs decaying into two photons at LHC as well as for searches for physics beyond the standard model.

Common to all analyses is the identification of the photon as an isolated electromagnetic cluster with no track pointing to it in order to reject charged particles. To ensure isolation of the photon, the fraction z of the transverse energy of the photon-jet (jet containing the photon) carried by the photon candidate has to be larger than 90%. The experimental difficulty is the separation of the photons from the decay products of neutral mesons, mainly π^0 or η, since at high energies the decay photons are not resolved but reconstructed in one single electromagnetic cluster. The photon signal is extracted by a shower shape analysis which uses six discriminating shower shape functions in a likelihood analysis.

In the thesis of Carsten Schmitz on isolated photons in deep inelastic scattering (9; 32) it has been shown that the leading order (LO) calculation (36) significantly underestimates the cross section of the production of isolated photons by roughly a factor two, in particular at low Q^2. A next to leading order calculation (37) which is only available for the exclusive process with a photon and a hadronic jet in the final state is higher than the LO prediction and describes the data well in shape but is also too low in absolute normalisation.

In the past months the analysis has been extended to the analysis of less isolated photons which gives access to the quark-to-photon fragmentation function (38). The latter cannot be calculated in perturbative QCD but

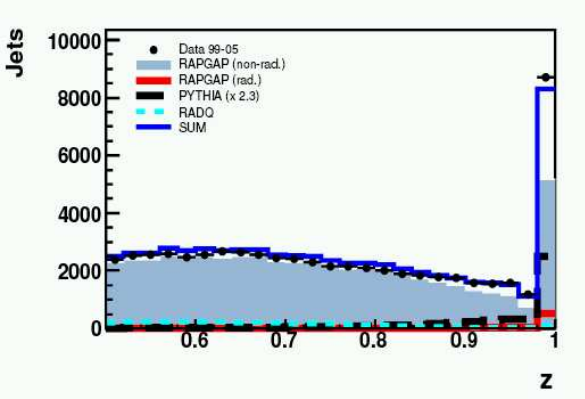

Figure 7.5: Distribution of the isolation parameter $z \equiv E_T^{\gamma}/E_T^{photonjet}$. The shaded area corresponds to the background contribution.

has to be determined by the experiments, which was only done by the ALEPH collaboration (39). The cross section is measured in bins of z, where z is the isolation parameter defined above.

Figure 7.5 shows the measured z distribution. The shaded area corresponds to the background and the white area can be attributed to the photon contribution. Whereas in the isolated case ($z > 0.9$) a clear signal of the photon is visible the background is dominating by far for photons close to a hadronic environment ($z < 0.9$). The extraction of less isolated photons therefore mainly requires a detailed understanding of the shower shapes of the background. Preliminary results are expected to be ready this summer.

In photoproduction (PhD thesis of Krzysztof Nowak) at very low Q^2 the scattered electron escapes detection through the beam pipe. The exchanged quasi-real photon either interacts directly with a parton from the proton (direct contribution) or resolves into partons which take part in the interaction (resolved contribution). Hence, the cross section yields information on the quark and gluon densities in the photon and the proton with different and generally lower corrections for hadronisation than in jet measurements. The analysis extends the phase space of the previous

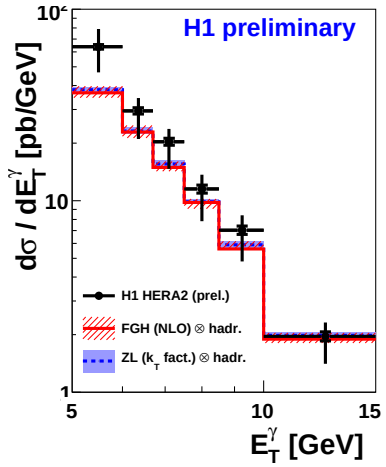

Figure 7.6: Inclusive prompt photon single differential cross sections as function of E_T^{γ}. The measured cross section is compared to two calculations.

H1 measurement in photoproduction (40) towards larger pseudorapidities of the photon and lower event inelasticities. The data used for the measurement were collected during the years 2004-2007 corresponding to a total integrated luminosity of 340 pb^{-1}, increased by a factor of three over the previous measurement. Following the results of the Bachelor thesis of Arno Gadola who analysed the separation of photons and π^0 at high transverse energies, the analysis is further extended to transverse energies up to 15 GeV. Preliminary results will be shown this spring. Figure 7.6 shows the single differential inclusive cross section as a function of transverse energy of the photon. The data are compared to a NLO calculation (41), denoted by FGH), and a calculation based on the k_T factorisation approach which uses the unintegrated quark and gluon densities of the proton and the photon according to the Kimber-Martin-Ryskin prescription (42) (ZL). Both calculations are slightly lower than the data most significantly at low E_T^{γ}. The momentum fraction of the partons in the photon (x_{γ}) and in the proton (x_p) can be determined in the exclusive sample with an isolated photon and an additional hadronic jet

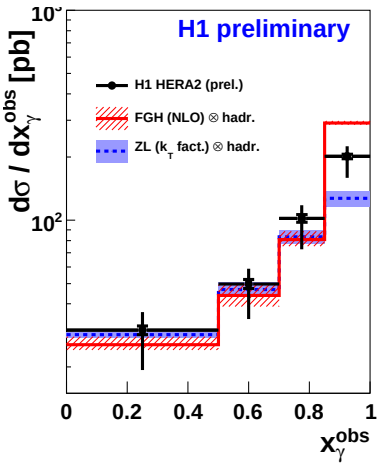

Figure 7.7: Exclusive (photon plus jet) cross sections as a function of x_γ. The measured cross section is compared to two calculations.

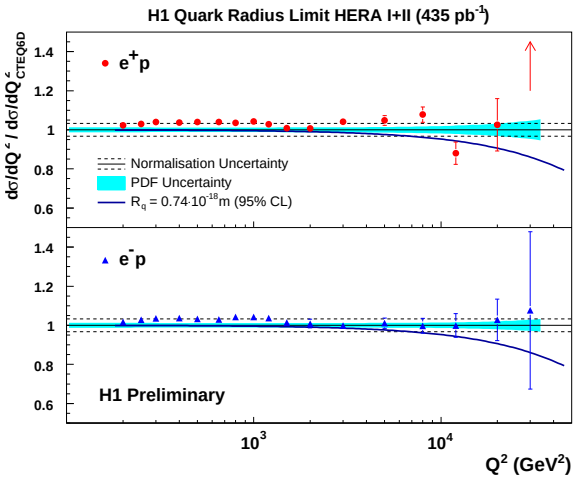

Figure 7.8: The good agreement with the behavior expected for the neutral current e^+p cross section at high Q^2 sets an upper limit on the quark radius of 0.74 attometer [35].

from the kinematics of the photon and the jet. The cross section as a function of x_γ is shown in Fig. 7.7. The distributions are described reasonably well by the two calculations.

7.4 Other results from recent analyses

The ultimate spatial resolution of the HERA *electron microscope* is demonstrated by the high Q^2 neutral current cross section shown in Fig. 7.8, which exhibits the deviations expected if quarks were extended objects.

That a measurement of the relative jet rates at different Q^2, for which some experimental errors cancel, is sensitive to the strong coupling α_s has been shown by H1 previously. These analyses have now been extended to lower Q^2 than before and at higher Q^2 to include both HERA-I and HERA-II data. Figs. 7.9 and 7.10 show the results for the running coupling.

The analysis yields for low Q^2:

$$\alpha_s(M_Z) = 0.1186 \pm 0.0014^{+0.0132}_{-0.0101} \pm 0.0021$$

and for high Q^2:

$$\alpha_s(M_Z) = 0.1182 \pm 0.0008^{+0.0041}_{-0.0031} \pm 0.0018 \ ,$$

where the first error given is experimental, the second comes from the model (scale) dependence and the last is introduced by the uncertainty of PDF's. Comparison with results from ZEUS and the world average largely given by e^+e^- collider data shows good agreement.

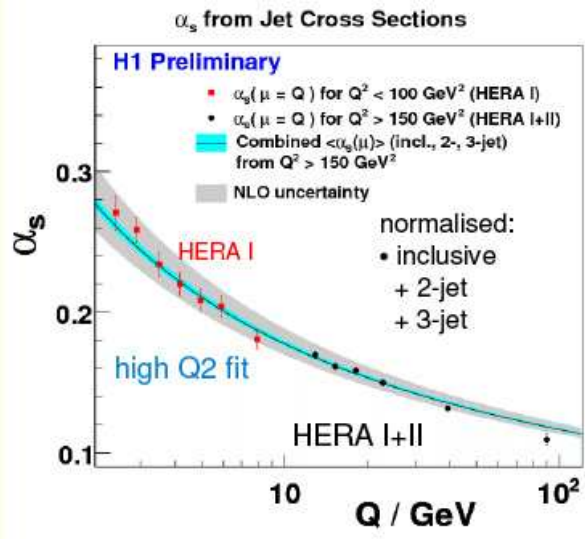

Figure 7.9: Fitted values of $\alpha_s(Q)$ from inclusive jet rates.

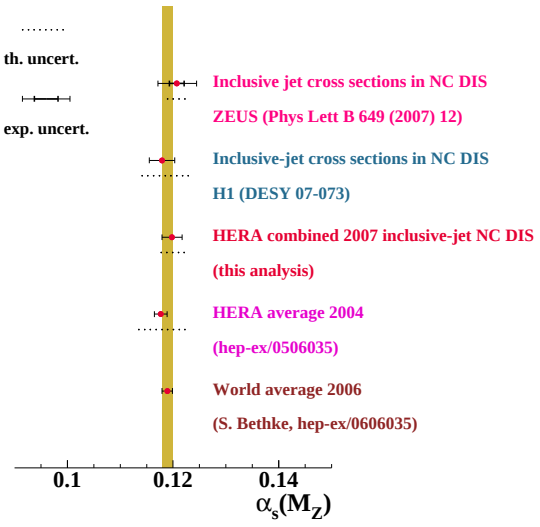

Figure 7.10: Comparison of the HERA results for $\alpha_s(M_Z)$ with the world average.

[1] **Inclusive D^* Meson and Associated Dijet Production in Deep Inelastic Scattering at HERA**,
A. Aktas et al. [H1-Coll.], DESY 06 – 240, hep-ex/0701023, Eur.Phys.J. **C51** (2007), 271.

[2] **Search for Lepton Flavour Violation in ep Collisions**
A. Aktas et al. [H1-Coll.], DESY 07 – 007, hep-ex/0703004, Eur.Phys.J. **C52** (2007), 833.

[3] **Tests of Factorisation in the Diffractive Production of Dijets in Deep Inelastic Scattering and Photoproduction at HERA**,
A. Aktas et al. [H1-Coll.], DESY 07 – 018, hep-ex/0703022, Eur.Phys.J. **C51** (2007), 549.

[4] **Search for Baryonic Resonances Decaying to $\Xi\pi$ in Deep Inelastic Scattering at HERA**,
A. Aktas et al. [H1-Coll.], DESY 07 – 045, arXiv:0704.3594 [hep-ex], Eur.Phys.J. **C52** (2007), 507.

[5] **Charged Particle Production in High Q^2 Deep Inelastic Scattering at HERA**,
F.D. Aaron et al. [H1-Coll.], DESY 07 – 065, arXiv:0706.2456 [hep-ex], Phys.Lett. **B654** (2007), 148.

[6] **Measurement of Inclusive Jet Production in Deep-Inelastic Scattering at High Q^2 and Determination of the Strong Coupling**,
A. Aktas et al. [H1-Coll.], DESY 07 – 073, arXiv:0706:3722 [hep-ex], Phys.Lett. **B653** (2007), 134.

[7] **Dijet Cross Sections and Parton Densities in Diffractive DIS at HERA**,
A. Aktas et al. [H1-Coll.], DESY 07 – 115, arXiv:0708.3217 [hep-ex], JHEP **10** (2007), 042

[8] **Measurement of Deeply Virtual Compton Scattering and its t-Dependence at HERA**,
F.D. Aaron et al. [H1-Coll.], DESY 07 – 142, arXiv:0709.4114 [hep-ex], Phys.Lett. **B659** (2008), 796.

[9] **Measurement of Isolated Photon Production in Deep-Inelastic Scattering at HERA**,
F.D. Aaron et al. [H1-Coll.], DESY 07 – 147, arXiv:0711.4578 [hep-ex], Eur.Phys.J. **C54** (2008), 371.

[10] **Three- and Fourjet Production in Deep Inelastic ep Scattering and Low x Parton Dynamics at HERA**,
F.D. Aaron et al. [H1-Coll.], DESY 07 – 200, arXiv:0711.2606 [hep-ex], Eur.Phys.J. **C54** (2008), 389.

[11] **Search for Excited Neutrinos at HERA**,
F.D. Aaron et al. [H1-Coll.], DESY 08 – 009, arXiv:0802.1858 [hep-ex], Phys.Lett. **B** (2008), in print.

[12] Contributed papers by the H1-Coll. to EPS2007 (HEP2007), Int. Europhysics Conf. on High Energy Physics, Manchester, UK, 19-25 July 2007; only those papers are listed, which have not yet been submitted to journals or to previous conferences.

[13] **D^* Production in Deep Inelastic Scattering with the H1 Detector** [12]

[14] **Inelastic Electroproduction of J/Ψ Mesons at HERA** [12]

[15] **Beam Charge Azimuthal Asymmetry in Deeply Virtual Compton Scattering at HERA II** [12]

[16] **Inclusive ep Scattering Cross Section at High Q^2 and High y** [12]

[17] **Measurement of the Inclusive ep Scattering Cross Section at Low Q^2 and x at HERA** [12]

[18] **Inclusive ep Scattering Cross Section at Low Q^2**

and High y [12]

[19] **Inclusive Jet Production in Deep Inelastic Scattering at Low and Medium** Q^2 **at HERA** [12]

[20] **Minijet Production in Deep Inelastic Scattering at HERA** [12]

[21] **Inclusive Jet Production at High** Q^2 **(HERA II)** [12]

[22] **Precision Measurements of** α_s **at HERA using Jets at High** Q^2 **(H1+ZEUS)** [12]

[23] **A Combined H1 and ZEUS Measurement of Events with Isolated Leptons and Missing** P_t **at HERA** [12]

[24] **Multi-Lepton Events at HERA** [12]

[25] **Events with an Isolated Lepton (Electron or Muon) and Missing Transverse Momentum at HERA** [12]

[26] **Combined Electroweak and QCD Fit of Inclusive NC and CC Data with Polarised Lepton Beams at HERA** [12]

[27] **Measurement of** W **Production and** W **Polarisations at HERA** [12]

[28] **A General Search for New Phenomena at HERA** [12]

[29] **A Search for Excited Electrons in** ep **Collisions at HERA** [12]

[30] **Events with an Isolated Tau Lepton and Missing Transverse Momentum at HERA** [12]

[31] **Search for Single Top Production at HERA** [12]

[32] **Isolated Photon Production in Deep Inelastic Scattering at HERA**, Carsten Schmitz, PhD Thesis, University of Zürich (2007) available at *http://www-h1.desy.de/publications/theses_list.html*.

[33] Physik-Institut, University of Zürich, Annual Reports 1996/7 ff.; available at *http://www.physik.unizh.ch/reports.html*.

[34] **A Vertex Trigger based on Cylindrical Multiwire Proportional Chambers**, J. Becker, K. Bösiger, L. Lindfeld, K. Müller, P. Robmann, S. Schmitt, C. Schmitz, S. Steiner, U. Straumann, K. Szeker, P. Truöl, M. Urban, A. Vollhardt, N. Werner, D. Baumeister, S. Löchner, and M. Hildebrandt, physics/0701002, Nucl.Instr.Meth. **A586** (2008), 190.

[35] Preliminary results presented by members of the H1-collaboration at the 2008 Workshop on Deep Inelastic Scattering (DIS 2008), London, April 7-11, 2008; available at *http://www-h1.desy.de/publications/H1preliminary.short_list.html*

[36] A. Gehrmann-De Ridder, T. Gehrmann, and E. Poulsen, Phys.Rev.Lett. **96** (2006), 132002; Eur.Phys.J.**C47** (2006), 395.

[37] A. Gehrmann-De Ridder, G. Kramer and H. Spiesberger, Nucl.Phys. **B578** (2000) 326.

[38] A. Gehrmann-De Ridder, T. Gehrmann and E. Poulsen, Eur.Phys.J. **C47** (2006) 395 [hep-ph/0604030].

[39] D. Buskulic *et al.* [ALEPH Coll.], Zeitschrift für Physik **C69** (1996) 365.

[40] A. Aktas *et al.* [H1-Coll.], Eur.Phys.J. **C38** (2005) 437.

[41] M. Fontannaz, J. P. Guillet and G. Heinrich, Eur.Phys.J. **C21** (2001) 303.

[42] A. V. Lipatov and N. P. Zotov, Phys.Rev. **D72** (2005) 054002.

8 High-precision CP-violation Physics at LHCb

R. Bernet, A. Büchler, N. Chiapolini, V. Hangartner, C. Salzmann, S. Steiner, O. Steinkamp, U. Straumann, J. van Tilburg, A. Vollhardt, D. Volyanskyy, A. Wenger

in collaboration with: The silicon tracking group of LHCb: University of Lausanne; Max Planck Institute, Heidelberg, Germany; University of Santiago de Compostela, Spain; and Ukrainian Academy of Sciences, Kiev, Ukraine.

The full LHCb collaboration consists of 49 institutes from Brazil, China, France, Germany, Ireland, Italy, Netherlands, Poland, Romania, Russia, Spain, Switzerland, Ukraine, U.K., and U.S.A.

(LHCb)

LHCb (1; 2) is a dedicated B-physics experiment that is currently being set up at the new 14 TeV proton-proton collider LHC at CERN. The installation of the detector is almost completed and its commissioning is in good progress. The experiment is expected to see the first proton-proton collisions from the LHC in summer 2008.

The main goal of LHCb is to perform precision measurements of CP violating processes in the B meson systems and to search for rare B decays. These measurements provide a powerful tool to search for signs of physics beyond the Standard Model. They are complementary to the direct searches at the high energy frontier that will also be performed at the LHC. Since CP violating asymmetries are generated through processes that involve internal loops of virtual particles, they are very sensitive to contributions from the new particles that are predicted in most extentions of the Standard Model.

Figure. 8.1 shows a vertical cross section through the LHCb detector. One of the crucial tasks in LHCb is the efficient and precise reconstruction of the trajectories and momenta of the charged particles that are generated in the decays of the B mesons. The

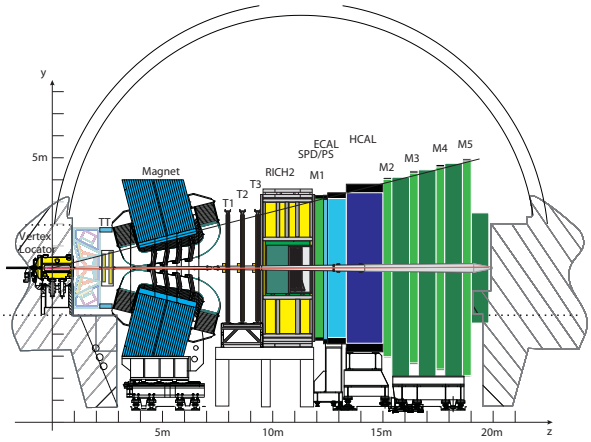

Figure 8.1:
Vertical cross section through the LHCb detector.

tracking system consists of a silicon-microstrip vertex detector (VELO) and four planar tracking stations: TT (Tracker Turicensis[4]) upstream of the LHCb dipole magnet and T1-T3 downstream of the magnet. The TT has an active area that is 160 cm wide and 130 cm high and is covered by four layers of silicon micro-strip detectors. In the much larger stations T1-T3 two detector technologies are employed: A 120 cm wide and 40 cm high region in the centre of the stations is covered with silicon micro-strip detectors (Inner Tracker,

[4]Initially, TT stood for "Trigger Tracker" since this was the only tracking station that was used in the trigger. The name was changed after a revision of the LHCb trigger philosophy, which resulted in all tracking stations being used in the trigger.

IT), whereas the outer part of these stations is covered by straw drift-tube detectors. Other components of the LHCb detector are two ring-imaging cherenkov detectors (RICH1 and RICH2), calorimeters (SPD,PS,ECAL,HCAL) and muon chambers (M1-M5).

8.1 The Zürich Group in LHCb

Our group has a leading rôle in the design, construction and operation of the LHCb Silicon Tracker, which comprises the Tracker Turicensis (2; 4) and the Inner Tracker (3).

The Tracker Turicensis was entirely developed, designed and constructed in Zürich. In addition, we have been responsible for the design specifications, the procurement and the quality control of the silicon sensors and for the design and production of the optical digital readout link for both TT and IT. A large fraction of our efforts in 2007 was spent on the installation and commissioning of the TT detector and the readout electronics in the experiment. These efforts also included the development of the slow-control software for the TT.

In addition to these contributions to the detector, we completed a simulation study in preparation for physics analyses, we continued our participation in the production of the large samples of simulated data that are necessary for these studies, and we further improved the geometry description of the TT in the LHCb simulation software.

8.2 Tracker Turicensis

The TT station (see Fig. 8.2) contains 128 detector modules that are arranged in four detection layers. All modules are housed in a common light-tight and electrically and thermally insulating detector box. During operation, an ambient temperature of around 0°C will have to be maintained in the detector volume to mitigate the effects of radiation damage. In order to avoid condensation on the cold surfaces, the detector volume is continuously flushed with a steady flow of nitrogen gas. To facilitate access for the installation and maintenance of detector modules, the box is constructed from two halves that can be retracted horizontally from the LHC beam pipe.

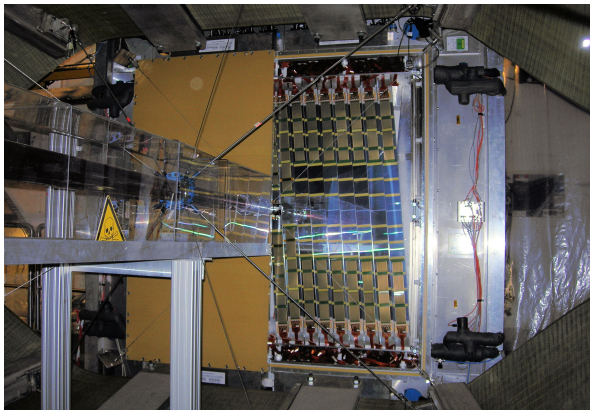

Figure 8.2: Photograph of the TT station viewed through the LHCb dipole magnet. One half of the detector box is open and the modules can be seen.

After extensive mechanical and thermal testing in Zürich, the detector box, without modules, had been shipped to CERN and installed in the experiment at the end of 2006. Throughout 2007, various tests were then performed on the still empty detector box, to commission the cooling system, to demonstrate that the design temperature can be reached everywhere in the detector volume, and to determine the flow of nitrogen necessary to avoid condensation. Automatic safeguards were implemented to protect the sensitive detector modules against potential failures of the cooling system or the nitrogen supplies.

Several geometrical surveys were performed to determine the precise positioning of the detector box in the experiment, both without and with the LHCb dipole magnet being switched on. Without magnetic field, the position of the box was found to agree with its nominal position within the measurement pre-

Figure 8.3: A. Büchler (left) and J. van Tilburg (right) during the installation of detector modules.

cision of ± 100 μm. However, a shift by several hundreds of micro-meters was found when the magnet was switched on, despite the fact that the detector is built from non-magnetic materials. This effect will be investigated further. Photogrammetric measurements were performed to determine and adjust the positions of the so-called balconies, on which the detector modules are mounted inside the detector volume. The results of these surveys are now being implemented in the software description of the detector geometry (see below).

The production and quality assurance of the TT detector modules was completed end of March 2007. Out of the 150 modules that were started, only two had to be rejected because of excessive leakage currents. All other modules are of detector-grade quality, such that we now have 20 spare modules of good quality on top of the 128 modules that are needed to fully equip the detector. The detailed results of the quality assurance tests were used to determine which modules to install at which position in the detector and which modules to keep as spares. Typically, the best modules were installed close to the LHC beam pipe, where particle densities are highest and where an excellent detector performance is most important for the physics goals of the experiment.

The modules were installed in several batches. After each installation campaign, bias-voltage tests and readout tests were performed. This permitted to identify and solve potential problems before the next batch of modules was installed. A few photographs from the module installation are shown in Fig. 8.3. By the end of April 2008, all detector modules were installed and more than 94% of the readout channels were fully debugged and operational.

8.3 Readout electronics

TT detector modules have either two or three readout sectors with 512 readout strips each. In total, the TT has more than 143'000 readout channels, to which 130'000 readout channels from the Inner Tracker have to be added. The analog signals from the detectors are transmitted via short copper cables to custom made electronics crates that are located at a few meters from the detectors. Here, the signals are digitised, multiplexed and prepared for optical transmission to the LHCb electronics barrack. The digitizer boards on which the processing of the signals takes place were produced in industry and then tested in Zürich. Two problems were identified on these boards, which made it necessary to go through a repair cycle at the assembly company. The first problem concerned the ADC chip, which had a much higher input bandwidth than was quoted in the data sheets, leading to an excessive sensitivity to high-frequency noise. This problem could be fixed by adding a simple first-order low-pass filter at the input of each ADC. The second problem was that a significant fraction of the VCSEL diodes was damaged during the assembly of the boards. All effected VCSELs were replaced. The digitizer boards were finally installed in the experiment in the second half of 2007.

8.4 Slow-control software

A general software framework for the slow-control of the detectors is provided by the LHCb collaboration. However, the components of this framework have to be adapted to the specific needs of the individual detectors. For example, so-called data points have to be built, which provide the interfaces to specific hardware components, user interfaces have to be defined, and a detector hierarchy has to be set up. The latter defines the interactions between different detector components and makes it possible to address and control different subsections of the detector. An important aspect of the slow-control is the handling of errors and alarms. The implementation of this software for TT is progressing well.

8.5 Physics studies

A detailed software description of the detector geometry is required for the generation of simulated data as well as for data reconstruction. The geometry description of the TT has been completely revised over the last months to provide an additional level of detail to the description of the active detector elements and to make the code more flexible and easier to maintain. For example, the new detector description makes it possible to correct for a possible mis-alignment of individual silicon sensors, whereas in the old description detector modules, consisting of several sensors, could only be aligned as a whole.

We continued to contribute to the generation of the large samples of simulated data that are required for physics studies. Using computer resources in Zürich and at the CSCS in Manno, about 2.75 Million events were generated. We also participated in the development and maintenance of the GRID software that is used to steer the world-wide data generation and analysis effort.

A Monte-Carlo simulation study of the decay mode $B_s^0 \to J/\psi\eta'$ was continued, and completed in summer 2007 (6). The time-dependent measurement of the CP asymmetry in this decay can be used to determine the phase of $B_s^0\overline{B^0}_s$ oscillations (i.e. the CKM angle χ). Since this phase is predicted to be very small in the Standard Model, it provides a sensitive probe for contributions from physics beyond the Standard Model (7). The simulation study consisted of an optimisation of the event selection criteria, followed by an estimation of the sensitivity of the experiment to the underlying physics parameters. Selection cuts were optimised using a multi-variate grid search on large samples of signal and background events. The results of this study were used to simulate a large number of toy experiments to estimate the expected sensitivity to the CKM angle χ. A sensitivity of 0.04 rad was found for one nominal year of data taking. The physics studies will be extended to other interesting decay channels, for example the rare decay $B_s^0 \to \mu^+\mu^-$.

[1] LHCb technical proposal, CERN/LHCC 998-4.

[2] LHCb Reoptimised Detector Technical Design Report, CERN/LHCC 2003-030.

[3] LHCb Inner Tracker Technical Design Report, CERN/LHCC 2002-029.

[4] Layout and expected performance of the LHCb TT station, J. Gassner, M. Needham, O. Steinkamp, LHCb note 2003-140.

[5] The Mechanical Design of the LHCb Silicon Trigger Tracker, J. Gassner, F. Lehner, S. Steiner, LHCb note 2004-110.

[6] The Trigger Tracker and a Monte Carlo Study of the $B_s^0 \to J/\psi\eta'$ Decay in the LHCb Experiment, D. Volyanskyy, PhD thesis, Universität Zürich (2007).

[7] J.P. Silva and L. Wolfenstein, Phys. Rev. **D 55** (1997) 5331.

9 Particle physics with CMS

E. Alagöz, C. Amsler, V. Chiochia, Hp. Meyer, C. Regenfus, P. Robmann, J. Rochet, T. Rommerskirchen, A. Schmidt[5], T. Speer[6], S. Steiner, D. Tsirigkas, and L. Wilke

In collaboration with: ETH - Zürich, Paul Scherrer Institut (PSI) and the CMS Collaboration

We have been involved in the design, construction and test of the CMS barrel pixel detector since many years. In particular, we have conducted various performance tests on beams at CERN (1). The position resolution, the Lorentz angle and the detection efficiency were determined on highly irradiated pixel prototypes. We also deliver the offline software for reconstructing and simulating hits and tracks in the CMS pixel (and strip) detectors, and contribute to the data quality monitoring and alignment codes. The group is furthermore active in the development of algorithms required to efficiently tag B-hadrons, using the pixel vertex detector. The year 2007 and early 2008 were dedicated to the completion of the pixel hardware and to the preparation of the software for data taking and data analysis.

The pixel detector is currently being completed in our institute and at PSI. The institute's workshop manufactured the two detector support structure half-shells for the pixel detector. Figure 9.1 shows the third layer of the final support structure with the mounted pixel detector modules. The production of the final supply tube half-shells is also completed. The electrical power and control lines, the optical signal lines and the cooling fluid are transferred across the supply tubes to the pixel detector. Figure 9.2 shows a supply tube half-shell. The structure consists of thin stainless steel tubes and inner and outer aluminium flanges. The tubes supply the detector with the cooling fluid. The gaps are filled with foam. The power and slow control leads are embedded in the supply tube body. Our electronics workshop manufactured all parts and the detector front end control system. The system consists of four communication and control unit boards, each controling a quarter of the detector with eight barrel readout sectors.

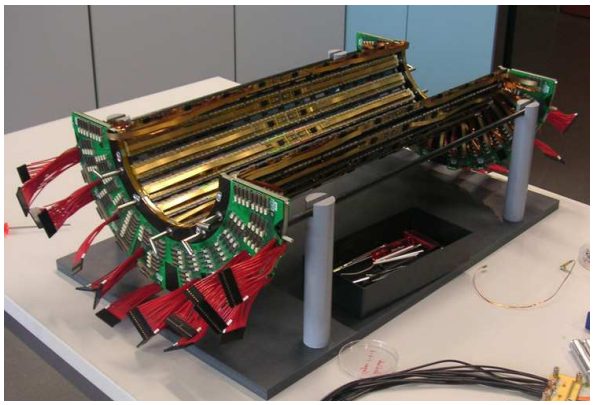

Figure 9.1: Support structure of the third (outer) layer with pixel detector modules.

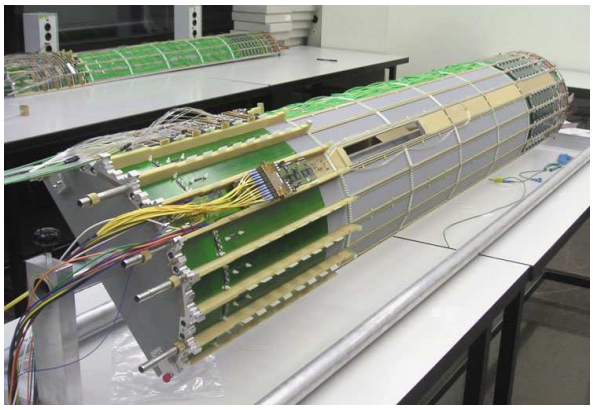

Figure 9.2: Supply tube half-shell during the installation of the electronics boards, the optohybrids and optical fibres. A fully equipped half-shell can be seen in the back.

[5]Since 1 September 2007
[6]Until 31 August 2007, now at Brown University

A final pixel sensor test had been performed at CERN in autumn 2006. We used a beam telescope with four pixel sensors, two in front and two behind the pixel sensors under test. The 52 $\times$ 80 pixel device had the final CMS dimensions 150 $\times$ 100 μm^2 with a thickness of 285 μm. They were bump-bonded to final CMS pixel readout chips. A PIN diode (3 $\times$ 6 mm^2) was used as a trigger. Irradiated sensors were kept at $-10^{\circ}\mathrm{C}$ in a cooling box with two Peltier elements. The experimental setup was placed in a Helmholtz superconductor magnet, providing a transverse field of 3T, and was exposed to a 150 GeV π^- beam. Data were taken with and without magnetic field for several bias voltages. The purpose of the test was to compare real data with the predictions obtained from our previous runs which used pixels of different dimensions and a magnetic field parallel to the incident pions (2).

The analysis of these data was performed in 2007, involving in particular a careful alignment procedure of the detectors to obtain the best possible resolution in the measurement of the directions of the incident pions. The charge collection in the test module is shown in Fig. 9.3 for several irradiated and unirradiated samples at 200 V bias. One observes a decrease of the collected charge for higher irradiation fluences. The collected charge is reduced to 46 % for fluences of $6.2 \times 10^{14}\mathrm{n_{eq}cm}^{-2}$ which will be absorbed by the CMS pixel sensors after two years of run at full LHC luminosity. The collected charge is reduced by defects due to radiation damage, which work as charge trapping centers. The charge loss is larger in the magnetic field since the drift length of the electrons increases due to Lorentz deflection. Increasing the bias voltage can recover some of the lost charge (Fig. 9.4), however at the expense of a reduced drift path, and hence reduced charge sharing, which in turn decreases the accuracy of the position resolution.

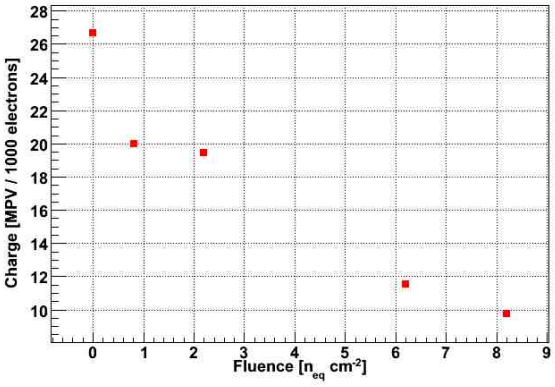

Figure 9.3: Charge collection efficiency for unirradiated and irradiated pixel sensors at 200 V, as a function of fluence.

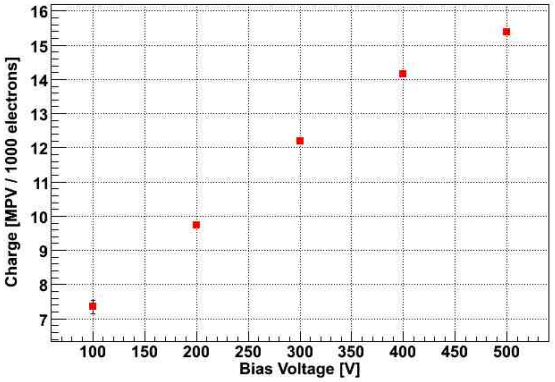

Figure 9.4: Charge collection efficiency for heavily irradiated pixel sensors ($8\times10^{14}\mathrm{n}_{eq}\mathrm{cm}^{-2}$) as a function of bias voltage.

Several new features have been implemented in the pixel software, such as a precise description of the material thickness, especially in the complicated regions of the pixel end-caps. Online pixel calibration runs will provide in real time gain response functions for each channel. The size of the calibration tables was reduced substantially to comply with the memory requirements of the CMS reconstruction programs. Detailed simulations have shown that such reductions will have negligible effects on position resolution and b-tagging efficiency.

The alignment of the tracking detectors is a major challenge in the early phase of the experiment. Tracker misalignment (e.g. due to imprecise mounting of sensors or moving structures due to thermal and magnetic field effects) will impair the hit, track and vertex reconstructions, and will decrease the b-tagging efficiency. We have developed a simple algorithm relying on the presence of a secondary vertex and taking the separation between primary and secondary vertex as discriminator. This algorithm does not require a dedicated calibration, is simple and robust enough to be used in the early stage of the experiment. However, the secondary vertex finding efficiency is only 55%. The detector alignment procedure will quickly improve as soon as data from resonances such as J/ψ and gauge bosons become available.

We made important contributions to track reconstruction and b-flavour tagging in fast simulation and are responsible for the interface and maintenance of the b-tagging algorithms in a fast simulation software. Figure 9.5 demonstrates the impressive agreement in terms of b-tagging efficiency and charm mistagging rate, comparing fast and full detector simulations.

In the pixel sensors the electrons produced by ionizing particles experience a Lorentz force and drift perpendicular to the 4T magnetic field and the bias electric field. This leads to a shift in the measured coordinates which can be up to 120 μm. This shift has been measured for un-irradiated sensors. However, during LHC operation the bias voltage will be increased to compensate for radiation damage (see Fig. 9.3) and hence the Lorentz deflection angle will decrease. Furthermore, each detector module will have a different evolution due to non uniform irradiation. Therefore the Lorentz drift needs to be monitored directly from data. Figure 9.6 shows a simulation of the coordinate shift d as a function of depth z in the pixel sensor at which the charge was produced. The average shift can be determined for a given depth with a large number of well-measured tracks (Fig. 9.7). The slope is the tangent of the Lorentz angle. Such a measurement is done independently for the eight module rings in the three detector layers. Studies for different input values of the Lorentz angle in the detector simulation were performed, as well as studies on the influence of misalignment.

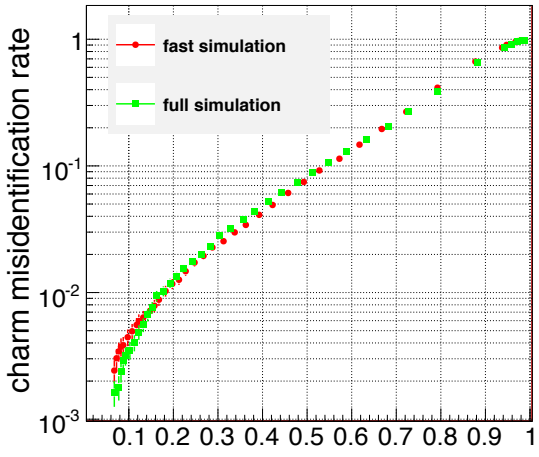

Figure 9.5: Charm mistagging rate vs. b-tagging efficiency in fast and full detector simulations.

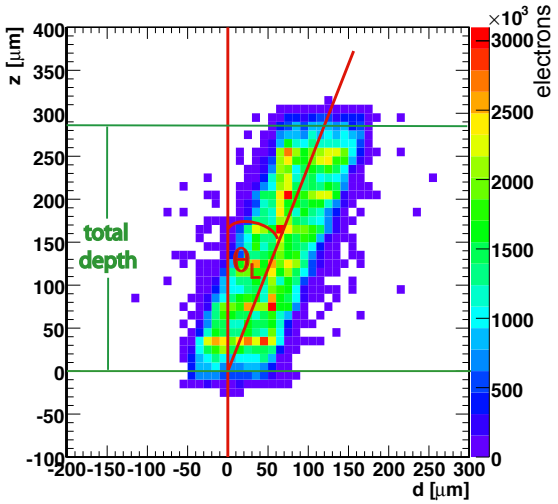

Figure 9.6: Depth z at which the drift electrons were produced vs. readout coordinate d (simulation for muon tracks crossing the pixel detector at a pseudo-rapidity η=2).

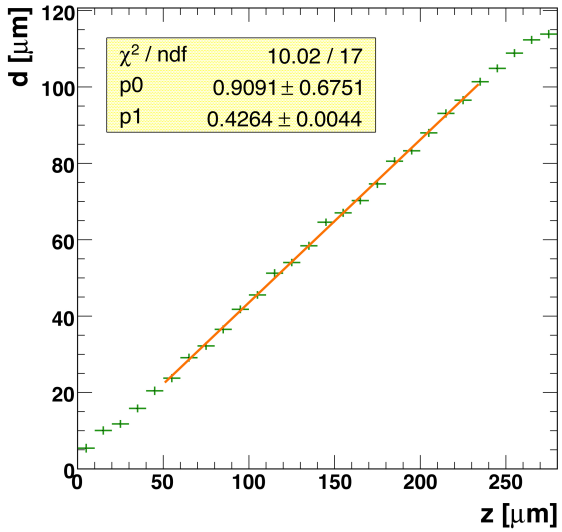

Figure 9.7: Average drift of electrons d as a function of the production depth z in the silicon sensor bulk. The solid line shows the fit.

During the first two years of LHC operation we will concentrate on b-physics issues which can be performed at low luminosity. In particular, we will study the decay $B_s^0 \rightarrow (J/\psi)\phi \rightarrow \mu^+\mu^- K^+K^-$ and measure the lifetimes of the CP-eigenstates B_s^H and B_s^L. This channel has been chosen as a benchmark channel by the CMS collaboration (3). A dedicated trigger for B-mesons decaying into two muons via a J/ψ intermediate states was developed, based on the long time of flight of the B-mesons. The secondary vertex of the two muons is reconstructed applying quality cuts on the decay length significance, and on the invariant mass of the two muons. We developed an analysis strategy for the first 100 pb^{-1} expected at the LHC in 2009. The first step is to measure the detector performance using the well known channel $B_d \rightarrow J/\psi K^* \rightarrow \mu^+\mu^- K^+\pi-$. This channel has very similar properties as the B_s-channel and all parameters have been measured to high precision by BaBar and Belle.

We are also preparing a search for supersymmetry which might be observed early at the LHC. A prominent signature is the presence of multiple jets + high missing transverse energy (MET) + two or more b-jets. The potential background stems from $t\bar{t}$, W + jets, Z^0 + jets and QCD events. An interesting process is the light Higgs-boson h-decay in SUSY processes, $\tilde{q} \rightarrow \tilde{\chi}_2^0 q, \tilde{\chi}_2^0 \rightarrow \tilde{\chi}_1^0 h, h \rightarrow b\bar{b}$, where χ_1^0 and χ_2^0 are neutralinos (4). The former is stable in R-parity conserving SUSY and therefore leads to a large missing energy.

We have simulated this channel by first requiring from the online trigger and at least 3 jets. In the offline analysis we require more than 5 energetic ($>$ 30 GeV) jets and a missing transverse energy of at least 240 GeV. A relevant parameter is the average direction of particles associated with a high energy jet, in particular its azimuthal angle ϕ transverse to the incident beam directions. The angles $\Delta\phi$ between the direction of the missing energy and those of the two most energetic jets is required to be at least 12°. From measurements of the impact parameters we also keep events with two b-jets. The result is shown in Fig. 9.8 which displays the predicted $b\bar{b}$ invariant mass distribution for an integrated luminosity of 100 pb^{-1}, after all cuts. The $h \rightarrow b\bar{b}$ signal (8 $\pm$ 1 events) shown by the red histogram is only a small contribution to all SUSY events. The main background stems from $t\bar{t}$ and QCD events, while contributions from W- and Z^0-decays associated with jet production are negligible.

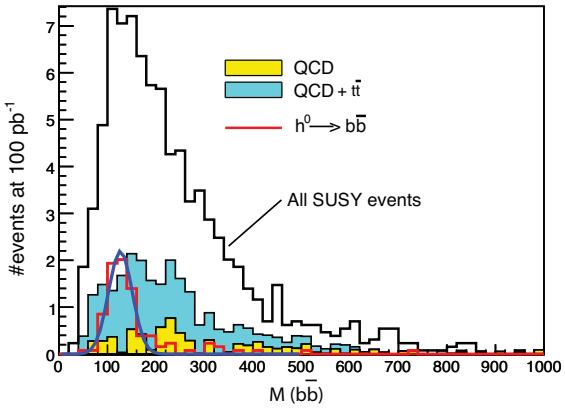

Figure 9.8: Invariant mass of two b-tagged jets after all selection cuts for SUSY and for background events (simulation). The red curve shows the fit to $h \rightarrow b\bar{b}$.

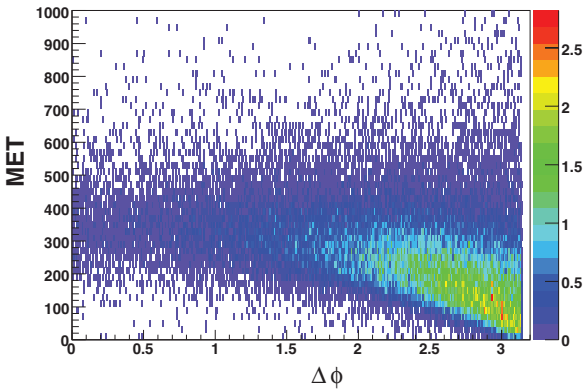

Figure 9.9: Missing transverse energy (MET) vs. $\Delta\phi$ for the LM1 point in the mSUGRA parameter space.

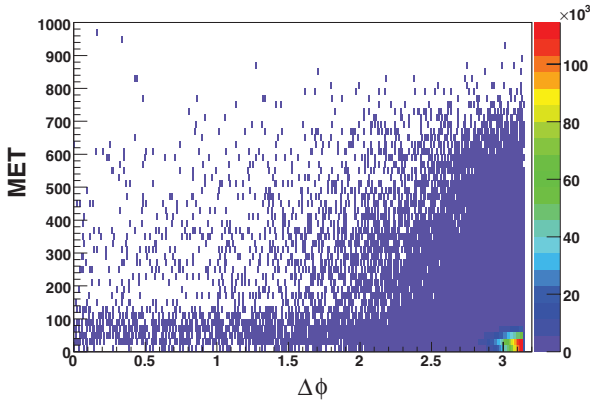

Figure 9.10: MET vs. $\Delta\phi$ for QCD events ($120 < p_T < 1000$ GeV/c).

For an integrated luminosity of 100 pb^{-1} the significance of the signal peak (43 ± 2 events) is about 8σ.

Figures 9.9 and 9.10 show the dependence of MET on $\Delta\phi$, the angle between the two most energetic jets, for SUSY and QCD events. It appears that, for large missing energies, the two most energetic jets are emitted in opposite directions (large $\Delta\phi$) for QCD events, while for the popular LM1-point of SUSY/mSUGRA they are more isotropically distributed. For the latter there is also a strong correlation between MET and $\Delta\phi$ (green/yellow region in Fig. 9.9). These features can be used to further decrease the QCD background.

The installation of the pixel detector in CMS is scheduled for May 2008. However, pixel readout tests have already been made in the CMS experimental area with a panel of the endcap pixel detector. Runs with several readout thresholds were recorded for the first time in March 2008 on the CERN TIER 0 storage, using the global CMS data acquisition, and were analyzed with the pixel data quality monitoring software. Results were in line with expectations. Our software codes will be deployed for the global run with the 3.8 T magnetic field scheduled in June 2008, just before LHC is expected to deliver its first beams.

[1] Y. Allkofer *et al.*. Nucl. Instrum. Meth. in Phys. Research **A 584** (2008) 25.

[2] A. Dorokhov *et al.*, Nucl. Instr. Meth. in Phys. Research **A 530** (2004) 71;
A. Dorokhov *et al.*, Nucl. Instr. Meth. in Phys. Research **A 560** (2006) 112;
V. Chiochia *et al.*, IEEE Trans. Nucl. Sci. **52** (2005) 1067.

[3] The CMS collaboration, "CMS Physics Technical Design Report Volume II:
Physics Performance", CERN/LHCC 2006-021, CMS TDR 8.2, 2006.

[4] F. Moortgat, P. Olbrechts, L. Pape and A. Romeyer, CMS Note 2006/090.

10 Superconductivity and Magnetism

D.G. Eshchenko, H. Keller, R. Khasanov (till December 2007), F. La Mattina, A. Maisuradze, J. Roos, S. Strässle, St. Weyeneth, B.M. Wojek, C. Duttwyler (Master student), U.. Mosele (Master student), M.V. Eremin (visiting scientist), V.B. Graneli (visiting scientist), A. Ivanshin (visiting scientist), B. Kochelaev (visiting scientist), R. Pusniak (visiting scientist), A. Shengelaya (visiting scientist)

Emeritus members:
Prof. K.A. Müller (Honorarprofessor), Prof. T. Schneider (Titularprofessor), Dr. M. Mali

in collaboration with: ETH Zürich (K. Conder, J. Karpinski), Paul Scherrer Institute (K. Conder, E. Morenzoni), Max-Planck-Institute for Solid State Research Stuttgart (A. Bussmann-Holder), IBM Rüschlikon Research Laboratory (J.G. Bednorz, S.F. Alvarado), University of Geneva (Ø. Fischer, J.M. Triscone), University of Rome (D. Di Castro), Kazan State University (A. Dooglav, M.V. Eremin, V. Ivanshin, B.I. Kochelaev), Polish Academy of Sciences (R. Puzniak), University of Belgrade (I.M. Savić), Tbilisi State University (A. Shengelaya), Russian Research Centre "Kurchatov Institute" (V.G. Storchak), Osaka University (S. Tajima), University of Tokyo (T. Sasagawa, H. Takagi), University of British Columbia (J.H. Brewer), Iowa State University (A. Kaminski).

We continued our research on magnetic and electronic properties of novel materials during the last year. In our efforts we profit from synergy effects in combining complementary experimental techniques, including muon-spin rotation (μSR), electron paramagnetic resonance (EPR), nuclear magnetic resonance (NMR), nuclear quadrupole resonance (NQR), as well as SQUID and torque magnetometry. Most prominent examples of our studies are presented in the following sections.

10.1 Two-gap superconductivity in cuprate superconductors

In collaboration with other research groups we recently performed two decisive experiments on cuprate high temperature superconductors (HTS's) which challenge theoretical models based on purely electronic mechanisms. From muon spin rotation (μSR) experiments the temperature dependence of the superfluid density has been determined from which clear conclusions on the pairing symmetry can be extracted. The experimental results for three different cuprate families disclose generic trends for HTS's, namely the coexistence of an s-wave and a d-wave gap in the CuO_2 planes and a predominantly s-wave gap along the c-axis (1; 2; 3) (Figs. 10.1 and 10.2 show representative results). These findings are not compatible with approaches that concentrate on the planes only, but consistent with early predictions where the 3D nature of high temperature superconductivity was suggested to be manifest in coupled gaps (4; 5). In addition, the existence of the s-wave gap is in strong support of ideas that the lattice plays a crucial role in HTS's. These latter conclusions are in accord with oxygen isotope effect (OIE) experiments where not only OIE's on the superconducting transition temperature but also on the magnetic penetration depth (6), the superconducting gaps, the Néel temperature, and the spin glass temperature have been observed (7). Throughout the whole phase diagram of cuprates OIE's exist which are sign reversed for the superconducting properties as compared to the magnetic states. The strong doping dependence of these OIE's has been shown to stem from renormalizations of the kinetic energy

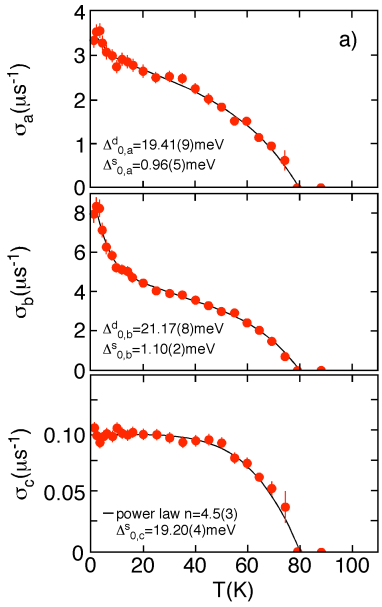

Figure 10.1: Temperature dependence of the μSR relaxation rates $\sigma_a \propto \rho_a$, $\sigma_b \propto \rho_b$, and $\sigma_c \propto \rho_c$ of single crystals of $YBa_2Cu_4O_8$ measured along the crystallographic directions a, b, and c (ρ_a, ρ_b, and ρ_c are the corresponding superfluid densities) [3]. Individual values of the s- and d-wave gap are indicated. The full lines are results from a power law dependence [2].

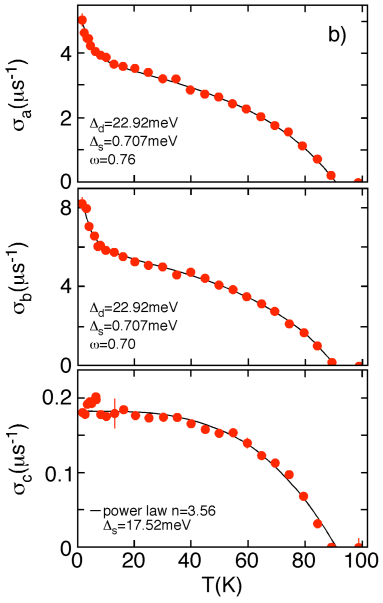

Figure 10.2: The same as in Fig. 10.1 but for $YBa_2Cu_3O_{7-\delta}$ [2].

caused by polaron formation (8). This interpretation is consistent with ideas that led to the discovery of high temperature superconductivity, namely the concept of Jahn-Teller polarons (9) which might provide a much better glue to the electron pairing than conventional electron-phonon coupling. Since both above mentioned experiments are direct, bulk sensitive, and unambiguous and have been carried through systematically for different cuprate families and as functions of doping, we conclude that the order parameter in cuprates is much more complex than just d-wave symmetry, the third dimension, i.e., physics involving the c-axis are of outermost importance, lattice effects in terms of polaron formation crucially dominate the whole phase diagram.

[1] R. Khasanov, A. Shengelaya, A. Maisuradze, F. La Mattina, A. Bussmann-Holder, H. Keller, and K. A. Müller, Phys. Rev. Lett. **98**, 057007 (2007).

[2] R. Khasanov, S. Strässle, D. Di Castro, T. Masui, S. Miyasaka, S. Tajima, A. Bussmann-Holder, and H. Keller, Phys. Rev. Lett. **99**, 237601 (2007).

[3] R. Khasanov, A. Shengelaya, A. Bussmann-Holder, J. Karpinski, H. Keller, and K. A. Müller, J. Supercond. Nov. Magn. **21**, 81 (2008).

[4] K.A. Müller, Nature (London) **377**, 133 (1995).

[5] K.A. Müller and H. Keller, in **High T_c Superconductivity 1996: Ten Years after the Discovery** (Kluwer, Dordrecht, 1997) p. 7.

[6] See e.g., H. Keller, in **Superconductivity in Complex Systems**, eds. K.A. Müller and A. Bussmann-Holder (Springer Series Structure and Bonding) **114**, 143 (2005); and refs. therein.

[7] R. Khasanov, A. Shengelaya, D. Di Castro, E. Morenzoni, A. Maisuradze, I.M. Savic, K. Conder, E. Pomjakushina, H. Keller, arXiv:0711.2257.

[8] A. Bussmann-Holder and H. Keller, in **Polarons in Advanced Materials**, eds. A.S. Alexandrov (Springer Series in Materials Science 103, Canopus Publishing, Bristol 2007), pp. 599.

[9] K.A. Müller, J. Phys. C: Condens. Matter **19**, 251002 (2007) and refs. therein.

10.2 Superconductivity and magnetism in $YBa_2Cu_3O_7/PrBa_2Cu_3O_7$ multi-layers

Heterostructures consisting of magnetic and superconducting layers juxtaposed to each other are ideal systems to investigate the interplay (coexistence, competition) of the two order parameters and to study possible interlayer coupling. These properties have been subject of intense research in the recent years. For instance in superlattices composed of one unit cell thick layers $YBa_2Cu_3O_7$ (YBCO) separated by $PrBa_2Cu_3O_7$ (PBCO) layers of variable thickness the critical temperature of the heterostructure has been found to decrease continuously as the PBCO thickness is increased indicating that coupling persists over distances of approximately 10 nm (1).

We used spin polarized low energy muons to investigate the local superconducting and magnetic properties of c-axis oriented $YBa_2Cu_3O_{7-\delta}$/ $PrBa_2Cu_3O_{7-\delta'}$/ $YBa_2Cu_3O_{7-\delta}$ tri-layers as well as of a $YBa_2Cu_3O_{7-\delta}$/ $PrBa_2Cu_3O_{7-\delta'}$ bi-layer system and single layer films of the constituents. Low energy μSR offers the unique possibility to measure local fields on a nanometer scale (2), to determine the spatial distribution of the magnetization throughout the layers, and to identify superconducting and magnetic fractions, quantities about which very little is known in multilayers.

In a series of measurements we investigated the response of the heterostructures to an external perturbation represented by a magnetic field applied parallel to the surface (and parallel to the ab-planes). In the trilayer we find that below the critical temperature of YBCO, a sizeable fraction of the PBCO buffer layer displays a diamagnetic shift characteristic of the superconducting state. This fraction is coexisting with an antiferromagnetic fraction.

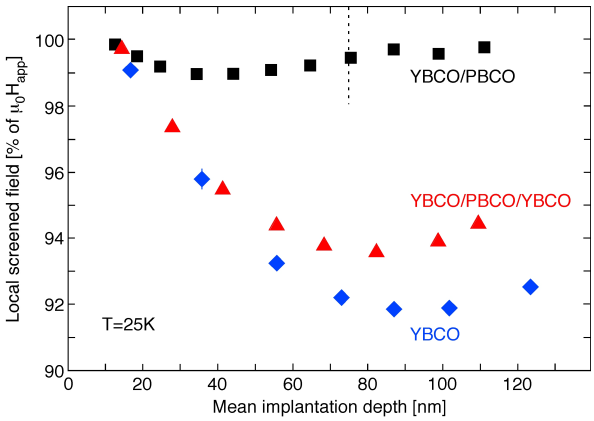

Figure 10.3: Depth dependence of the local screened magnetic field in the bi-layer (black squares) and tri-layer (red triangles) samples at T=25 K in the Meissner state. The dotted line indicates the top YBCO/PBCO interface. For comparison the depth profile of a 200 nm thick single layer of YBCO is also shown (blue diamonds).

A typical depth profile of the diamagnetically shifted field component is depicted in Fig. 10.3 at a temperature below the critical temperature of YBCO. In the YBCO/PBCO/YBCO film the monotonic decrease of the screened field in the top superconducting layer and the large shift in PBCO imply that unexpected large supercurrents with no dissipation are flowing through a 50 nm AF barrier to the bottom YBCO layer, which sustains the return flow. The absence of a second superconducting layer suppresses the back flow and hence the observed diamagnetic shift in PBCO, possibly indicating that the induced superfluid density in PBCO is much lower than in YBCO and that the effective penetration depth in PBCO is much larger than in the superconductor, where from our measurement we determine $\lambda_{ab} \simeq 200$ nm.

By applying a magnetic field perpendicular to the surface and to the ab-planes we observed the typical field distribution of a rigid vortex state in the top and bottom superconducting layer, reflecting the vortex supercurrents flowing in the ab-planes. From a detailed analysis of the field distribution observed at

various depths, we expect to quantify the amount of superfluid density induced in the barrier layer. Although the mechanism of our observation is not understood in detail at the moment, the results present the signature of a large proximity effect between two compounds with different electronic ground state, not expected on the base of conventional proximity theory. The results call for additional investigations. We plan to measure the effect as a function of the thickness of the single components and extend the investigations to other cuprates (e.g. of the 214 family) where we have recently observed similar effects with strongly underdoped barriers and where so-called giant proximity effects in the Josephson current have been reported (3).

[1] J.-M. Triscone and Ø. Fischer, Rep. Prog. Phys. **60**, 1673 (1997).

[2] E. Morenzoni, R. Khasanov, T. Luetkens, H. Prokscha, and A. Suter, J. Neutron Research **14**, 269 (2006).

[3] I. Bozovic, G. Logvenov, M. A. J. Verhoeven, P. Caputo, E. Goldobin, and M. R. Beasley, Phys. Rev. Lett. **93**, 157002 (2004).

10.3 Spectroscopic studies of novel electronic materials

10.3.1 Antiferromagnetic to superconducting phase transition in $Y_{0.98}Yb_{0.02}Ba_2Cu_3O_x$ for $x \simeq 6.4$ investigated by Yb^{3+} EPR

The antiferromagnetic (AF) to superconducting (SC) phase transition in $YBa_2Cu_3O_x$ for $x \simeq 6.4$ is subject of recent studies (1; 2; 3). Whereas superconductivity in $La_{2-x}Sr_xCuO_4$ emerges from a nonmetallic phase, the precursor phase for $YBa_2Cu_3O_x$ remains still controversial. A detailed study in the vicinity of the boundary between AF and SC phases is needed to understand whether the AF and SC phases coexist, compete, or are separated by a novel phase. We report on the detailed investigation of $YBa_2Cu_3O_{6.4}$ by the Yb^{3+} EPR probe across the transition from the AF to the SC state. The AF to SC phase transition was induced by varying the hole concentration p in the CuO_2 planes near the critical concentration $p = 0.05$ holes/Cu where superconductivity appears/vanishes. To change the value of p the well known effect of its dependence on the chain-oxygen order was used. It was found that the width of the distribution of the oxygen content x of any investigated powder sample is less than 0.02 (80% of the sample's powder grains have an oxygen content in this range). Within the doping range $x \simeq 6.37 - 6.47$ the Yb^{3+} EPR line is split into a broad and a narrow component, unambiguously indicating the presence of an electronic phase separation. By comparing this result with neutron investigations of Ref. (2) we could assign the broad and the narrow EPR line to the central mode and the damped mode of the Cu spin dynamics of the neutron spectra, respectively.

By studying the temperature dependence of the linewidth of the broad Yb^{3+} signal it was possible to estimate the energy of the central mode to $E \simeq 0.03$ meV above 20 K. Below 20 K this energy gradually drops to zero. Our present result is in full agreement with studies of Sanna **et al.** suggesting a stripe-like order of carriers for $x \simeq 6.37 - 6.47$ (1).

[1] S. Sanna, G. Allodi, G. Concas, A.D. Hillier, and R. De Renzi, Phys. Rev. Lett. **93**, 207001 (2004).

[2] C. Stock, W.J.L. Buyers, Z. Yamani, C.L. Broholm, J.-H. Chung, Z. Tun, R. Liang, D. Bonn, W.N. Hardy, and R.J. Birgeneau, Phys. Rev. B **73**, 100504 (2006).

[3] M. Sutherland, S.Y. Li, D.G. Hawthorn, R.W. Hill, F. Ronning, M.A. Tanatar, J. Paglione, H. Zhang, L. Taillefer, J. DeBenedictis, R. Liang, D.A. Bonn, and W.N. Hardy, Phys. Rev. Lett. **94**, 147004 (2005).

10.3.2 Charge effects in $LaBa_2Cu_3O_{7-\delta}$

The study of charge effects in cuprates by means of ^{139}La NMR/NQR on $LaBa_2Cu_3O_{7-\delta}$ powder samples was completed with measurements of the temperature dependence of the three ^{139}La NQR resonance lines in the normal conducting phase. We observed a smooth increase of line frequencies with decreasing temperature that can be simply attributed to the shrinking of the lattice. Moreover, the complex temperature behavior of the ^{139}La nuclear spin-spin relaxation (NSSR) rate in the normal conducting phase was reinvestigated in more detail. We performed new NQR-NSSR measurements on lose powder samples which had been exposed to dry air for some month, however belonging to the same batch as the aligned powder samples which were used in our earlier NMR-NSSR investigation on c-axis aligned powder samples (cast in epoxy) (1). The pronounced steps and plateaus in the temperature dependent NMR-NSSR rate observed previously (1) are not present in the new NQR-NSSR data. From these findings we conclude that the previously observed complex NSSR temperature dependence is dominated by the long term behavior of the dynamics related to oxygen diffusion and reordering in the CuO-chains of $LaBa_2Cu_3O_{7-\delta}$.

In addition we extended the temperature range of our measurements of ^{139}La NMR parameters on c-axis aligned powder samples down to 2 K. Most interestingly we found that the nuclear spin-lattice relaxation rate for a magnetic field orientation parallel to the c-axis follows the same nearly linear temperature dependence ($\propto T^{4/3}$) which we observed in our earlier investigations at higher temperatures in the superconducting phase.

[1] S. Strässle , J. Roos , M. Mali , K. Conder, E. Pomjakushina, and H. Keller,
Physica C **460-462**, 890 (2007).

10.4 3D-xy critical properties in the fluctuation regime of the superconductor MgB_2

The observation of thermal fluctuation effects have been limited in conventional low-T_c superconductors because the large correlation volume makes these effects very small compared to the mean-field behavior. By contrast, the high transition temperature T_c and small correlation volume in a variety of cuprate superconductors lead to significant fluctuation effects (1; 2). In MgB_2 the correlation volume and T_c lie between these extremes, suggesting that fluctuation effects will be observable if measurements are done carefully enough.

We analyzed reversible magnetization data of a high quality MgB_2 single crystal in the vicinity of the zero field transition temperature, $T_c \simeq 38.83$ K. Though MgB_2 is a two gap superconductor our scaling analysis uncovers below T_c remarkable consistency with 3D-xy critical behavior similar to the situation in the cuprate superconductors. For this reason the magnetic field induced finite size effect, whereupon the correlation length transverse to the applied magnetic field cannot grow beyond a limiting magnetic length L_H, can be verified and studied in detail. Indeed, as the magnetic field increases, the density of vortex lines becomes greater, but not indefinitely. The limit is roughly set by the proximity of vortex lines due to the overlapping of their cores. This finite size effect implies that in type II superconductors, superconductivity in a magnetic field is confined to cylinders with diameter L_H. Accordingly, there is below T_c a 3D to 1D crossover line. It circumvents the occurrence of the continuous phase transition in the (H,T) -diagram along the H_{c2}-lines predicted by the mean-field treatment (3).

[1] T. Schneider and J.M. Singer, Phase Transition Approach To High Temperature Superconductivity, (Imperial College Press, London, 2000).

[2] T. Schneider, in: The Physics of Superconductors, edited by K. Bennemann and J.B. Ketterson (Springer, Berlin), p. 111 (2004).

[3] S. Weyeneth, T. Schneider, N.D. Zhigadlo, J. Karpinski, and H. Keller, J. Phys.: Condens. Matter **20**, 135208 (2008).

10.5 Charge transfer processes during resistive switching in Cr-doped $SrTiO_3$

Current induced bistable resistance effects in metal-insulator-metal structures involving transition-metal oxides and more recently also perovskite oxides such as $SrTiO_3$ have attracted substantial interest because of their potential technological applications for non-volatile memory devices. We investigate single crystals of Cr-doped $SrTiO_3$ as a model system for perovskite oxides exhibiting resistive memory behavior in the current-voltage characteristic (I-V). We found evidence of charge transfer processes involving the Cr site during the resistive memory switching of Cr-doped $SrTiO_3$. Electroluminescence (EL) was observed in-situ during I-V measurements. Our luminescence measurements performed on $SrTiO_3$:Cr crystals at different stages of conductivity reveal that the light emission is associated with 3d intrashell transitions of Cr^{3+} on an octahedral lattice site. Electrically stimulated emission can be taken as proof of dynamic processes involving trapping and subsequent radiative decay of electrons at the Cr dopant sites. With increasing conductivity of $SrTiO_3$ the emission maximum changes from the predominant well known R-line to another intrashell transition of Cr^{3+}(5). We interpret this as being due to a geometrical change of the oxygen octahedron, through either distortion and/or a modified oxygen vacancy distribution. The EL in the final state, which occurs only when the memory cell is switched from the low- to the high-resistance state, can provide an important stimulus for the refinement of theoretical models by taking controlled and defined trapping centers into account. Even if some models of the resistive switching on $SrTiO_3$ are presently under discussion, a conclusion about the role and the nature of intrinsic defects or dopants has not been done. Extended defects like dislocations and local changes of the oxygen vacancy content has been proposed to be responsible for the conduction in $SrTiO_3$ (1; 2). Inhomogeneity of the crystal in the bistable conductive state has been shown experimentally (3) as a property arising from the forming procedure, and a phenomenological model (4) points out the requirement of extended non percolating domain structures. However a clear explanation of the role of the Cr dopant has not been incorporated in any models. We found an essential process describing the decreases of conductivity during the resistive switching, which involves the Cr site as a reversible trapping center for the conducting electrons (5).

[1] M. Janoush, G.I. Meijer, U. Staub, B. Delley, S.F. Karg, and B.P. Andreasson, Adv. Mater. **19**, 2232 (2007).

[2] K. Szot, W. Speier, G. Bihlmayer, and R. Waser, Nature Mater. **5**, 312 (2006).

[3] C. Rossel, G.I. Meijer, D. Brémaud, and D. Widmer, J. Appl. Phys. **90**, 2892 (2001).

[4] M.J. Rozenberg, I.H. Inoue, and M.J. Sánchez, Phys. Rev. Lett. **92**, 178302 (2004).

[5] S. F. Alvarado, F. La Mattina, and J.G. Bednorz, Appl. Phys. A **89**, 85 (2007).

11 Phase transitions and superconducting photon detectors

M. Reibelt, R. Dell'Amore, H. Bartolf, S. Siegrist, L. Gómez, A. Engel and A. Schilling

in collaboration with: Paul Scherrer Institute, University of Bern (K. Krämer), EPF Lausanne (H. Berger), Bhaba Atomic Research Center (G. Ravikumar), Forschungszentrum Karlsruhe (Th. Wolf, H. Küpfer), Universität Karlsruhe (K. Il'in), ETH Zürich (J. Karpinksi), Deutsches Zentrum für Luft- und Raumfahrt (H.-W. Hübers), University of Wellington (B. Ruck), Istituto Nazionale di Ricerca Metrologica I.N.RI.M Torino (C. Portesi), FIRST Lab ETH Zürich.

11.1 Physics of superconducting thin-film nanostructures and possible applications as fast single-photon detectors

Superconducting single-photon detectors (SSPD) which are based on a current-biased superconducting meander strip, have been attracting a lot of attention. They are extremely fast and very sensitive and could be used in such diverse areas as quantum encryption, infrared astronomy or spectroscopy. We are working on a better understanding of the detection principle and to shed a light on the underlying physics of superconducting nanostructures.

E-beam lithography

The performance of SSPD crucially depends on the quality of the lithographic processes during their production. The strip cross-section and the parameters characterizing the superconducting state have to be as homogeneous as possible along the entire length of the strip. Therefore, we are continuously working on improving our lithographic technologies. During the last year we have implemented a dry-etching step into our production process.

Our collaborating partners at the University of Karlsruhe produce high-quality NbN films with thickness typically between 4 and 10 nm. These films are prepared by DC-magnetron sputtering. In order to achieve homogeneous films with a high T_c the sapphire substrate needs to be heated to about 750°C. These high temperatures during film deposition prohibit the use of the lift-off technique. Our alternative approach starts from such extended films. Using e-beam lithography we then write the desired structure into a resist that is put on top of the NbN film. Reactive ion etching is then used to remove the unprotected areas of the NbN film.

After additional photolithography processes to make the necessary conduction paths for connecting the device to external electronics we obtain the final structures. In Fig. 11.1 we show an example of a meander structure with 200 nm wide and 10 nm thin strips. This

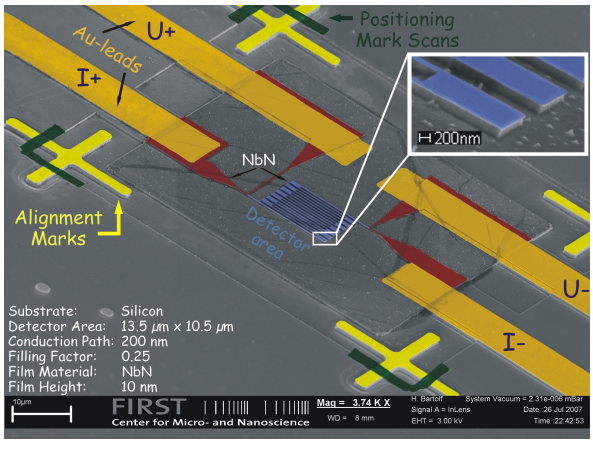

Figure 11.1: SEM picture of a 200 nm wide NbN meander on a Si substrate in false color representation to emphasize different elements.

meander showed excellent superconducting properties (1). Similar structures will be tested to demonstrate their potential as SSPD.

Critical-current density in NbN bridges

The detection model that has been previously described in detail requires bias currents of about 90% to 95% of the depairing critical-current density. Such high current densities can only be reached if the meander strip lines remain free of magnetic vortices, otherwise the dissipation-free current transport will be limited by the depinning of vortices. We have systematically measured critical-current densities in NbN bridges with widths ranging from 100 nm to 10 μm to shed light on the mechanism determining the critical-current density.

We have found that the experimentally determined critical-current densities in sub-μm wide bridges can be well described by the mean-field *Ginzburg-Landau* depairing critical current density (see Fig. 11.2 for a 300 nm wide bridge). Wider bridges deviate substantially from this temperature-dependence below a certain temperature. We interpret this reduction in critical-current density below the expectations for the depairing critical-current density as the entry of vortices due to self-field of the applied current. This can be qualitatively described with an edge-barrier model (2) taking into account edge effects in analogy to the *Bean-Livingston* surface barrier (3).

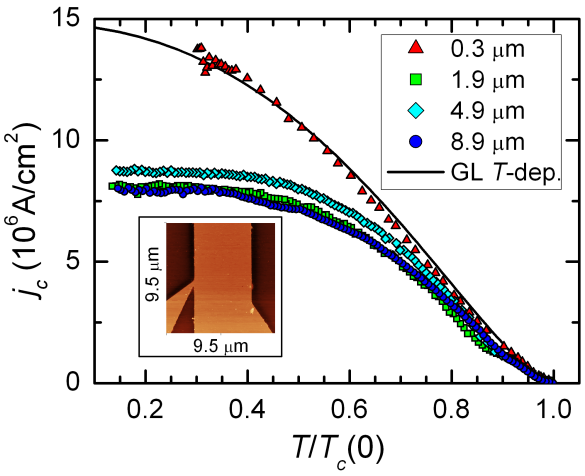

Figure 11.2: Critical current density j_c as a function of reduced temperature $T/T_c(0)$ for NbN bridges of different widths. The solid line is a fit of the Ginzburg-Landau depairing critical-current density to the data of the 300 nm wide bridge. The inset shows an AFM-image of the 4.9 μm wide bridge.

Transition metal nitrides

Currently, NbN is used as the standard material for these kind of single-photon detectors and in many respects it is a very good material. However, to increase the spectral range of these detectors and to check the validity of the detection model, the use of other superconducting materials would also be interesting. In 2007 a versatile magnetron sputtering machine has been installed in the FIRST lab at ETHZ. This has opened up the opportunity to prepare a whole range of elemental and composite superconducting thin films. We have already been able to prepare amorphous MoN films with $T_c \approx 6$ K. We will further optimize deposition parameters and characterize these films to evaluate their potential as an alternative to NbN.

11.2 Low temperature magnetic field dependence of the specific heats of V_3Si and $LuNi_2B_2C$

The differential-thermal analysis (DTA) method used in our laboratory is particularly suited to detect sharp phase transitions, e.g., first-order phase transitions, and it does not require large sample masses (4; 5). Since very high quality samples often only exist in form of small crystals, such a sensitive method is of high value. In addition, it is often desirable to choose a method that yields a high data-point density

within a reasonable measuring time. Common techniques, such as AC or relaxation methods, are sensitive but very time consuming. As an example, the relaxation method implemented in a commercial PPMS platform (Quantum Design) usually takes several *minutes* per data point for data acquisition while the DTA technique takes only approximately 3 *seconds* per data point, at an impressive data-point density of typically 170 data points per Kelvin. High resolution and high data-point density are needed for the observation of small and sharp effects.

In superconductors, not only the discontinuity in the specific heat at T_c contains valuable information about the superconducting state, but also the field dependence of this quantity below T_c is of utmost interest because it may be influenced by the symmetry of the order-parameter and perhaps also by other factors (6; 7; 8; 9).

V_3Si

In the standard theory of superconductivity the magnetic-field dependence of the specific heat in the mixed state is $\Delta c_p/T(H) = (c_p(H) - c_p(H=0))/T = \gamma H/H_{c2}(T)$ for $T \to 0$, where γ is the Sommerfeld coefficient characterizing the specific heat of the electronic system in the normal sate. In this classic scenario, $\gamma(H)$, a thermodynamic probe of the electronic density of states at low energy, is expected to be linear in H up to H_{c2} (10). At temperatures $T > 0$, the field dependence of $\Delta c_p/T$ is expected to be more complicated, and a non-linear behavior has been observed in a number of compounds.

We measured the specific heat of V_3Si for fields up to H=8.3 T. Fig. 11.3 shows two DTA data sets for $\mu_0 H = 0$ T and 6 T. The $\mu_0 H = 6$ T data show a structural martensitic transition taking place close to T_{c0}, which is nearly entirely suppressed by superconductivity in zero magnetic field. Figure 11.4 shows a small temperature interval around T=7.5 K for selected fields. The non-linear field dependence at low magnetic fields is already visible in this figure.

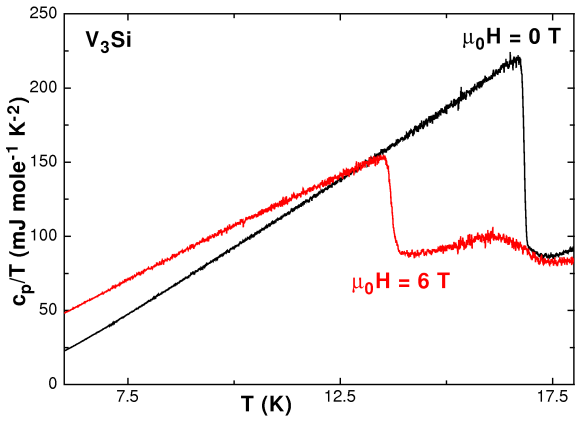

Figure 11.3: c_p/T-DTA data of a V_3Si single crystal for $\mu_0 H$=0 T and 6 T.

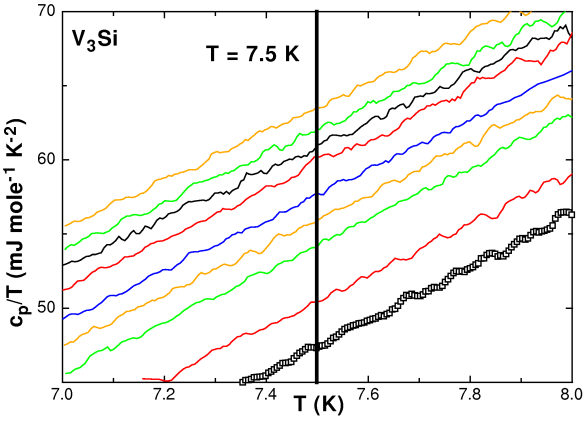

Figure 11.4: c_p/T-DTA data of V_3Si in a small temperature interval around T=7.5 K, starting with $\mu_0 H$=0 T (open circles) for the lowest curve and 4 T for the highest curve, $\mu_0 H$ increasing in intervals of 0.5 T.

Extracting the $c_p/T(H)$ data for a fixed temperature T=7.5 K results in the data plotted in Fig. 11.5(a), demonstrating the magnetic-field dependent specific-heat difference $\Delta c_p/T(H)$ of V_3Si (open circles). The dashed line is a guide to the eye and visualizes an approximately linear behavior above $\mu_0 H > 2$ T. It can clearly be seen that the data deviate from linearity below $\mu_0 H < 2$ T

where it is better described by a $H^{1/2}$ dependence. For comparison, we have plotted in the same figure the data of Ramirez (11) from a polycrystalline V_3Si sample. The deviation from linearity becomes very significant for low fields close to the lower critical field H_{c1}. In analogy to Ref. (11) we can fit our data to $\Delta c_p/T = A(H - H^*_{c1})^{1/2}$ with $H^*_{c1} = 0.2$ T being the field where magnetic flux starts to enter the sample, and $A \approx 8.6$ mJ mole^{-1} K^{-2} T$^{-1/2}$, in good agreement with the result of Ref. (11).

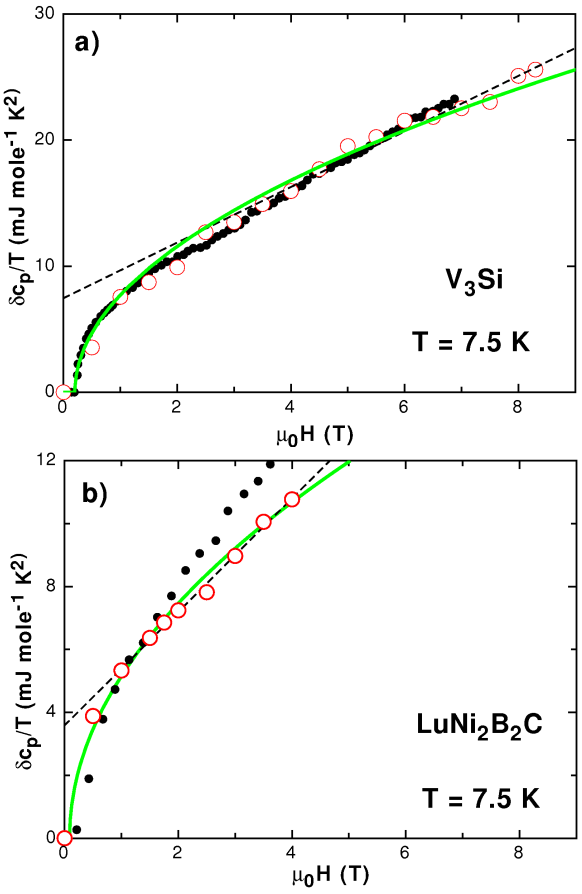

Figure 11.5: Magnetic-field dependence of the specific heat difference Δc_p/T at T=7.5 K for different crystals. The thick lines represent fits according to Δc_p/T=A(H-H^{1*}_{c1})$^{1/2}$ (see text). The dashed lines are guides to the eye to visualize the approximate linear behavior for the magnetic fields $\mu_0 H >$2 T in the case of V_3Si and $\mu_0 H >$1 T in the case of $LuNi_2B_2C$.
(a): data of a V_3Si single crystal obtained from DTA measurements (open circles), in comparison with the data of Ramirez [11](filled circles).
(b): data of a $LuNi_2B_2C$ single crystal obtained from DTA measurements (open circles), together with the data of Nohara et al. [12] (filled circles).

$LuNi_2B_2C$

Figure 11.5(b) shows in a similar way the magnetic field dependent $\Delta c_p/T$-DTA data for a $LuNi_2B_2C$ single crystal, obtained at a fixed temperature T=7.5 K. The dashed line is a guide to the eye and visualizes the linear behavior above $\mu_0 H > 1$T. Again it can clearly be seen that the data deviate from linearity below $\mu_0 H < 1$T where it is better described by a $H^{1/2}$ dependence. A fit according to $\Delta c_p/T = A(H - H_{c1})^{1/2}$ with $H_{c1} = 87$ mT ((13)) gives $A \approx 5.4$ mJ mole^{-1} K^{-2}T$^{-1/2}$.

For comparison we have reproduced the data of Nohara *et al.* (12) for $LuNi_2B_2C$ in Fig. 11.5. Again, our data confirm the observation that also in $LuNi_2B_2C$ $\Delta c_p/T$ is not linear in H.

These findings are noteworthy since both V_3Si and $LuNi_2B_2C$ are supposed to be s-wave systems. While the deviation of $\Delta c_p(H)/T$ from linearity and especially its approximate $\propto H^{1/2}$ dependence is usually interpreted as an indication for lines of nodes in the energy gap (8), one can state here that such a behavior as we observe in the s-wave superconductors V_3Si and $LuNi_2B_2C$ is likely a more a general phenomenon of type II superconductors.

11.3 Bose-Einstein condensation in $TlCuCl_3$?

$TlCuCl_3$ is a quantum- spin- $\frac{1}{2}$ system, that shows a gap between the ground state and

the first excited states for low magnetic fields $\mu_0 H_c \lessapprox 5.5\mathrm{T}$ and at low temperatures. At higher magnetic fields the gap is suppressed, and a Bose-Einstein condensation (BEC) of magnetic S=1 excitations (called triplons or magnons) is supposed to occur, leading to a magnetic phase with anti-ferromagnetic long-range order of the transverse spin components.

Meanwhile a considerable number of other materials have been found that exhibit various features which can be explained within the same framework (14; 15; 16). The main target we have been pursuing during the last year was to demonstrate the existence of state with macroscopic phase coherence in this compound.

The idea of BEC has already been used quite successfully to explain the transition of "normal" to "superfluid" $^4\mathrm{He}$. The strong interactions that exist in liquid $^4\mathrm{He}$ may alter the nature of the transition, however. For instance, while 90-95% of the particles of an atomic ensemble are in the "superfluid" phase below the transition temperature of an atomic BEC, just a few percent ($\sim$ 9%) of the Helium-atoms are condensed in superfluid $^4\mathrm{He}$.

One of the relevant parameters indicating that a system is Bose-Einstein condensed is the number of particles in the ground state N_c which gets macroscopically large for $T \to 0$K.

In the case of $\mathrm{TlCuCl_3}$ the total magnetization $M = g\mu_B N$ (17) is proportional to the total number of excited triplons N, where g is the Landé g-factor and μ_B is the Bohr magneton. We therefore analyzed this quantity in detail. The temperature dependence of the magnetization $M(T)$ along the applied magnetic field H shows a cusp-like minimum at a finite temperature $T_c(H)$ for fixed magnetic field H (see Fig. 11.6). The increase of M for $T < T_c$ is a consequence of the condensation of the magnetic quasiparticles and the increasing number of particles N_c in the ground state forming the condensate. Theoretical arguments predict a T-dependence of $M \propto \left(1 - \frac{T}{T_c}\right)^{\frac{3}{2}}$ (17).

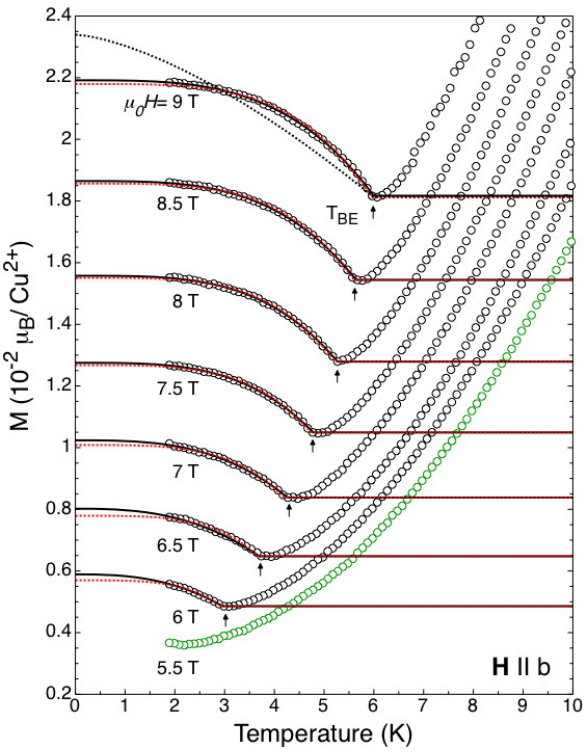

Figure 11.6: The total magnetization M per Cu^{2+} $TlCuCl_3$ for H ∥ b. The low-temperature regime for $T < T_c$ is fitted according to $g\mu_B n(T) = g\mu_B(n_{crit} + n_0(1 - (\frac{T}{T_c})^{\alpha}))$. The dashed red curves are for fixed α=4. The black curves are fits for varying exponent α. The black dotted curve represents a fit for $\alpha = \frac{3}{2}$ at $\mu_0 H$=9T.

We have fitted the low-temperature magnetization according to a more general power law

$$\begin{aligned} m(T) &= \frac{M(T)}{N_d} = g\mu_B \frac{N(T)}{N_d} = g\mu_B n(T) = \\ &= g\mu_B(n_{crit} + n_0\left(1 - \left(\frac{T}{T_c}\right)^{\alpha}\right)) \ , \end{aligned}$$

where N_d is the total number of dimers and $n_{crit} = \frac{N(T=T_c)}{N_d}$ is the critical density at which condensation occurs. This value corresponds to the normalized magnetization $m(T = T_c) = g\mu_B n_{crit}$. At zero temperature we obtain

$m(0) = g\mu_B n(0) = g\mu_B(n_{crit} + n_0)$ and therefore $n(0) = n_{crit} + n_0$. For an ideal Bose gas $n(0)$ corresponds to the condensate density. As soon as interactions between the particles are considered the depletion of the condensate has to be taken into account. The quantity $n(0) = n_c(0) + \tilde{n}(0)$ is then a sum of the condensate density $n_c(0)$ and the density of non-condensed particles $\tilde{n}(0)$. The latter term represents the number of triplons per Cu^{2+}-dimer scattered out of the ground state due the interactions between the particles. It depends on the number of condensed particles and can be expressed as $\tilde{n}(0) = \frac{1}{3\pi^2}\left(\frac{mUn_c(0)}{\hbar^2}\right)^{\frac{3}{2}}$, where $m \approx 2.8 \times 10^{-29}$ kg is the effective mass of a triplon and $\frac{U}{k_B} \approx 315\mathrm{K}$ (18) is the two-particle interaction potential . Extracting $n(0)$ from our fits, we can therefore calculate the condensate density at zero temperature $n_c(0)$ for various magnetic fields (see Fig. 11.7). As one would naively expect from simple arguments (17; 18) $n_c(0)$ increases with increasing magnetic field. The percentage of the condensed particles with respect to the total number of triplons is approximately 96% and slightly decreases with increasing magnetic field.

From this high percentage of condensed particles we conclude that the triplons in $\mathrm{TlCuCl_3}$ form a *weakly interacting Bose gas* right above H_c, and that the interaction increases with increasing particle density (i.e. with increasing the magnetic field H).

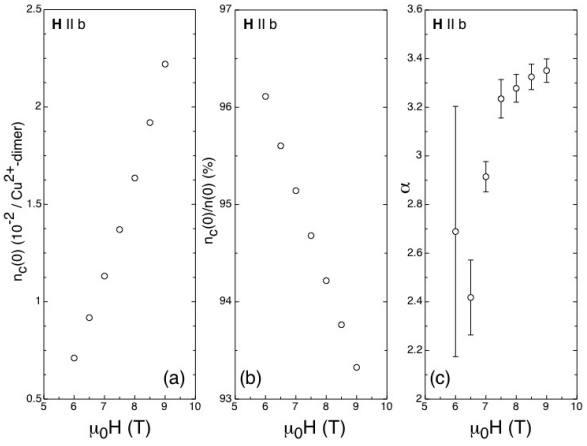

Figure 11.7:
(a) The number of condensed triplons per Cu^{2+} of $TlCuCl_3$ at T=0 K for H ‖ b.
(b) The percentage of particles in the condensate at T=0 K for H ‖ b.
(c) The extracted exponent α from $M(T < T_c)$ data of $TlCuCl_3$ for H ‖ b.

[1] H. Bartolf, *et al.*, accepted for publ. in Phys. C.

[2] A. Engel, *et al.*, submitted to J. Mod. Opt.

[3] C. P. Bean and J. D. Livingston, Phys. Rev. Lett., **12**, 14 (1964).

[4] A. Schilling and O. Jeandupeux; Phys. Rev. B; 52, 9714 (1995).

[5] A. Schilling and M. Reibelt; Rev. Sci. Instrum.; 78, 033904 (2007).

[6] K. A. Moler et al.; Phys. Rev. Lett.; 73, 2744 (1994).

[7] D. A. Wright et al.; Phys. Rev. Lett.; 82, 1550 (1999).

[8] G. E. Volovik; JETP Lett.; 58, 469 (1993).

[9] A. P. Ramirez et al.; Phys. Rev. Lett.; 74, 1218 (1995).

[10] C. Caroli and J. Matricon; Phys. Kondens. Mater.; 3, 380 (1965).

[11] A. P. Ramirez; Physics Letters A; 211, 59 (1996).

[12] M. Nohara et al.; Journal of the Physical Society of Japan; 66, 1888 (1997).

[13] G. M. Schmiedeshoff et al.; Phys. Rev. B; 63, 134519 (2001).

[14] B. Grenier et al., Phys. Rev. Lett. **92**, 087203 (2004).

[15] V. S. Zapf et al., Phys. Rev. Lett. **96**, 077204 (2006).

[16] M. Jaime et al., Phys. Rev. Lett. **93**, 077204 (2004).

[17] T. Nikuni et al., Phys.Rev. Lett. **84**, 5868 (2000).

[18] F. Yamada et al., condmat **arXiv:0711.2110v1** (2007).

12 Surface Physics

T. Greber, M. Hengsberger, S. Berner, C. Galli Marxer, J. H. Dil, H. Yanagisawa, M. Morscher, T. Brugger, F. Meier, D. Leuenberger, A. Devizis, T. Mattle, S. Roth, J. Schmidlin, M. Klöckner, J. Osterwalder

In the surface physics group model systems of well defined surfaces and interfaces are systematically studied in order to address fundamental issues that are relevant for nanoscience and nanotechnology. Our laboratory is well equipped for the preparation and characterization of clean surfaces, metal and molecular monolayer films, as well as self-assembling nanostructures, all under ultrahigh vacuum (UHV) conditions. Experimental techniques available to us include x-ray photoelectron spectroscopy (XPS) and diffraction (XPD), angle-resolved photoemission spectroscopy (ARPES), two-photon photoemission (2PPE) using femtosecond laser pulses, low-energy electron diffraction (LEED) and scanning tunneling microscopy (STM). During this past year, a new variable-temperature STM could be purchased, partly funded by the R'Equip program of the Swiss National Science Foundation (SNF). A new UHV system was designed and built, and the instrument was successfully commissioned. At the nearby Swiss Light Source (SLS) we operate two more photoemission spectrometers, one for spin-resolved Fermi surface mapping and one for photo-electron diffraction and holography. A growing network of national and international collaborations expands this set of experimental techniques and provides us also with the necessary theoretical support.

The research carried out during the report period can be grouped into four topics:

- **Monolayer films of hexagonal boron nitride on metal surfaces**
  The boron nitride nanomesh continued to be one of our major research interests, funded in part by the SNF and the EU (FP6-STREP "NanoMesh"). This one atom thick layer of boron nitride on Rh(111) surfaces, which was discovered some years ago in our group (1), exhibits a very regular hexagonal corrugation pattern with 2 nm wide depressions ("holes") and a periodicity of 3.2 nm, giving the surface a mesh-like appearance in STM images. Its periodicity and atomic structure are now fairly well understood (2; 3; 4), a further structural refinement by means of surface x-ray diffraction (SXRD) is currently ongoing in collaboration with the SXRD group of the SLS. After establishing the ability of the nanomesh to trap naphthalocyanine molecules within the holes, thus forming self-assembled molecular arrays covering macroscopic surface areas (4), we could now contribute to the understanding of the trapping mechanism that keeps the molecules in place (see Sec. 12.1 and Ref. (5)). These studies were extended to other molecules, like copper phthalocyanine and more recently Co carbonyls, the latter with a view of producing Co metal nanoclusters within the nanomesh holes. Preliminary results indicate that Co atoms remain on the surface and form clusters, while the carbonyl groups desorb when the warm nanomesh surface is exposed to a flux of molecules. One of the most remarkable properties of the nanomesh is its robustness when exposed to air and even when immersed in water (6). Within a Master thesis project (T. Mattle), the stability range under electrochemical conditions has been further characterized at EMPA Thun, and preliminary studies of molecular adsorption from the liquid phase are ongoing.

- **Ultrafast processes at surfaces**
  From the laser laboratory, which is located adjacent to the lab housing the photoelectron spectrometer, femtosecond laser pulses can be coupled through a hole in the wall into the photoemission chamber. With this setup, 2PPE experiments can be performed, exploiting also the angular degrees of freedom of the UHV sample goniometer. This has been demonstrated in a recent publication on photoemission momentum mapping and wave function analysis of surface and bulk states on Cu surfaces (7). In a recent Master project (D. Leuenberger), the poorly understood *ultrafast demagnetization* of a Ni surface by fs-laser pulses, previously observed by other groups in optical (8) and photoemission (9) experiments, had been addressed in a new approach. The clean Ni(111) surface is protected by a single boron nitride monolayer, providing at the same time a strongly resonant emission peak in 2PPE spectra (10). In principle, this resonance should be sensitive to changes in the Ni band structure associated with the demagnetization process. The experiments have so far produced ambiguous results and the study has been expanded into a PhD project. In a new Master project (S. Roth), we have started an investigation of diamondoid (nano-clusters of diamond) covered Ag surfaces in view of their interesting property of *negative electron affinity* (NEA) (11). Such surfaces have their lowest unoccupied molecular orbital situated above the vacuum energy and show therefore strongly enhanced electron emission upon photo-excitation. Specifically, self-assembled monolayers of thiolated tetramantane molecules that were obtained through a collaboration with Chevron U.S.A. Inc., Richmond CA, were prepared on Ag(111) and are currently being studied by time-resolved 2PPE. In parallel, the group is commissioning a new photoemission spectrometer in the laser lab. This instrument has been moved from PSI to Zürich (courtesy Ch. Quitmann). It contains an ellipsoidal display analyzer (12) and will allow to measure 2PPE momentum distributions very efficiently.

- **Spin-resolved photoemission and momentum mapping**
  After a couple of very difficult years of identifying, characterizing and fixing magnetic shielding problems, our spin-resolved photoemission chamber at the SLS (COPHEE, the complete photoemission experiment) is now working very well. As a first demonstration, the spin polarization and the spin structure of the electronic states in the two surface alloys Bi/Ag(111) and Pb/Ag(111) have been successfully measured (see Sec. 12.2), and a paper has been accepted for publication in Physical Review B. The unique capability of the instrument to resolve all components of the spin polarization vector of the photoelectrons made it possible to introduce a new two-step fitting routine that provides absolute spin polarization vectors for each individual band intersected in a particular measurement. This procedure is crucial when investigating this type of two-dimensional systems where spin-orbit effects lead to complex momentum dependent spin structures (13; 14). With the photoelectron spin as an additional tag in the measurement, spin-split bands with splittings far below the measured line width can be resolved. This has allowed us to see such splittings in quantum well states within ultrathin Pb layers on Si(111). Comparable to surface states, the space inversion symmetry is broken in these films, and the spin degeneracy of the valence electrons is lifted. The effect is much smaller, though, and first results have shown a splitting of only 15 meV in such films.

- **Further instrumental developments**
  The importance of the electron spin in chemical bonding is obvious (Pauli princi-

ple). For molecules adsorbed on ferromagnetic surfaces, where the absolute spin orientation in spin-split bands can be interchanged by controlling the macroscopic sample magnetization direction, the spin-dependent coupling of molecular orbitals to states of the underlying substrate can be studied. In order to exploit the versatile preparation and characterization environment of our photoelectron spectrometer chamber, we have engaged in a development project for a simplified type of spin detector that is compatible with the existing hemispherical electron analyzer. In this new type of Mott detector, backscattered high-energy electrons are measured within scintillator crystals. The light pulses are extracted by glass rods out of the UHV. This design avoids the complex high-voltage operation of the preamplifiers. A first prototype of the device has been built and will soon be ready for testing.

In conjunction with the nanomesh project, the interest arises whether individual molecules trapped within nanomesh pores can be addressed via optical fluorescence. In order to have a substantial fluorescence yield, excited molecular states have to be long lived, which is not obvious for molecules adsorbed on a metal surface, where many de-excitation channels exist. It is therefore crucial to establish whether the presence of the single-layer boron nitride dielectric provides sufficient decoupling from the underlying Rh surface. Within a Master project (J. Schmidlin), our room temperature STM has been equipped with a detector for recording fluorescence photons excited locally by the tunneling current from the tip. Preliminary measurements show clear photon signals correlating with the tunneling voltage.

In the following, two highlights of last year's research are presented in more detail.

12.1 Boron nitride nanomesh: trapping molecules with dipole rings

In collaboration with: Peter Blaha and Robert Laskowski, Institut für Materialchemie, Technische Universität Wien, A-1060 Vienna, Austria.

The control of the mobility of single atoms or molecules on surfaces is of key importance in nanotechnology. For efficient immobilization or trapping, the bonding has to compromise between bonding strength and deterioration of the specific function of a single molecule, which relies on a minimal coupling to the degrees of freedom of the support. Surface dipoles, which contribute strongly to the bonding of polarizable entities, should lead to lateral immobilization as soon as they also exhibit in-plane components. In this respect, a ring geometry of in-plane dipoles appears most attractive for complete confinement of molecules within a nanometer-size space. The mesh-like monolayer structure of hexagonal boron nitride on Rh(111) (1) represents a perfect realization of a dense layer of such dipole rings with diameters of 2 nm. This is demonstrated by the adsorption of highly polarizable Xe atoms, and by using photoemission from shallow Xe core levels as a sensitive probe for the electrostatic energy landscape on this layer.

It is now established that the h-BN nanomesh on Rh(111) or Ru(0001) is a single sheet of hexagonal boron nitride, where 13x13 BN units form a coincidence lattice with 12x12 substrate unit cells (2; 3; 4; 15). Two distinct BN regions were found within the sp^2-bonded network of h-BN: A closely bound region assigned to the "holes" in the nanomesh and a loosely bound region assigned to the "wires" (see Fig. 12.1) (3; 4; 15). Theory confirmed the experimentally observed electronic structure and showed the sp^2 derived BN σ-band density of states of the holes and the wires to be quasi rigidly shifted with respect to each other by about 1 eV (3). This suggests that a signi ficant

portion of the h-BN σ-band shift is related to electrostatics, i.e. to different work functions of the wires and the holes. The accompanying local vacuum level misalignment imposes electric fields and leads to lateral polarization within the h-BN sheet. This is described with dipole rings, which in turn offer a natural explanation for an enhanced immobilization of molecules. Fig.12.2 shows valence band photoemission data from Xe on h-BN/Rh(111) for different Xe coverages. It is seen that the Xe atoms first occupy sites in the holes and then start to cover wire- and further hole-sites within the nanomesh unit cell. The Xe 5p binding energy difference of 0.3 eV between Xe in the holes and Xe on the wires corresponds to the difference of the electrostatic potential at the sites of the Xe cores, 2Åabove the surface. This is rationalized by in plane dipoles on rings located at the rims of the holes. The potential energy landscape, where the holes attract electrons, is confirmed by density functional theory calculations within a super-cell with more than thousand atoms.

Thermal desorption spectroscopy allows to determine the site specific Xe desorption energies. It is found that 12 Xe atoms in the nanomesh unit cell that were located in the holes, have a desorption energy which is 25 meV larger than that of the 42 other Xe atoms in the nanomesh unit cell with a full monolayer (182±0.05 meV). We expect dipole rings also to occur in other dislocation networks and that this concept will improve the understanding of two-dimensional templates for supramolecular structures.

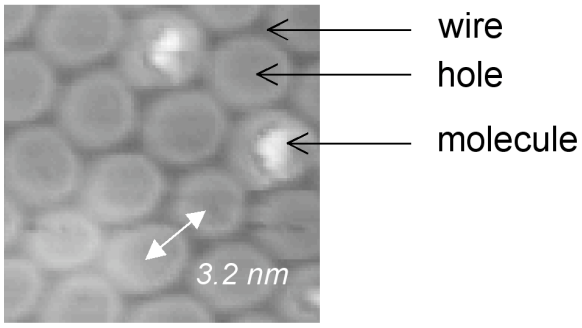

Figure 12.1: Scanning tunneling microscopy image of h-BN/Rh(111). About 20 unit cells with a lattice constant of 3.2 nm are shown. The two distinct regions of the wires (dark) and the holes (bright) are marked. Two holes are occupied by Cu-phthalocyanine molecules.

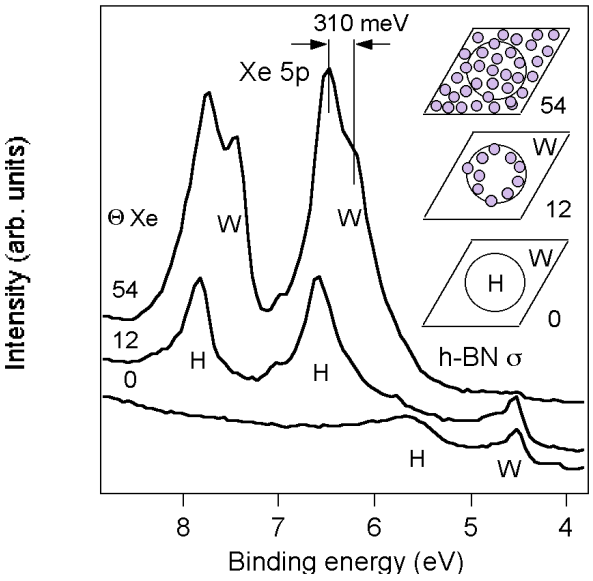

Figure 12.2: Photoemission spectra ($\hbar\omega$=21.2 eV) for three different Xe coverages on h-BN nanomesh. Θ Xe is the number of Xe atoms per unit cell. H stands for hole, W for wire. When Xe is in the holes the H-σ-bands are suppressed. The three icons mimic the nanomesh unit cell and the location of the Xe atoms. The Xe 5p doublet is also split in a H and a W contribution. The energy difference of 310 meV corresponds to the electrostatic potential-energy difference between the Xe cores on top of the wires and the holes.

12.2 Understanding and tuning the electron spin at surfaces

In collaboration with:
Luc Patthey, Swiss Light Source, Paul Scherrer Insititute, 5232 Villigen, Switzerland.

Methods that allow to control and measure the electron spin, or the average of a certain quantity of spins, have received growing attention in the last few years. In spintronics, the spin field-effect transistor as proposed by Datta and Das (16), which relies on the Rashba-Bychkov effect (17) (henceforth Rashba effect), is one of the key elements. The basis of the Rashba effect lies in the breaking of the crystal symmetry at the surface and the resulting absence of space inversion symmetry. For a parabolic band this will produce two parabola that are split in momentum and cross at the centre of the Surface Brillouin zone. The size of this splitting is determined by the magnitude of the potential gradient at the surface and the atomic number Z of the atoms involved. In order to utilize the Rashba effect the splitting of the two bands has to be large compared to the other energy scales in the system. Recently, a very large band splitting was reported in the two surface alloys Bi/Ag(111)$\sqrt{3} \times \sqrt{3}$ ($R30°$) and Pb/Ag(111)$\sqrt{3} \times \sqrt{3}$ ($R30°$) (18; 19), henceforth referred to as Bi/Ag(111) and Pb/Ag(111). The spin integrated band structure can roughly be explained by a Rashba type spin-orbit splitting of the Bi (or Pb) induced surface states. In these systems the Rashba effect is strongly enhanced due to an additional reduction of the surface symmetry caused by the $\sqrt{3} \times \sqrt{3}$ ($R30°$) surface reconstruction and due to the corrugation of the surface (20). Furthermore it has been proposed that the symmetry of the individual bands plays a crucial role in the Rashba effect.

Spin and angle resolved photoemission spectroscopy (SARPES) data were obtained for the Bi/Ag(111) and Pb/Ag(111) surface alloys using the COPHEE spectrometer located at the surface and interface spectroscopy beamline at the Swiss light source (21). This spectrometer is capable of measuring the spin polarization along three orthogonal directions in real space for any point in reciprocal space (22). This means that all the quantum numbers of a photoemitted electron can be obtained. In order to harness the amount of information obtained in this manner a novel two step fitting routine has been developed. Using this routine the magnitude and orientation of the spin polarization vector in three dimensional space can be obtained for individual bands. The usefulness and necessity of this approach is illustrated in Fig. 12.3. Due to their large number of bands and complex band structure these surface alloys provide ideal test cases. An additional benefit of this procedure is that bands which can normally not be resolved in spin integrated photoemission are easily separated using the spin as an additional tag of individual bands. Our data confirm that the orientation of the spin polarization vector depends on both the orientation of the potential gradient and the orbital symmetry of a state. This information is typically not accessible in spin integrated ARPES and can be used to verify ab-initio density functional theory calculations. Although the measured spin polarization is usually less than one due to overlapping bands and an unpolarized background, our analysis shows that the true polarization of individual bands is either zero or one. This finding sheds a new light on previous publications in the field, both theoretical and experimental. In order to standardize the results of spin resolved measurements and theoretical treatments, we suggest to focus on the direction of the spin polarization vector rather than the relative magnitude of the polarization along a coordinate system, especially for non magnetic samples. Building on the understanding of the electron spin behaviour at surfaces obtained from these experiments we can now explore some possibilities to tune electron spins in artificial systems prepared by standard surface science procedures.

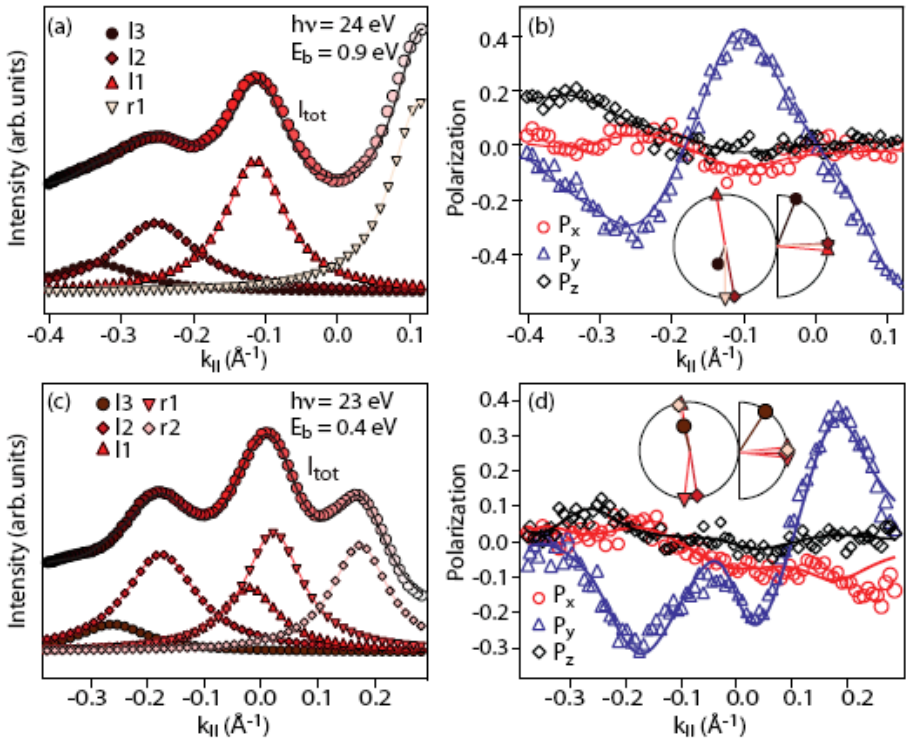

Figure 12.3:
Photoemission momentum distribution curves measured on Bi/Ag(111) at a binding energy E_B = 0.9 eV with $\hbar\omega$ = 24 eV (top panels) and at E_B = 0.4 eV with $\hbar\omega$ = 23 eV (bottom panels) along the $\overline{\Gamma K}$ direction of the surface Brillouin zone (from Ref. [21]).
(a) and (c):
spin integrated intensities and the Lorentzian peaks of the fit. The solid line is the total intensity fit.
(b) and (d):
measured (symbols) and fitted (solid lines) spin polarization curves from the MDC. The statistical errors are smaller than the symbol size. The insets visualize the in-plane and out-of-plane spin polarization components obtained from the polarization fit, where the symbols refer to those in (a) and (c).

[1] M. Corso, et al., Science 303, 217 (2003).
[2] O. Bunk et al., Surf. Sci. 601, L7 (2007).
[3] R. Laskowski et al., Phys. Rev. Lett, 98, 106802 (2007).
[4] S. Berner et al. Angewandte Chemie Int. Ed. 46, 5115 (2007).
[5] J. H. Dil et al., Science 319, 1824-1826 (2008).
[6] R. Widmer et al., Electrochemistry Commun. 9, 2484 (2007).
[7] M. Hengsberger et al., Phys. Rev. B 77, 085425 (2008).
[8] E. Beaurepaire et al., Phys. Rev. Lett. 76, 4250 (1996).
[9] H. S. Rhie et al., Phys. Rev. Lett. 90, 247201 (2003).
[10] M. Muntwiler et al., Phys. Rev. B 75, 075407 (2007).
[11] W. L. Yang et al., Science 316, 1460 (2007).
[12] T. Dütemeyer et al., Rev. Sci. Instrum. 72, 2638 (2001).
[13] S. LaShell et al., Phys. Rev. Lett. 77, 3419 (1996).
[14] M. Hoesch et al., Phys. Rev. B 69, 241401 (2004).
[15] A. Goriachko et al. Langmuir, 23, 2928 (2007).
[16] S. Datta and B. Das, Appl. Phys. Lett. 56, 665 (1990).
[17] Y.A. Bychkov and E.I. Rashba, JETP Lett. 39, 78 (1984).
[18] C. R. Ast et al., Phys. Rev. Lett. 98, 186807 (2007).
[19] D. Pacile et al., Phys. Rev. B 73, 245429 (2006).
[20] G. Bihlmayer et al., Phys. Rev. B 75, 195414 (2007).
[21] F. Meier et al., Phys. Rev. B (in press); cond. mat. arXiv:0802.1125.
[22] M. Hoesch et al., J. Electron Spectrosc. Relat. Phenom. 124, 263 (2002).

13 Physics of Biological Systems

C. Andreoli (until October 2007), C. Escher, H.-W. Fink, M. Germann (since September 2007), Tatiana Latychevskaia, J.-N. Longchamp (since October 2007), Elvira Steinwand.

in collaboration with:
Eugen Ermantraut, Clondiag Chip Technologies (Germany); Dr. Pierre Sudraud, Orsay Physics (France); Prof. John Miao, University of California at Los Angeles (USA); Prof. Dieter Pohl, University of Basel; Prof. Andre Geim, Manchester Centre for Mesoscience and Nanotechnology, University of Manchester, Dr. Ilona Müllerová, Institute of Scientific Instruments (Czech Republic), Dr. Heinz Gross, ETH Zurich, Dr. Petr Formanek, University of Dresden (Germany).

In connection with the structural investigation of biological objects by Low Energy Electron Point Source (LEEPS) microscopy we established a sample preparation technique based on DNA. The molecules are stretched over holes in a structured thin film by a laminar flow followed by rapid quenching in under-cooled liquid nitrogen to embed DNA in amorphous ice. The final step, before transfer to the LEEPS microscope, is the freeze drying at low temperature in vacuum. The DNA molecule serves us as a template for presenting proteins to the coherent electron wave. DNA modifications for attaching proteins are designed by Clondiag Chip Technologies in Jena.

Free standing graphene membranes shall serve as transparent support for holography with low energy electrons in connection with the EU project SIBMAR. We are newly assisted in this endeavour by a group in Brno. They carry out Scanning Low Energy Electron Microscopy (SLEEM) studies on free-standing graphene membranes. A second approach towards structural biology on a single molecule level is based on phase retrieval from an over sampled coherent electron diffraction pattern of a single molecule. The instrument for that is now operational and preliminary data show that it is possible to generate a coherent parallel beam by employing a micro-structured electron lens. Some recent achievements towards our goal to obtain structural information from a single molecule are illustrated in some detail below.

13.1 Numerical hologram reconstruction

The recent solution of the long standing twin image problem in holography (1) has meanwhile also been applied to the reconstruction of holograms taken with 200 keV electrons in the holography laboratory of the University of Dresden. It turns out that the twin image removal technique leads to reconstructed in-line holograms comparable to those from off-axis holography where the object and reference wave are propagating in different direction. For low energy electrons, however, their strong forward scattering still needs to be build into the reconstruction routine.

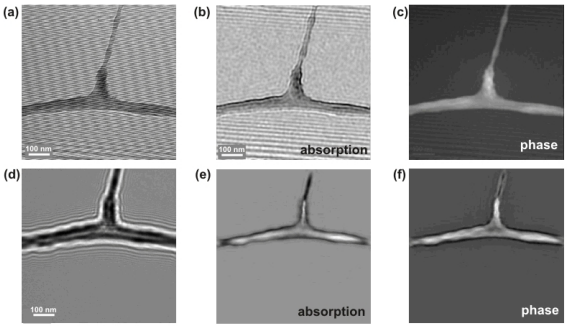

Figure 13.1: (a) High-energy electron off-axis hologram of a carbon net taken taken in the Holography laboratory at the University of Dresden. (b) and (c) Absorption and phase reconstructed from the off-axis hologram. (d) High-energy electron in-line hologram of a carbon net. (e) and (f) Absorption and phase reconstructed from the in-line hologram.

13.2 Pulsed holography with low energy electrons

Restrictions to the resolution in low-energy electron holograms are associated with residual vibrations and ac magnetic fields. Both limit the coherence of the beam and with this the interference resolution in the holograms. In order to circumvent these resolution limiting factors we now do acquire holograms in a pulsed mode. The pulse duration times have to be well below typical vibration periods and ac-magnetic field changes. However, short exposure times lead to holograms with a poor signal to noise ratio. This problem has been overcome by acquiring a large set of pulsed holograms of the same molecule and using cross-correlation to account and correct for the shift between subsequently taken holographic records of the same molecule.

Initial experiments show that this strategy of pulsed holography works and leads to improved interference resolution as evident from Fig. 13.2. The set of superimposed holograms of a DNA molecule shows the disturbing effect of vibrations which smear out high order interference fringes. If cross correlation is employed to align subsequently taken holograms, a significantly improved signal to noise ratio and visibility of high order fringes, already evident by visual inspection, is apparent.

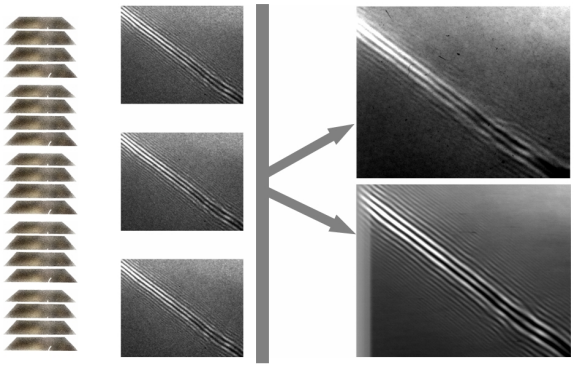

Figure 13.2: A set of 400 electron holograms has been taken in the pulsed mode at 140 eV kinetic energy of the electrons. The MCP was held at a dc bias of 670 V and a pulse of 500V was applied to the MCP to increase the gain for 50 microsecond duration. Three out of 400 noisy data sets are shown. At the top right, the superposition of all 400 records is shown, at the bottom right, the superposition after cross- correlation alignment is displayed.

Apart from improvements in the detector system, our major strategy for improving interference resolution relies now on pulsed holography. While the first data seem promising, improving the short time electronics is a major challenge. In order to avoid unnecessary exposure of the molecule during the time in between pulses, it will be necessary to also pulse the electron source with a precision of a few 10 mV in order to not sacrifice temporal coherence.

13.3 Radiation damage by low energy electrons

Radiation damage is one of the major obstacles in using radiation with sufficiently short wave length, like x-rays or energetic electrons, for structural determination of single molecules. In x-ray diffraction, only every thousandth photon is scattered elastically and carries information about the molecules structure; all the rest just causes damage to the fragile object. For low energy electrons it is so far only qualitatively known that the amount of damage is much less. We have started a detailed study on determining the extent of radiation damage and contrast transfer by low-energy electrons in the range between 10 and 500 eV. The permissible dose will ultimately determine the signal-to-noise ratio for the high-resolution terms incorporated in the holographic reconstruction and will allow optimal set-up of imaging conditions in LEEPS microcopy. We hope to discover energy windows in which essentially no damage to proteins occurs. This would then make low energy electrons the only known

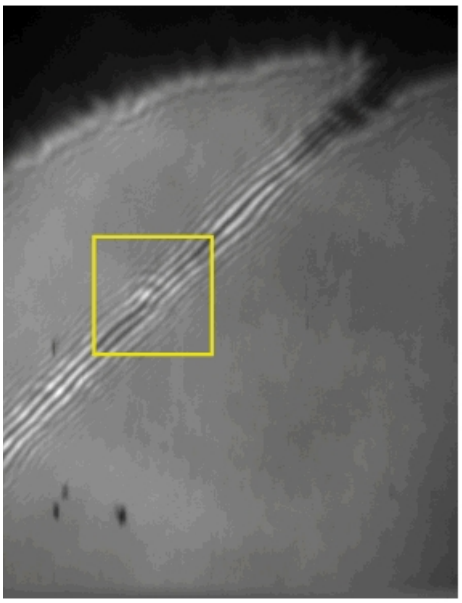

Figure 13.3: Electron hologram of a DNA. Marked in yellow is the area that is used for computing the cross-correlation between subsequent hologram.

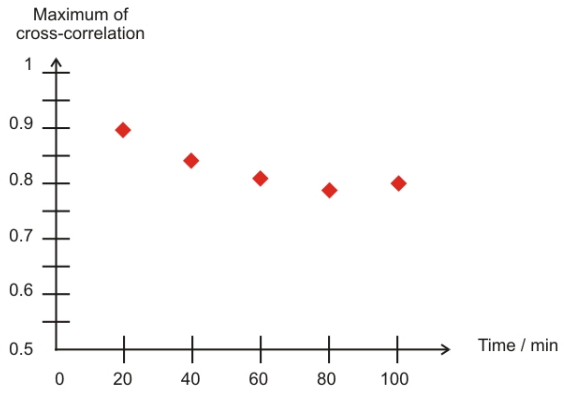

Figure 13.4: Maximum of the cross-correlation between the first hologram and the later recorded holograms as a function of time.

radiation with potential atomic resolution not plagued by radiation damage. A first indication that such windows might indeed exist is displayed in Figs. 13.3 and 13.4. A DNA molecule has continuously been imaged for 100 minutes with coherent electrons of 107 eV. The total emission current of 100 nA corresponds to an estimated dose of 108 electrons/nm^2. Despite this massive dose the hologram of the molecule has not altered significantly as evident from the cross correlation coefficient between subsequent images which maintains a high value throughout the 100 minutes of observation.

[1] T. Latychevskaia and H.-W. Fink, Phys. Rev. Lett. 98, 233901 (2007).

14 Mechanical Workshop

K. Bösiger, B. Lussi, R. Maier, M. Schaffner, S. Scherr, O. Fardin (apprentice), T. Naterop (apprentice since August 2007) and R. Reichen (until October 2007)

Thanks to the availability of sophisticated numerically controlled machines the mechanical workshop is well equipped to manufacture all kind of complicated and technically demanding components. For this reason the number of orders from other departments of the university is increasing steadily. The income from construction and modification work for outside companies is used for new tooling and for advanced training courses of the apprentices and the staff members. We also design and build prototypes and make limited-lot productions.

More than 30 institutes made again use of the metal and technical material store maintained by the workshop [7]. The store not only supplies materials but quite often also consults its customers.

During the reporting period some smaller investments were made. For the welding shop we purchased a dedicated welding machine used exclusively for the metal active gas (MAG) and the metal inert gas (MIG) welding of aluminum. On the modern milling machine DMU 50ev we installed a haze filter system. A 26 years old universal manually controlled milling machine was completely refurbished. In the metal and technical material store we adapted the storage frames for the sheet material to the larger actual norm dimensions and the storage for the remainder parts was rearranged.

In summer 2007 and winter 2008 we organized and accomplished the basic courses for the bachelor students in physics. In a first stage the candidates learn how to use all kinds of measuring tools and how to read and produce technical drawings. They also accomplish simple work on drilling and milling machines as well as on the lathe. The course finishes with an introduction in the technique of hard soldering. In the second stage more demanding machining techniques are trained. Different materials are handled and an introduction into various welding processes is given. Because of the large number of participants we had to arrange four courses of 35 hours each.

Below we list some of our main projects and activities during 2007.

CMS pixel detector

In 2007 the main part of the workshop workload was related to this project. We produced the detector support structure for the prototype system consisting of a complete half shell and the two half shell pairs needed for the final system. To guarantee the required precision a lot of auxiliary tooling had to be produced for the construction of these parts. Here we profited strongly from the modern computer controlled milling machine with 5 axes (DMU 50eV) acquired in 2005. Very complex parts could be produced with high precision. At the end of October 2007 the final system was sent to PSI, where the installation of the silicon sensors started.

Besides the detector support structure we also manufactured the supply tube half shells for the barrel pixel detector of the CMS experiment. The experience made with the prototype half shell pair resulted in some changes for the final two half shell pairs. Additional

[1] For a catalogue see http://www.physik.unizh.ch/groups/werkstatt/dienstleistung.html

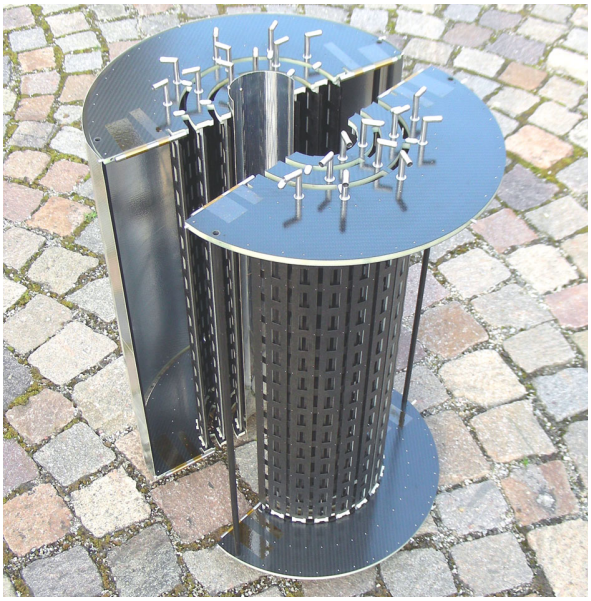

Figure 14.1: CMS Barrel Pixel Support Structure.

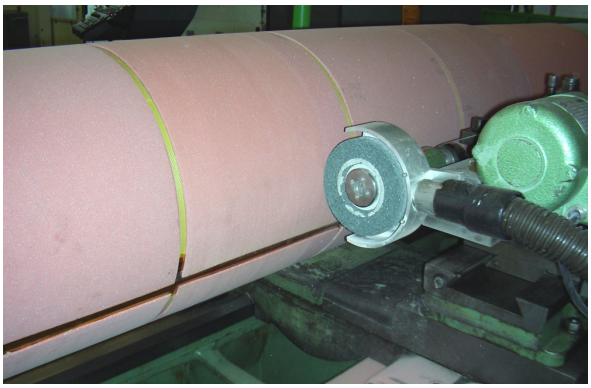

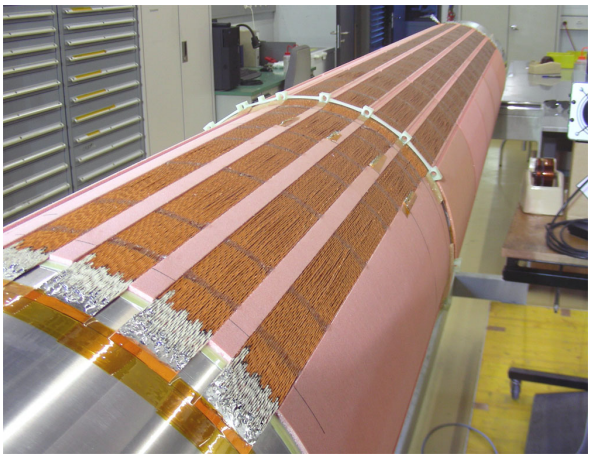

Figure 14.2: CMS Barrel Pixel Supply Tube during the production.

auxiliary tools were produced in the workshop. The production of these parts with a length of about 2.2 m was accomplished on a 3 m long lathe which is especially adapted for such components. Although the experts from the safety department of the university complained about the unconventional use of the machine it was only due to these additional installations and modifications that the very complex milling, drilling and grinding work could actually be accomplished. The last supply tube pair was completed in April 2008. All components are now at PSI where the complete detector system will be assembled.

LHCb silicon tracking detector

The Tracker Turicensis was transported to CERN already at the end of 2006. Some modifications were made to the cooling system and the electronic crates.

Figure 14.3: Installation of the LHCb TT-station at CERN.

Surface Physics

We manufactured a stand for a scanning tunneling microscope (STM) with different extensions and installations. We produced different probe- and vacuum-deposition-holders made out of stainless steel. In addition we performed maintenance and repair work during the whole reporting period.

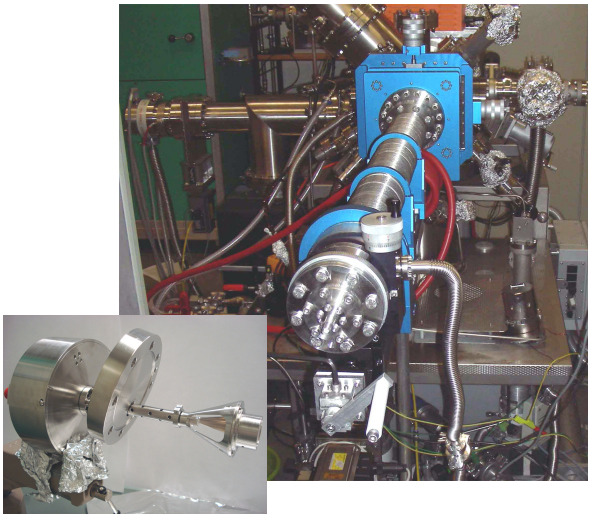

Figure 14.4: Vacuum parts made out of stainless steel and a new probe manipulator.

XENON Experiment

We produced a test setup for photomultipliers and manufactured different parts made out of Teflon for the XENON experiment built up at the Gran Sasso laboratory in Italy.

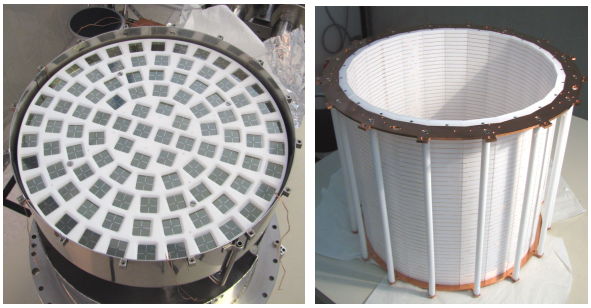

Figure 14.5: Components for the XENON Experiment made out of Teflon.

Solid State Physics

Specimen holders and complete probe manipulators were produced. We manufactured different coil shells and probe packagings made out of different materials.

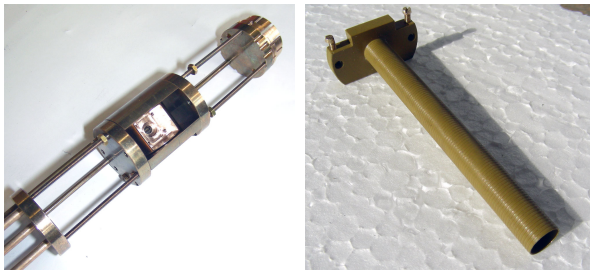

Figure 14.6: Coil shell and specimen holder made out of different materials.

Physics of Biological Systems

Different test setups were built. Some apparatus were upgraded and in addition we performed maintenance and repair work.

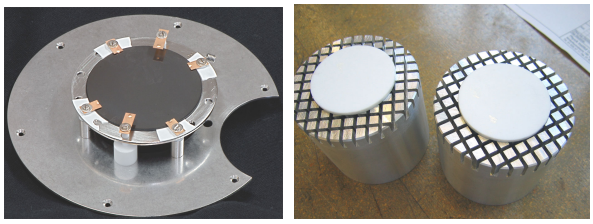

Figure 14.7:
Multichannel plate holder and ceramic disks for the LEEPS Microscope prepared for the milling.

Projects from other institutes and outside companies

In 2007 an increasing number of jobs were carried out on the workshop machinery for other institutes of the university. Besides single parts, complete setups were also built. Furthermore, we accomplished some work for outside companies.

Figure 14.8: Custom built sample holder for the Institute of Physiology.

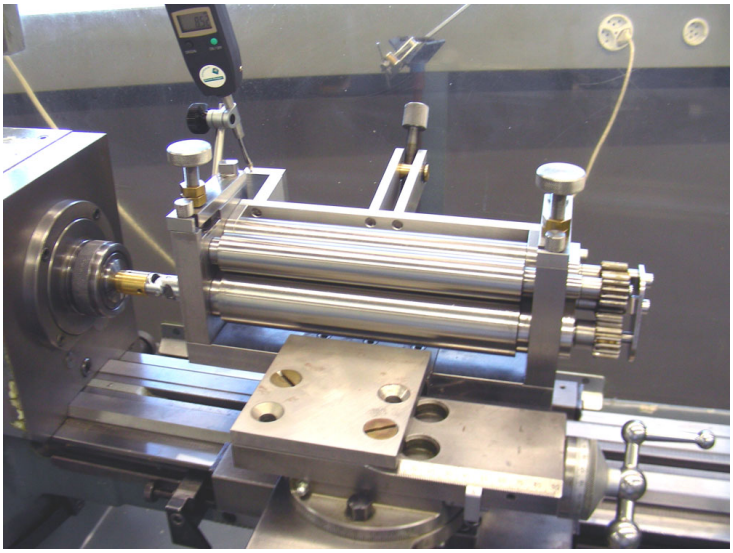

Figure 14.9: Dedicated plate bending machine.

Continuing education of the workshop staff

In April and June 2007 an internal welding course was organized for the workshop staff. For 5 days we learned and practiced the latest welding techniques. Seminars and innovation days in relation with modern processing methods (welding, grinding, milling, etc.) were attended. In August and September training courses for the CAM software used in the workshop were organized for all staff members.

Education of the apprentices

Besides the mandatory Swissmechanic courses the apprentices attended also advanced education in computer controlled machine (CNC) programming, pneumatics and electronics. In May 2007 the apprentices had to pass their intermediate and final exams. The final apprenticeship examination consisted of a project of 75 working hours carried out at the institute's workshop. The candidate had to manufacture a dedicated plate bending machine which was designed and developed in the workshop. With this apparatus we can produce precise tubes with a length of 150 mm and a diameter of 30 mm and greater out of 1.5 mm thick plate material. In the period 11 - 15 June 2007 we organized trial courses for young people interested in an apprenticeship at the workshop.

Miscellaneous

On the 29th and 30th of June 2007 the workshop staff visited CERN in Geneva. We visited both LHCb and CMS for which we manufactured components in our workshop. In October we moved the components of the H1-project which were de-comissioned in 2007 back from Hamburg to Zürich. Since 1991 people from the workshop staff spent several weeks working for the project at DESY. So leaving Hamburg this time some nostalgia came up. In February 2008 the workshop staff enjoyed a day out in the snow.

15 Electronics Workshop

W. Fässler, Hp. Meyer, P. Soland, and A. Vollhardt (since August 07)

A main effort of this year's activities went into the CMS barrel pixel project. The complete electronics for the Supply Tube prototype half shells and the final system was designed, manufactured and assembled. This includes also the Barrel Pixel detector front-end control system with the associated communication and control unit boards (CCU boards) which connect the detector system to the front end controller module. The boards for the complete detector system and additional spares were manufactured and assembled. For the mounting of the ball grid array chips we had the chance to use the dedicated system available at the PSI electronics workshop. The prepared components were then mounted with our help onto the basic Supply Tube structures and all solder connections had to be made accurately (see Fig. 15.1).

Finally the completed systems had to be tested. After installing the electrical and optoelectrical readout components including the optical fibers the entire system was again tested. All components are now at PSI where the assembly of the complete detector system is in the final stage.

We were also involved in the installation and commissioning of the trigger tracker system of the LHCb experiment. In different stages the single detector modules were mounted into the detector housings already installed in the experimental hall at CERN and subsequently electrically tested.

The electronics workshop supported also all research groups in maintaining and repairing the existing devices. We designed and developed some dedicated preamplifiers, mainamplifiers and a push-pull amplifier with an output impedance of 200 Ohm used to drive detection coils. For the XENON experiment a series of existing amplifier modules was supplemented with a USB computer interface allowing the control over each single channel.

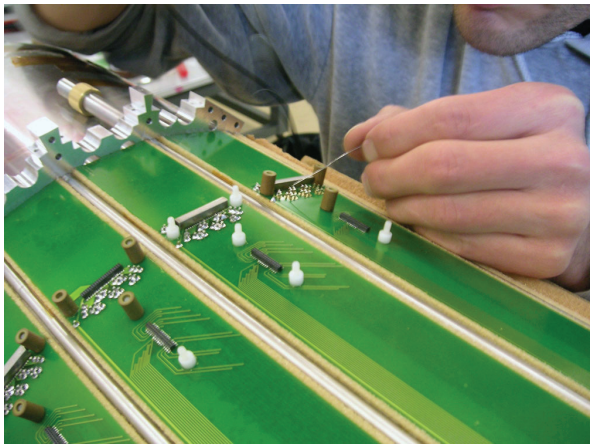

Figure 15.1: Soldering of the copper plated aluminum power wires to the Supply Tube printed circuit boards.

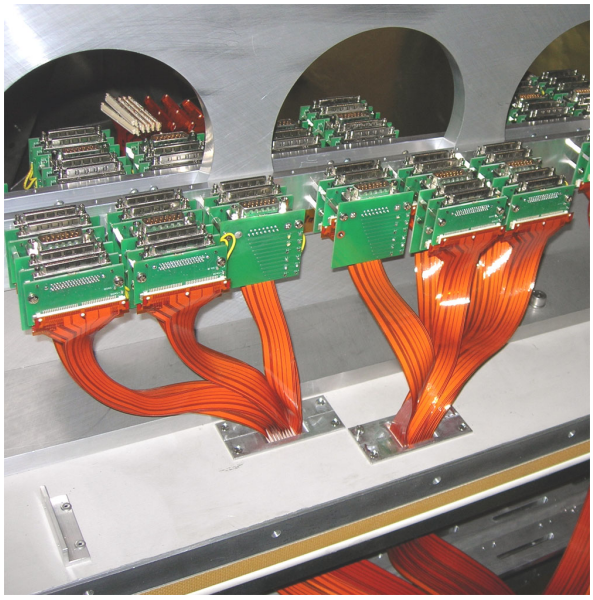

Figure 15.2: Readout electronics of the LHCb trigger tracker detector.

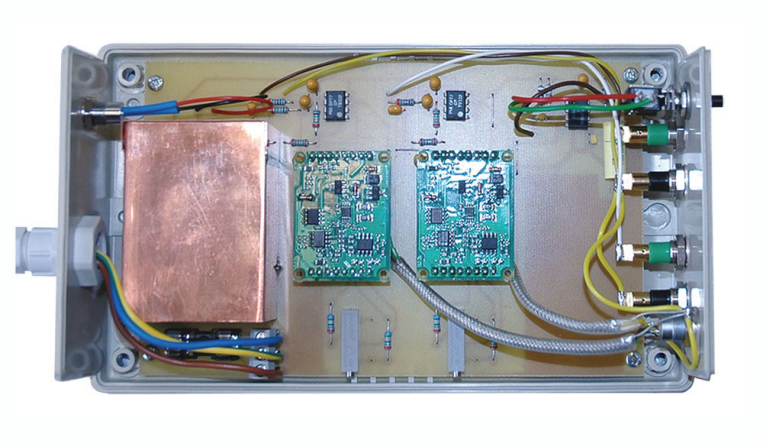

Figure 15.3: Amplifier for the resistance strain gauge experiment.

In collaboration with L. Pauli and J. Seiler, who are responsible for the preparation of the demonstration experiments, we renewed and improved some experiments. Figure 15.3 shows the new amplifier built for the strain gauge demonstration experiment. In most cases we have to improve the output signal quality which we then also match to the computer readout system installed in the lecturer halls used to visualize the measurements. The workshop staff attended seminars and tutorials to remain up-to-date in the fastly-developing field of modern electronics.

16 Publications

16.1 Elementary particles and their interactions

16.1.1 ArDM

Articles

- **Luminescence quenching of the triplet excimer state by air traces in gaseous argon**
  C. Amsler *et al.*, Journal of Instrumentation **3** (2008) P02001.
- **Detection of VUV scintillation light in one ton of liquid argon**
  C. Regenfus, Proc. of the 6th Int. Workshop on the Identication of Dark Matter (IDM2006), Rhodes, World Scientific (2007) 325.

Invited Lectures

- V. Boccone: **Assembly and test of the light readout for the ArDM WIMP-detector**
  Swiss Physical Society, Geneva, 26 March 2008.
- C. Regenfus: **Search for WIMPs with one ton of LAr – the ArDM experiment**
  Seminar zum Graduiertenkolleg – Physik an Hadron-Beschleunigern, Freiburg i.B., 27 June 2007.
- C. Regenfus: **Status of the Argon Dark Matter Experiment**
  CHIPP-Plenary Meeting, PSI, Villigen, 15 October 2007.

16.1.2 ATHENA

Articles

- **Protonium production in ATHENA**
  L. Venturelli *et al.*, Nucl. Instr. Meth. in Phys. Research **B 261** (2007) 40.
- **Production of slow protonium in vacuum**
  N. Zurlo *et al.*, Proc. of the TCP 06 Conf., Hyperfine Int., Springer Verlag, 2007.

16.1.3 CDMS

Talks

- T. Bruch: **New Results from the CDMS-II experiment**
  Contributed Talk, University of Freiburg, March 3, 2008.
- T. Bruch: **Cryogenic Dark Matter Search**
  Seminar, ETH Zürich, September 14, 2007.
- T. Bruch: **Cryogenic Dark Matter Search**
  Seminar, RWTH Aachen, July 9, 2007.
- T. Bruch: **Cryogenic Dark Matter Search experiment status and future: CDMS to SuperCDMS**
  Plenary Talk, Imperial College London, July 5, 2007.

16.1.4 CMS

Articles

- **Design and performance of the silicon sensors for the CMS barrel pixel detector**
  Y. Allkofer *et al.*, Nucl. Instrum. Meth. **A 584** (2008) 25.
- **CMS Technical Design Report, Volume II : Physics Performance**
  J. Phys. G: Nucl. Part. Phys. **34** (2007) 993.
- **Summary of Session 2 : Data Analysis - Algorithms and Tools**
  T. Speer, Proc. of XI Int. Workshop on Advanced Computing and Analysis Techniques in Physics Research, Amsterdam, Proc. of Science, PoS(ACAT) 089 (2007).
- **The ATLAS and CMS detectors and triggers for B-physics**
  T. Speer, Nucl. Phys. Proc. Suppl. **167** (2007) 165.

Articles in press

- **The Compact Muon Solenoid Detector at LHC**
  CMS Collaboration, Journal of Instrumentation (2008).
- **The CMS Tracker Operation and Performance at the Magnet Test and Cosmic Challenge**
  W. Adam *et al.*, Journal of Instrumentation (2008).
- **The CMS pixel detector: from production to commissioning**
  V. Chiochia, Proc. 10th ICATPP Conf. on Astroparticle, Particle, Space Physics, Detectors and Medical Physics Applications, Como, e-Print: arXiv:0710.5120 (physics.ins-det).
- **B physics at CMS**
  T. Speer, Proc. 2007 Eur. Conf. on High Energy Physics, Manchester, Journal of Physics: Conference Series.

Public Notes

- **Lorentz angle calibration for the barrel pixel detector**
  Lotte Wilke, CMS NOTE-2008-012.

- **A new technique for the reconstruction, validation and simulation of hits in the CMS pixel detector**
  M. Swartz *et al.*, CMS NOTE-2007-033.

Invited Lectures

- E. Alagöz: **Position resolution of the pixel detector for the CMS experiment**
  Turkish Physical Society, Malatya, 29 August 2007.

- E. Alagöz: **Testbeam study of the irradiated pixel barrel sensors for the CMS experiment**
  Swiss Physical Society, Geneva, 27 March 2008.

- V. Chiochia: **The CMS pixel detector: from production to commissioning**
  10th ICATPP Conf. on Astroparticle, Particle, Space Physics, Detectors and Medical Physics Applications, Como, 10 October 2007.

- T. Rommerskirchen: **Study of the discovery potential of supersymmetric final states at CMS**
  German Physical Society, Freiburg i.B., 5 March 2008.

- T. Rommerskirchen: **Study of the discovery potential of supersymmetry with final states with missing energy, mutiple jets and b-jets at the CMS detector**
  Swiss Physical Society, Geneva, 27 March 2008.

- A. Schmidt: **b-Quark-Jet Identifikation in CMS**
  German Physical Society, Freiburg i.B., 5 March 2008.

- T. Speer: **Data analysis and reconstruction algorithms**
  XI Int. Workshop on Advanced Computing and Analysis Techniques in Physics Research (ACAT), Amsterdam, 25 April 2007.

- T. Speer: B**-Physics at CMS**
  Institute for High Energy Physics of the Austrian Academy of Sciences, Vienna, Austria, 22 June 2007.

- T. Speer: B**-Physics at CMS**
  2007 Eur. Conf. on High Energy Physics, Manchester, 20 July 2007.

- L. Wilke: **Flavour Physics**
  Plenary CMS invited talk, 21 June 2007.

- L. Wilke: **Lorentz angle calibration for the CMS barrel pixel detector**
  German Physical Society, Freiburg i.B., 6 March 2008.

16.1.5 CRYSTAL BARREL

Article in press

- **Partial wave analysis of $\bar{p}p$ annihilation at rest into $2\pi^+2\pi^-\eta$**
  C. Amsler *et al.*, Eur. J. Phys.

16.1.6 DIRAC

Article

- **A novel aerogel Čerenkov detector for DIRAC-II**
  Y. Allkofer *et al.*, Nucl. Instr. Meth. in Phys. Research $\mathbf{A}$ $\mathbf{582}$ (2007) 497.

Articles in press

- **A new aerogel Cherenkov detector for DIRAC-II**
  Y. Allkofer *et al.*, Nucl. Instrum. Meth. in Phys. Research $\mathbf{A}$ (2008).
- **The C4F10 Cherenkov detector for DIRAC-II**
  S. Horikawa *et al.*, Nucl. Instrum. Meth. in Phys. Research $\mathbf{A}$ (2008).
- **Search for πK-atoms with DIRAC II**
  Y. Allkofer *et al.*, Proc. of XII Int. Conf. on Hadron Spectroscopy (Hadron07), Frascati (2007), Physics Series, Vol. XLVI (2008).

Invited Lectures

- Y. Allkofer: **Search for πK-atoms with DIRAC II**
  XII Int. Conf. on Hadron Spectroscopy (Hadron07), Frascati, 7 October 2007
- Y. Allkofer: **Search for πK-atoms with DIRAC II**
  CHIPP-plenary meeting, PSI, Villigen, 15 October 2007.
- S. Horikawa: **A new aerogel Cherenkov detector design for DIRAC-II**
  6th Int. Workshop on Ring Imaging Cherenkov Counters (RICH2007), Trieste, 18 October 2007.
- S. Horikawa: **The DIRAC C4F10 Cherenkov Detector**
  6th Int. Workshop on Ring Imaging Cherenkov Counters (RICH2007), Trieste, 19 October 2007.

16.1.7 D0

Articles

- **Search for squarks and gluinos in events with jets and missing transverse energy using 2.1 fb-1 of ppbar collision data at $\sqrt{s}$=1.96 TeV**
  V. M. Abazov *et al.*, Phys. Lett. B **660**, 449 (2008).

- **Measurement of the $p\bar{p} \to WZ + X$ cross-section at $\sqrt{s}$ = 1.96-TeV and limits on WWZ trilinear gauge couplings**
  V. M. Abazov *et al.*, Phys. Rev. D **76**, 111104 (2007).

- **Search for the lightest scalar top quark in events with two leptons in $p\bar{p}$ collisions at $\sqrt{s}$ = 1.96-TeV**
  V. M. Abazov *et al.*, Phys. Lett. B **659**, 500 (2008).

- **Search for $B_s \to \mu^+\mu^-$ at D0**
  V. M. Abazov *et al.*, Phys. Rev. D **76**, 092001 (2007).

- **Direct observation of the strange b baryon Xi_b^-**
  V. M. Abazov *et al.*, Phys. Rev. Lett. **99**, 052001 (2007).

- **Measurement of the $Lambda_b^0$ lifetime using semileptonic decays**
  V. M. Abazov *et al.*, Phys. Rev. Lett. **99**, 182001 (2007).

- **Search for stopped gluinos from $p\bar{p}$ collisions at $\sqrt{s}$ = 1.96-TeV**
  V. M. Abazov *et al.*, Phys. Rev. Lett. **99**, 131801 (2007).

- **$Z\gamma$ production and limits on anomalous $ZZ\gamma$ and $Z\gamma\gamma$ couplings in $p\bar{p}$ collisions at $\sqrt{s}$ = 1.96 TeV**
  V. M. Abazov *et al.*, Phys. Lett. B **653**, 378 (2007).

- **Measurement of the Λ_b lifetime in the exclusive decay $\Lambda_b \to J/\psi\Lambda$**
  V. M. Abazov *et al.*, Phys. Rev. Lett. **99**, 142001 (2007).

- **Search for production of single top quarks via flavor-changing neutral currents at the Tevatron**
  V. M. Abazov *et al.*, Phys. Rev. Lett. **99**, 191802 (2007).

- **Lifetime difference and CP-violating phase in the B_s^0 system**
  V. M. Abazov *et al.*, Phys. Rev. Lett. **98**, 121801 (2007).

16.1.8 H1

Articles

- **Three- and Four-jet Production at Low x at HERA**
  F. D. Aaron *et al.*, Eur. Phys. J. C **54**, 389-409 (2008).

- **Measurement of Isolated Photon Production in Deep-Inelastic Scattering at HERA**
  F. D. Aaron *et al.*, Eur. Phys. J. C **54**, 371-387 (2008).

- **Measurement of Deeply Virtual Compton Scattering and its t-dependence at HERA**
  F. D. Aaron *et al.*, Phys. Lett. B **659**, 796 (2008).
- **Dijet Cross Sections and Parton Densities in Diffractive DIS at HERA**
  A. Aktas *et al.*, JHEP **0710**, 042 (2007).
- **Charged Particle Production in High Q2 Deep-Inelastic Scattering at HERA**
  F. D. Aaron *et al.*, Phys. Lett. B **654**, 148 (2007).
- **Measurement of Inclusive Jet Production in Deep-Inelastic Scattering at High Q^2 and Determination of the Strong Coupling**
  A. Aktas *et al.*, Phys. Lett. B **653**, 134 (2007).
- **Search for baryonic resonances decaying to Xi pi in deep-inelastic scattering at HERA**
  A. Aktas *et al.*, Eur. Phys. J. C **52**, 507 (2007).
- **Search for lepton flavour violation in e p collisions at HERA**
  A. Aktas *et al.*, Eur. Phys. J. C **52**, 833 (2007).
- **Tests of QCD factorisation in the diffractive production of dijets in deep-inelastic scattering and photoproduction at HERA**
  A. Aktas *et al.*, Eur. Phys. J. C **51**, 549 (2007).

PhD Thesis

- **Isolated Photon Production in Deep-Inelastic Scattering at HERA**
  C. Schmitz, PhD Thesis, Universität Zürich, October 2007.

Conference contributions and invited talks

- **Isolated Photons at HERA**
  U. Straumann, Europhysics Conference on High Energy Physics, Manchester, England, 19-25 July 2007.
- **Isolated Photons in DIS at HERA (H1)**
  K. Müller, XV International Workshop on Deep-Inelastic Scattering and related Subjects, 16.-10.4.07 Munich, 2007.
- **Hadronic final states and spectroscopy in ep collisions at HERA**
  C. Schmitz, 42nd Rencontres de Moriond on QCD and High Energy Hadronic Interactions, March 17-24 2007, La Thuile, Aosta Valley, Italy, arXiv:0705.4625 (hep-ex).

16.1.9 HERA-B

Articles

- **Measurement of D^0, D^+, D_s^+ and D^{*+} Production in Fixed Target 920 GeV Proton-Nucleus Collisions**
  I. Abt *et al.*, Phys. J. C **52**, 531 (2007).

- **Luminosity determination at HERA-B**
  I. Abt *et al.*, Nucl. Instrum. Meth. A **582**, 401 (2007).

- **Bottom production cross section from double muonic decays of b-hadrons in 920-GeV proton nucleus collision**
  I. Abt *et al.*, Phys. Lett. B **650**, 103 (2007).

- **A measurement of the $\psi' \to J/\psi$ production ratio in 920-GeV proton nucleus interactions**
  I. Abt *et al.*, Phys. J. C **49**, 545 (2007).

- **$K0^*$ and ϕ meson production in proton nucleus interactions at $\sqrt{s}$ = 41.6 GeV**
  I. Abt *et al.*, Eur. Phys. J. C **50**, 315 (2007).

16.1.10 LHCb

PhD Thesis

- **The Trigger Tracker and a Monte Carlo Study of the $B_S \to J/\psi\eta'$ Decay in the LHCb Experiment**
  Dmytro Volyanskyy, PhD Thesis, Universität Zürich, October 2007.

Collaboration notes

- **Design and development of the control board for the LHCb silicon tracker**
  D. Esperante Pereira and A. Vollhardt, CERN-LHCB-2007-153(2008).

- **Updated channel numbering and readout partitioning for the Silicon Tracker**
  M. Needham and O. Steinkamp, CERN-LHCB-2007-137(2007).

- **The LHCb silicon tracker**
  R. P. Bernhard *et al.*, CERN-LHCB-2007-126(2007).

- **Radiation monitoring system for the LHCb inner tracker**
  M. Agari *et al.*, CERN-LHCB-2007-062(2007).

- **The trajectory model for track fitting and alignment**
  E. Bos, M. Merk, G. Raven, E. Rodrigues and J. van Tilburg, CERN-LHCB-2007-008(2007).

- **Selection of the $B_s^0 \to J/\psi(\mu^+\mu^-)\ \eta'(\rho_0\gamma)$ decay at LHCb and its sensitivity to the B_s^0 mixing phase $\phi(s)$**
  D. Volyansky and J. van Tilburg, CERN-LHCB-2007-027(2007).

- **Performance of the track matching**
  M. Needham and J. van Tilburg, CERN-LHCb-2007-020(2007).

16.1.11 Ultracold neutrons

Articles

- **Direct Experimental Verification of Neutron Acceleration by the Material Optical Potential of Solid 2H2**
  I. Altarev *et al.*, Phys. Rev. Lett. **100**, 014801 (2008).

- **Surface characterization of diamond-like carbon for ultracold neutron storage**
  F. Atchison *et al.*, Nucl. Instr. Meth. A **587**, 82-88 (2008).

- **Cold Neutron Energy Dependent Production of Ultracold Neutrons in Solid Deuterium**
  F. Atchison *et al.*, Phys. Rev. Lett. **99**, 262502 (2007).

- **Direct Experimental Limit on Neutron → Mirror-Neutron Oscillations**
  G. Ban *et al.*, Phys. Rev. Lett. **99**, 161603 (2007).

- **Diamond-like carbon coated ultracold neutron guides**
  S. Heule *et al.*, Applied Surface Science **253**, 8245 - 8249 (2007).

- **Measurement of the Fermi potential of diamond-like carbon and other materials**
  F. Atchison *et al.*, Nucl. Instr. Meth. B **260**, 647-656 (2007).

- **Structural characterization of diamond-like carbon coatings for ultracold neutron applications**
  F. Atchison *et al.*, Diamond and Related Materials **16**, 334 (2007).

- **Loss and spinflip probabilities for ultracold neutrons interacting with diamondlike carbon and beryllium surfaces**
  F. Atchison *et al.*, Phys. Rev. C **76**, 044001 (2007).

Conference contributions and invited talks

- **A Direct Experimental Limit on Neutron → Mirror Neutron Oscillations**
  A. Knecht, Annual meeting of the Swiss Physical Society, Geneva, 26. March 2008.

- **A direct experimental limit on neutron → mirror neutron oscillations**
  A. Knecht, International Workshop on Search for Baryon and Lepton Number Violations, 20-22 September 2007, Berkeley, USA.

- **Amorphous carbon coating for ultracold neutron experiments**
  S. Heule, E-MRS Spring meeting, Symposium P, 1. June 2007, Strasbourg, France.

16.1.12 XENON

Talks

- R. Santorelli: **The XENON Dark Matter Project**
  Plenary Talk, Rencontres de Moriond EW 2008, La Thuile, March 6, 2008.

- M. Haffke: **Backgrounds of the XENON10 Experiment at the Gran Sasso Underground Laboratory**
  Contributed Talk, University of Freiburg, March 3, 2008.

- A. Askin: **Material Screening Measurements of XENON100 Detector with GATOR Setup at LNGS**
  Contributed Talk, University of Freiburg, March 3, 2008.

- A. Kish: **Background predictions for the XENON100 Experiment at the Gran Sasso Underground Laboratory**
  Contributed Talk, University of Freiburg, March 3, 2008.

- A. Manalaysay: **The Latest from XENON10 at the Gran Sasso Underground Lab**
  Plenary Talk, Eighth UCLA Symposium, Marina del rey, February 22, 2008.

- L. Baudis: **Direct Dark Matter Searches with Liquid Xenon Detectors**
  Seminar, Karlsruhe Institute of Technology, January 22, 2008.

- L. Baudis: **First results from the XENON10 Experiment at the Gran Sasso Underground Lab and Status of XENON100**
  Plenary Talk, SPP Seminar, CEA Saclay, November 12, 2007.

- E. Tziaferi: **Hunting WIMPs - the XENON experiment**
  Plenary Talk, 11th Meeting of german female physicists, Osnabrück, November 1, 2007.

- L. Baudis: **Results from the XENON10 Experiment**
  Plenary Talk, PSI, October 15, 2007.

- A. Manalaysay: **XENON10 Dark Matter Results: Past, Present, Future**
  Seminar, ETH Zürich, September 14, 2007.

- A. D. Ferella: **Results from the XENON10 Dark Matter search experiment at Gran Sasso Laboratories**
  Plenary Talk, Imperial College London, July 5, 2007.

- L. Baudis: **First results on WIMP-nucleon interactions from the XENON10 Experiment at the Gran Sasso Underground Laboratory**
  Plenary Talk, University of Patras, June 20, 2007.

- A. Manalaysay: **First Results from the XENON10 Experiment at the Gran Sasso Underground Lab**
  Seminar, RWTH Aachen, May 25, 2007.

- A. Manalaysay: **Nuclear Recoil Discrimination in the XENON10 Detector**
  Contributed Talk, Annual April Meeting of the APS, Jacksonville Florida, April 14, 2007.

16.1.13 Miscellaneous

Articles

- **Myonen und Pionen in Teilchenphysik und Anwendungen, 30 Jahre experimentelle Forschung an der Schweizer Mesonenfabrik in Villigen**
  Peter Truöl, Neujahrsblatt der Naturforschenden Gesellschaft in Zürich auf das Jahr 2008, ISSN 0379-1327.

Articles in press

- **Review of Particle Physics**
  C. Amsler *et al.* (Particle Data Group), to appear in Summer 2008.

- **Quark Model**
  C. Amsler, T. DeGrand, B. Krusche, Review of Particle Physics, to appear in Summer 2008.

- **The $\eta(1405)$, $\eta(1475)$, $f_1(1420)$, and $f_1(1510)$**
  C. Amsler and A. Masoni, Review of Particle Physics, to appear in Summer 2008.

- **Note on scalar mesons**
  S. Spanier, N.A. Törnqvist, and C. Amsler, Review of Particle Physics, to appear in Summer 2008.

- **B, D and K decays**
  M. Artuso *et al.*, Eur. J. Phys. (2008), e-Print: arXiv:0801.1833.

- **Flavour physics of leptons and dipole moments**
  M. Raidal and A. van der Schaaf *et al.*, report of the CERN series of workshops on FLAVOUR IN THE ERA OF THE LHC, November 2005 - March 2007, to appear in Eur. Phys. J.

- **Physics at a future Neutrino Factory and super-beam facility**
  A. Bandyopadhyay *et al.* (ISS Physics Working Group), to appear in Reports on Progress in Physics (IOP).

Talks

- L. Baudis: **Direct Dark Matter Searches with Underground Detectors**
  Physics Colloquium, University of Basel, November 23, 2007.

- L. Baudis: **Direct Detection of Dark Matter**
  Plenary Talk, SUSY 2007, Karlsruhe, August 1, 2007.

- L. Baudis: **Direct Detection of Cold Relics with Underground Detectors**
  Plenary Talk, XIXemes Rencontres de Blois, Matter and Energy in the Universe, May 21, 2007.

16.2 Condensed matter

16.2.1 Biological systems

Article

- **Solution to the twin image in holography**
  T. Latychevskaia and H.-W. Fink, Phys. Rev. Lett. 98, 233901 (2007).

Talks

- T. Latychevskaia and Elvira Steinwand: **Hologram presentation**
  experimental presentation, Nacht der Forschung, Zürichhorn, 28 September 2007.
- M. Germann: **Alignment of set of holograms**
  SIBMAR meeting, Jena, Germany, 13 - 15 December 2007.
- T. Latychevskaia: **Theory of hologram alignment method**
  SIBMAR meeting, Jena, Germany, 13 - 15 December 2007.
- H.-W. Fink: **Transmission or no transmission through graphene membranes**
  SIBMAR meeting, Jena, Germany, 13 - 15 December 2007.
- E. Steinwand and J.-N. Longchamp: **Low Energy Electron Coherent Diffraction Microscopy**
  SIBMAR meeting, Jena, Germany, 13 - 15 December 2007.
- T. Latychevskaia: **Holography with Low Energy Electrons, A new Tool for Structural Biology**
  American Physics Society March meeting, New Orleans, March 2008.

Semesterarbeit

- **Freezedryer, Thermal Desorption Spectroscopy**
  M. Thomann, HS 07

Poster

- **On the Energetics of Individual DNA-Molecules**
  C. Escher and H.-W. Fink, ICN+T 07, Stockholm, 2 - 6 Juli 2007.

16.2.2 Phase transitions and superconducting photon detectors

Articles

- **Energy resolution and sensitivity of a superconducting quantum detector**
  A. Semenov, P. Haas, K. Ilin, H.-W. Hübers, M. Siegel, A. Engel, A. Smirnov,
  Physica C, **460-462**, (2007) 1491.
- **Spectral Sensitivity and Spectral Resolution of Superconducting Single-Photon Detectors**
  P. Haas, A. Semenov, H.-W. Hübers, J. Beyer, A. Kirste, T. Schurig, K. Il'in, M. Siegel, A. Engel, A. Smirnov, IEEE Trans. Appl. Supercon., **17**, (2007) 298.
- **Ultra-thin NbN films on Si: crystalline and superconducting properties**
  K. Il'in, R. Schneider, D. Gerthsen, A. Engel, H. Bartolf, A. Schilling, A. Semenov, H.-W. Hübers, B. Freitag, M. Siegel, J. Phys.: Conf. Ser., **97**, (2008) 012045.
- **Temperature- and field-dependence of critical currents in NbN microbridges**
  A. Engel, B. Holger, A. Schilling, K. Il'in, M. Siegel, A. Semenov, H.-W. Hübers,
  J. Phys.: Conf. Ser., **97**, (2008) 012152.

Articles in press

- **Fabrication of metallic structures with lateral dimensions less than 15 nm and $j_c(T)$-measurements in NbN micro- and nanobridges**
  H. Bartolf, A. Engel, A. Schilling, K. Il'lin, M. Siegel, to be published in Phys. C
- **Current-Induced Critical State in NbN Thin-Film Structures**
  K. Il'in, M. Siegel, A. Engel, H. Bartolf, A. Schilling, A. Semenov, H.-W. Hübers,
  to be published in J. Low Temp. Phys.

Master thesis

- **Effect of vortex shaking on the resistivity of type-II superconductors**
  Stefan J. Menzi, Physik-Institut Universität Zürich, 2007.

Contributed Conference Presentations

- **Fabrication of metallic structures with spatial dimensions of about 10 nm and $j_c(T)$ measurements in NbN micro- and nanobridges (poster)**
  H. Bartolf, A. Engel, A. Schilling, K. Il'in, M. Siegel, Vortex Matter in Nanostructured Superconductors (Vortex V), Rhodes, Greece, 8.-14.9.2007.
- **Temperature- and Field-Dependence of Critical Currents in NbN Microbridges (poster)**
  A. Engel, H. Bartolf, A. Schilling, K. Il'in, M. Siegel, A. Semenov, H.-W. Hübers, European Conference for Applied Superconductivity EUCAS 2007, Brussels, Belgium, 16.-20.9.2007.
- **Magnetic Vortices in Superconducting Photon Detectors**
  A. Engel, H. Bartolf, A. Schilling, K. Il'in, M. Siegel, P. Haas, A. Semenov, H.-W. Hübers,
  Single Photon Workshop 2007, Torino, Italy, 25.-28.9.2007.

- **Temperature- and Field-Dependence of Critical Currents in NbN Microbridges (poster)**
  A. Engel, H. Bartolf, A. Schilling, K. Il'in, M. Siegel, A. Semenov, H.-W. Hübers, 2007 Swiss Workshop on Materials with Novel Electronic Properties, Les Diablerets, Switzerland, 28.-30.9.2007.

- **Process development for the fabrication of metallic structures with lateral dimensions of about 10 nm and superconducting nm-sized meander structures (poster)**
  H. Bartolf, A. Engel, A. Schilling, K. Il'in, M. Siegel, 2007 Swiss Workshop on Materials with Novel Electronic Properties, Les Diablerets, Switzerland, 28.-30.9.2007.

- **Unexpected temperature-dependence of the critical current in NbN-microbridges (poster)**
  A. Engel, H. Bartolf, L. Gómez, A. Schilling, K. Il'in, M. Siegel, A. Semenov, H.-W. Hübers, Frühjahrstagung der Deutschen Physikalischen Gesellschaft, Berlin, Deutschland, 25.-29.2.2008.

- **Fabrication process of superconducting nanostructures and $R(T, B)$ measurements of their electronic phase transition (poster)**
  H. Bartolf, A. Engel, L. Gómez, A. Schilling, K. Il'in, M. Siegel, Swiss Physical Society Meeting, Geneva, Switzerland, 26.-27.3.2008.

Invited Lectures

- A. Schilling: **Phase diagrams of superconductors, populated with peaks, steps and crossovers**
  Highly correlated Electron Systems and Superconductivity Symposium in Honor of Prof. Hans-Ruedi Ott, Zürich, Switzerland, 11.05.07.

- A. Schilling: **Transition-metal oxide perovskites: still any hope for new superconductors?**
  MaNEP Project 4 Internal Workshop 2008, Neuchâtel, Switzerland, 16.01.08.

- A. Engel: **Superconducting Nanostructures – Single-Photon Detector**
  Manep Project 5 Internal Workshop 2008, Neuchâtel, Switzerland, 17.1.2008.

16.2.3 Superconductivity and Magnetism

Articles

- **Influence of Ti^{4+} on the magnetic state of $CaRu_{1-x}Ti_xO_3$**
  A. Zorkovská, A. Baran, I. Bradarić, I. Savić, J. Šebek, E. Šantavá, D. Marinčev, S. Kohout, H. Keller, and A. Feher, Journal of Magnetism and Magnetic Materials **316**, e699-e702 (2007).

- **Polaron Effects in High-Temperature Cuprate Superconductors**
  A. Bussmann-Holder and H. Keller, in **Polarons in Advanced Materials**, ed. A.S. Alexandrov (Springer Series in Materials Science 103, Canopus Publishing, Bristol 2007), pp. 599-621.

- **Real and marginal isotope effects in cuprate superconductors**
  A.R. Bishop, A. Bussmann-Holder, O.V. Dolgov, A. Furrer, H. Kamimura, H. Keller, R. Khasanov, R.K. Kremer, D. Manske, K.A. Müller, and A. Simon,
  J. Supercond. Nov. Magn. **20**, 393-396 (2007).

- **High T_c Superconductors and Related Transition Metal Oxides**
  A. Bussmann-Holder and H. Keller, editors (Springer, Berlin, 2007).

- **Electronic phase separation and unusual isotope effects in $La_{2-x}Sr_xCuO_4$ observed by electron paramagnetic resonance**
  A. Shengelaya, B.I. Kochelaev, K. Conder, and H. Keller,
  in **High T_c Superconductors and Related Transition Metal Oxides**, eds. A. Bussmann-Holder and H. Keller (Springer-Verlag, Berlin, Heidelberg, 2007), pp. 287-302.

- **Two types of $H_{c_2}(T)$ dependences in $Bi_2Sr_2Ca_{1-x}Y_xCu_2O_{8+\delta}$ with different Yttrium content**
  I.L. Landau and H. Keller, Physica C **458**, 38-42 (2007).

- **Surface nanomagnetism of La_2CuO_4 particles**
  R.V. Yusupov, V. Kabanov, D. Mihailovic, K. Conder, H. Keller, and K.A. Müller,
  Physica C **460-462**, 801-802 (2007).

- **Oxygen isotope effect on the polaronic infrared photo-induced absorption spectra of La_2CuO_4**
  R.V. Yusupov, T. Mertelj, D. Mihailovic, K. Conder, H. Keller, and K.A. Müller,
  Physica C **460-462**, 920-921 (2007).

- **On the interpretation of muon-spin-rotation experiments in the mixed state of type-II superconductors**
  I.L. Landau and H. Keller, Physica C **466**, 131-141 (2007).

- **Spontaneous ferromagnetic spin ordering at the surface of La_2CuO_4**
  R.V. Yusupov, V.V. Kabanov, D. Mihailovic, K. Conder, K. A. Müller, and H. Keller,
  Phys. Rev. B **76**, 024428-1-9 (2007).

- **Entscheidende Rolle des Gitters**
  A. Bussmann-Holder, H. Keller, and K.A. Müller, Physik Journal **6**, 16 (2007).

- **Study of the critical current and irreversibility line of $Bi_2Sr_2CaCu_2O_8$ thin films irradiated with low-energy Co^+ and Fe^+ ions**
  N. Panarina, A. Bukharaev, Yu. Talanov, V. Petukhov, G. Gumarov, A. Validov, and R. Khasanov,
  Physica C **467**, 85-90 (2007).

- **Dual character of the electronic structure in $YBa_2Cu_4O_8$: conduction bands of CuO_2 planes and CuO chains**
  T. Kondo, R. Khasanov, J. Karpinski, S.M. Kazakov, N.D. Zhigadlo, T. Ohta, H.M. Fretwell, A.D. Palczewski, J.D. Koll, J. Mesot, E. Rotenberg, H. Keller, and A. Kaminski,
  Phys. Rev. Lett. **98**, 157002-1-4 (2007).

- **On the occurrence of Berezinskii-Kosterlitz-Thouless behavior in highly anisotropic cuprate superconductors**
  T. Schneider, Europhys. Lett. **78**, 47003-1-4 (2007).

- **Evidence for three-dimensional XY critical properties in underdoped $YBa_2Cu_3O_{7-\delta}$**
  T. Schneider, Phys. Rev. B **75**, 174517-1-10 (2007).

- **Magnetic-field-induced 3D-to-1D crossover in $La_{0.9}La_{0.1}CuO_2$**
  T. Schneider, Europhys. Lett. **79**, 57005-1-4 (2007).

- **Vortex states and magnetic anisotropy in single-crystal $La_{2x}Sr_xCuO_4$ studied by torque magnetometry**
  S. Kohout, T. Schneider, J. Roos, H. Keller, T. Sasagawa, and H. Takagi,
  Phys. Rev. B **76**, 064513-1-7 (2007).

- **On the superconductivity in hole doped cuprates**
  K.A. Müller, J. Phys. C: Condens. Matter **19**, 251002-1-12 (2007).

- **^{139}La NMR and NQR investigations of the superconductor $LaBa_2Cu_3O_{7-\delta}$**
  S. Strässle , J. Roos , M. Mali , K. Conder , E. Pomjakushina, and H. Keller,
  Physica C **460-462**, 890-891 (2007).

- **^{11}B NMR study of single-crystal MgB_2 in the normal conducting phase**
  S. Strässle , J. Roos , M. Mali , H. Keller, and J. Karpinski, Physica C **466**, 168-173 (2007).

- **Electroluminescence in $SrTiO_3$:Cr single-crystal nonvolatile memory cells**
  S.F. Alvarado, F. La Mattina, and J.G. Bednorz, Appl. Phys. A **89**, 85-89 (2007).

- **Multiple Gap Symmetries for the Order Parameter of Cuprate Superconductors from Penetration Depth Measurements**
  R. Khasanov, S. Strässle, D. Di Castro, T. Masui, S. Miyasaka, S. Tajima, A. Bussmann-Holder, and H. Keller, Phys. Rev. Lett. **99**, 237601-1-4 (2007).

- **In-plane magnetic penetration depth λ_{ab} in $Ca_{2-}Na_xCuO_2Cl_2$: Role of the apical sites**
  R. Khasanov, N.D. Zhigadlo, J. Karpinski, and H. Keller, Phys. Rev. B **76**, 094505-1-8 (2007).

- **Formation of Hydrogen Impurity States in Silicon and Insulators at Low Implantation Energies**
  T. Prokscha, E. Morenzoni, D.G. Eshchenko, N. Garifianov, H. Glückler, R. Khasanov, H. Luetkens, and A. Suter, Phys. Rev. Lett **98**, 227401-1-4 (2007).

- **Two-gap superconductivity in the cuprate superconductor $La_{1.83}Sr_{0.17}CuO_4$**
  R. Khasanov, A. Shengelaya, A. Bussmann-Holder, and H. Keller,
  Invited paper to the volume "High Tc Superconductors and Related Transition Metal Oxides", eds. A. Bussmann-Holder and H. Keller (Springer, Berlin, 2007), pp. 177-190.

- **μSR studies of hydrogen-bonded ferroelectrics and antiferroelectrics**
  E. Morenzoni, H. Luetkens, A. Suter, D. Eshchenko, R. Khasanov, A. Amato, T. Prokscha, and R. Scheuermann, Physica B **388**, 274-277 (2007).

- **$s-$wave symmetry along the c-axis and $s+d$ in-plane superconductivity in bulk $YBa_2Cu_4O_8$**
  R. Khasanov, A. Shengelaya, A. Bussmann-Holder, J. Karpinski, H. Keller, and K.A. Müller,
  J. Supercond. Nov. Magn. **21**, 81-85 (2008).

- **Correlation between the transition temperature and the superfluid density in BCS superconductor NbB_{2+x}**
  R. Khasanov, A. Shengelaya, A. Maisuradze, D. Di Castro, R. Escamilla, and H. Keller,
  Phys. Rev. B **77**, 064506-1-9 (2008).

- **Finite gap behaviour in the superconductivity of the 'infinite layer' n-doped high-T_c superconductor $Sr_{0.9}La_{0.1}CuO_2$**
  J.S. White, E.M. Forgan, M. Laver, P.S. Häfliger, R. Khasanov, R. Cubitt, C.D. Dewhurst, M.-S. Park, D.-J. Jang, H-G. Lee, and S.-I. Lee, J. Phys.: Condens. Matter **20**, 104237-1-5 (2008).

- **Probing superconductivity in MgB_2 confined to magnetic field tuned cylinders by means of critical fluctuations**
  S. Weyeneth, T. Schneider, N.D. Zhigadlo, J. Karpinski, and H. Keller,
  J. Phys.: Condens. Matter **20**, 135208-1-8 (2008).

- **Synthesis and bulk properties of oxychloride superconductor $Ca_{2-x}Na_xCuO_2Cl_2$**
  N.D. Zhigadlo, J. Karpinski, S. Weyeneth, R. Khasanov, S. Katrych, P. Wägli, and H. Keller, J. Phys.: Conf. Ser. **97**, 012121-1-6 (2008).

- **Resonant soft x-ray powder diffraction study to determine the orbital ordering in A-site-ordered $SmBaMn_2O_6$**
  M. Garca-Fernández, U. Staub, Y. Bodenthin, S.M. Lawrence, A.M. Mulders, C.E. Buckley, S. Weyeneth, E. Pomjakushina, and K. Conder, Phys. Rev. B **77**, 060402(R)-1-4 (2008).

- **Universal correlations of isotope effects in $Y_{1-x}Pr_xBa_2Cu_3O_{7-\delta}$**
  R. Khasanov, S. Strässle, K. Conder, E. Pomjakushina, A. Bussmann-Holder, and H. Keller, Phys. Rev. B **77**, 104530-1-5 (2008).

Article in press

- **Depth dependent spin dynamics of canonical spin glass films: A low-energy muon spin rotation study**
  E. Morenzoni, H. Luetkens, T. Prokscha, A. Suter, S. Vongtragool, F. Galli, M.B.S. Hesselberth, N. Garifianov, and R. Khasanov, to appear in Phys. Rev. Lett.

Conference reports

- **Depth dependent μSR studies of YBCO/PBCO/YBCO tri-layers**
  B.M. Wojek, E. Morenzoni, D.G. Eshchenko, T. Prokscha, A. Suter, E. Koller, E. Treboux, Ø. Fischer, and H. Keller, NCCR MaNEP - Review Panel Meeting, Genève, June 14, 2007.

- **Evidence of charge transfer processes in resistive memory switching of Cr-doped $SrTiO_3$**
  F. La Mattina, S. F. Alvarado, J.G. Bednorz, and H. Keller,
  6th PSI Summer School, Zuoz, August 18-25, 2007.

- **Superconductivity and magnetism in cuprate tri-layers**
  B.M. Wojek, E. Morenzoni, D.G. Eshchenko, A. Suter, T. Prokscha, E. Koller, E. Treboux, Ø. Fischer, and H. Keller,
  6th PSI Summer School on Condensed Matter Research, Zuoz, August 18-25, 2007.

- **Depth resolved investigations of superconductivity and magnetism in cuprate multilayers**
  E. Morenzoni, B.M. Wojek, D.G. Eshchenko, A. Suter, T. Prokscha, E. Koller, E. Treboux, Ø. Fischer, and H. Keller, Swiss Workshop on Materials with Novel Electronic Properties, Les Diablerets, 28-30 September, 2007.

- **^{139}La NMR/NQR study of the cuprate superconductor $LaBa_2Cu_3O_{7-\delta}$**
  S. Strässle, J. Roos, M. Mali, K. Conder, E. Pomjakushina, and H. Keller, Swiss Workshop on Materials with Novel Electronic Properties, Les Diablerets, 28-30 September, 2007.

- **EPR study of Oxygen Isotope Effect on spin lattice relaxation rate of Yb^{3+} in $YBa_2Cu_3O_x$**
  A. Maisuradze, A. Shengelaya, B.I. Kochelaev, E. Pomjakushina, K. Conder, K.A. Müller, and H. Keller, Swiss Workshop on Materials with Novel Electronic Properties, Les Diablerets, 28-30 September, 2007.

- **Electron traps and resistive memory switching in $SrTiO_3$**
  F. La Mattina, S. F. Alvarado, J. G. Bednorz, S. Karg, A. Shengelaya, and H. Keller,

Swiss Workshop on Materials with Novel Electronic Properties, Les Diablerets, 28-30 September, 2007.

- **Superconductivity confined to magnetic field tuned cylinders by means of critical fluctuations**
S. Weyeneth, T. Schneider, N.D. Zhigadlo, J. Karpinski, and H. Keller, Swiss Workshop on Materials with Novel Electronic Properties, Les Diablerets, 28-30 September, 2007.

- **Superconductivity and magnetism in cuprate multi-layers**
B.M. Wojek, E. Morenzoni, D.G. Eshchenko, A. Suter, T. Prokscha, E. Koller, E. Treboux, Ø. Fischer, and H. Keller, Annual meeting of the Swiss Physical Society, Genève, March 26-27, 2008.

- **^{139}La NMR/NQR study of the cuprate superconductor $LaBa_2Cu_3O_{7-\delta}$**
S. Strässle, M. Mali, B. Graneli, J. Roos, K. Conder, E. Pomjakushina, and H. Keller,
Annual meeting of the Swiss Physical Society, Genève, March 26-27, 2008.

- **Evidence of coexisting superconducting and magnetic phases in $YBa_2Cu_3O_x$ near antiferromagnetic to superconducting boundary detected by Yb^{3+} EPR probe**
A. Maisuradze, A. Shengelaya, B.I. Kochelaev, E. Pomjakushina, K. Conder, and H. Keller, Annual meeting of the Swiss Physical Society, Genève, 26-27 March, 2008.

- **Superconductivity confined to magnetic field tuned cylinders by means of critical fluctuations**
S. Weyeneth, T. Schneider, N.D. Zhigadlo, J. Karpinski, and H. Keller,
Annual meeting of the Swiss Physical Society, Genève, 26-27 March, 2008.

Invited lectures

- H. Keller: **Unconventional isotope effects in cuprate superconductors - are they real?**
Dynamical Energy Landscapes and Functional Systems, Port Jefferson, New York, U.S.A., May 23-26, 2007.

- R. Khasanov: **Evidence for complex order parameters in cuprate superconductors**
Dynamical Energy Landscapes and Functional Systems, Port Jefferson, New York, U.S.A., May 23-26, 2007.

- R. Khasanov: **μSR observation of multiple order parameters in cuprate superconductors**
LMU seminar, PSI, 16 August, 2007.

- H. Keller: **Introduction to superconductivity**
Correlated Electron Materials, 6th PSI Summer School on Condensed Matter Research, Lyceum Alpinum, Zuoz, Switzerland, August 18-25, 2007.

- H. Keller: **Experimental evidence for mixed order parameter symmetries in cuprate superconductors**
5th CoMePhS Meeting, University of Groningen, Groningen, The Netherlands, September 13-14, 2007.

- R. Khasanov: **Evidence for complex order parameter in cuprate high-temperature superconductors**
Swiss Workshop on Materials with Novel Electronic Properties, Les Diablerets, 28-30 September, 2007.

- H. Keller: **Unconventional isotope effects in cuprate superconductors - what do they tell us?**
High-temperature Superconductivity in Cuprates Original Concept and Developments, Tbilisi, Georgia, 8-11 October, 2007.

- R. Khasanov: **Multiple order parameters in cuprate superconductors**
  Conference on High-Temperature Superconductivity in Cuprates: Original Concept and New Developments, Tbilisi, Georgia, 8-11 October, 2007.

- T. Schneider: **Magnetic field induced 3D to 1D crossover in type-II superconductors**
  Conference on High-Temperature Superconductivity in Cuprates: Original Concept and New Developments, Tbilisi, Georgia, 8-11 October, 2007.

- A. Maisuradze: **Investigation of relaxation mechanisms and insulator to superconductor transition of $YBa_2Cu_3O_x$ by Yb^{3+} EPR probe**
  Conference on High-Temperature Superconductivity in Cuprates: Original Concept and New Developments, Tbilisi, Georgia, 8-11 October, 2007.

- H. Keller: **Unconventional isotope effects and multicomponent superconductivity in cuprates**
  International Symposium on Lattice Effects in Cuprate High Temperature Superconductors - Spin, phonon or third way?, National Institute of Advanced Industrial Science and Technology (AIST), Tsukuba, Japan, October 31 - November 3, 2007.

- H. Keller: **Hochtemperatur-Supraleitung - 20 Jahre nach der Entdeckung**
  Physikalische Gesellschaft Zürich, ETH Zürich, Zürich, Switzerland, November 22, 2007.

- H. Keller: **Unconventional isotope effects in cuprate superconductors - what do they tell us?**
  PSI Condensed Matter Colloquium, Paul Scherrer Institute, Villigen, Switzerland, November 30, 2007.

- R. Khasanov: **Partially superconducting "Fermi surface" in $(BiPb)_2(SrLa)_2CuO_{6+\delta}$: competition between superconductivity and pseudogap**
  MICuO: Metal Insulator transition in Cuprates, Parma (Italy), March 18, 2008.

- Alexander Maisuradze: **Analysis of μSR spectra in the vortex state of type-II superconductors**
  Seminar at Paul Scherrer Institut, Villigen, Switzerland, 28 February 2008.

- H. Keller: **Von Positronen zu Myonen**
  Mini-Symposium (Dr. Dierk Herlach), Paul Scherrer Institute, Villigen, Switzerland, March 28, 2008.

16.2.4 Surface Physics

Articles

- **Boron nitride nanomesh: functionality from a corrugated monolayer**
  S. Berner, M. Corso, R. Widmer, O. Groening, R. Laskowski, P. Blaha, K. Schwarz, A. Goriachko, H. Over, S. Gsell, M. Schreck, H. Sachdev, T. Greber, J. Osterwalder,
  Angew. Chem. Int. Ed. 46, 5115-5119 (2007).

- **Electrolytic in situ STM investigation of h-BN nanomesh**
  R. Widmer, S. Berner, O. Groening, T. Brugger, J. Osterwalder, T. Greber,
  Electrochemistry Commun. 9, 2484-2488 (2007).

- **Hidden surface states on pristine and H-passivated Ni(111): angle-resolved photoemission and density-functional calculations**
  J. Lobo-Checa, T. Okuda, M. Hengsberger, L. Patthey, T. Greber, P. Blaha, J. Osterwalder,
  Phys. Rev. B 77, 075415-1-8 (2008).

- **Photoemission momentum mapping and wave function analysis of surface and bulk states on flat Cu(111) and stepped Cu(443) surfaces: a two-photon photoemission study**
  M. Hengsberger, F. Baumberger, H. J. Neff, T. Greber, J. Osterwalder,
  Phys. Rev. B 77, 085425-1-10 (2008).

- **Electronic structure at the C_{60}/metal interface: an angle-resolved photoemission and first principles study**
  A. Tamai, A. P. Seitsonen, F. Baumberger, M. Hengsberger, Z.-X. Shen, T. Greber, J. Osterwalder,
  Phys. Rev. B 77, 075134-1-8 (2008).

- **Surface trapping of atoms and molecules with dipole rings**
  H. Dil, J. Lobo-Checa, R. Laskowski, P. Blaha, S. Berner, J. Osterwalder, T. Greber,
  Science 319, 1824-1826 (2008).

Articles in press

- **Comparative electron diffraction study of the diamond nucleation layer on Ir(001)**
  S. Gsell, S. Berner, T. Brugger, M. Schreck, R. Brescia, M. Fischer, J. Osterwalder, B. Stritzker,
  Diamond Relat. Mater., in press (2008).

- **Quantitative vectorial spin analysis in ARPES: Bi/Ag(111) and Pb/Ag(111)**
  F. Meier, H. Dil, J. Lobo-Checa, L. Patthey, J. Osterwalder, Phys. Rev. B, in press (2008).

Master and Bachelor theses

- **Alignment and characterisation of an optical parametric amplifier**
  Silvan Roth, Bachelor Thesis, Physik-Institut, Universität Zürich, 2007.

- **Towards silicon nanowire field-effect transistors**
  Martin Enderlein, Master Thesis, Physik-Institut, Universität Zürich, 2008
  (work carried out at the IBM Research Laboratory, Rüeschlikon).

Contributed conference presentations

- **Corannulene molecules on a magnetic surface**
  L. Brandenberger, Swiss Molecules on Surfaces (molCHsurf) Discussion Meeting, Bern, 19.6.07.

- **Catching molecules in nanomesh pores**
  S. Berner, Swiss Molecules on Surfaces (molCHsurf) Discussion Meeting, Bern, 19.6.07.

- **Nanomesh in liquids (Poster)**
  T. Greber, Bunsen Discussion Meeting "Out of the Vacuum", Heidelberg, Germany, 29.6.07.

- **Boron nitride nanomesh: functionality from a corrugated monolayer**
  S. Berner, 17th International Vacuum Congress, Stockholm, Sweden, 3.7.07.

- **Hidden surface states on Ni(111) pristine and hydrogen passivated surfaces**
  J. Lobo-Checa, 17th International Vacuum Congress, Stockholm, Sweden, 6.7.07.
- **Quantum size effects and Rashba splitting in thin metal films**
  J. H. Dil, SLS Symposium on Surface Science, PSI, Villigen, 3.7.07.
- **Boron nitride nanomesh: functionality from a corrugated monolayer**
  S. Berner, International Conference on Trends in Nanotechnology 2007, San Sebastian, Spain, 5.9.07.
- **Determining the nanoscale energy landscape of the h-BN nanomesh (Poster)**
  J. H. Dil, International Conference on Trends in Nanotechnology 2007, San Sebastian, Spain, 5.9.07.
- **Rashba spin-orbit splitting of quantum well states in thin Pb layers (Poster)**
  J. H. Dil, SLS Users Meeting, PSI, Villigen, 11.9.07.
- **The power of COPHEE**
  J. H. Dil, SLS Workshop on Spectroscopy of Novel Materials, Rigi, 10.1.08.
- **Trapping molecules in dipole rings**
  T. Greber, Symposium on Surface Science 2008, St. Christoph, Austria, 4.3.08.
- **Understanding and tuning the electron spin on surfaces**
  J. H. Dil, Symposium on Surface Science 2008, St. Christoph, Austria, 7.3.08.
- **Spin-orbit splitting of quantum well states in ultrathin Pb layers (Poster)**
  J. H. Dil, Swiss Physical Society Meeting, Geneva, 26./27.3.08.
- **Quantitative vectorial spin analysis in spin and angle resolved photoemission: Bi/Ag(111) and Pb/Ag(111) (Poster)**
  F. Meier, Swiss Physical Society Meeting, Geneva, 26./27.3.08.

Invited lectures

- M. Hengsberger: **(Brief) review of techniques and recent progress in laser-based photoelectron spectroscopy**
  International Seminar and Workshop on Strong Correlations and Angle-Resolved Photoelectron Spectroscopy (CORPES 07), MPI für Physik komplexer Systeme, Dresden, Germany, 7.5.07.
- M. Hengsberger: **Time-resolved photoelectron spectroscopy from h-BN/Ni(111)**
  International Seminar and Workshop on Strong Correlations and Angle-Resolved Photoelectron Spectroscopy (CORPES 07), MPI für Physik komplexer Systeme, Dresden, Germany, 8.5.07.
- J. Osterwalder: **Robust nanotemplates from hexagonal boron nitride monolayers on transition metal surfaces**
  Seminar, IBM Research Laboratory, Rüeschlikon, 22.5.07.
- T. Greber: **Single layer hexagonal boron nitride: from flat films to nanomesh**
  Chemie Kolloquium, Universität Hannover, Germany, 25.6.07.
- J. Osterwalder: **Monolayer films of hexagonal boron nitride on transition metal surfaces**
  17th International Vacuum Congress, Stockholm, Sweden, 5.7.07.

- T. Greber: **Formation of single sheet boron nitrides on transition metals**
  Workshop on Elementary Reactive Processes at Surfaces (ERPS 07), Donostia, San Sebastian, Spain, 30.8.07.
- J. H. Dil: **Rashba spin-orbit splitting in Pb quantum well states and on Bi/Ag(111) and Pb/Ag(111) surface alloys**
  Seminar, Arbeitsgruppe S. Blügel, Institut für Festkörperforschung, Forschungszentrum Jülich, Germany, 29.10.07.
- T. Greber: **Single sheets of hexagonal boron nitride: from flat layers to nanomesh**
  Kolloquium, Departement für Chemie und Biochemie, LMU München, 19.2.08.
- T. Greber: **PEARL: an update**
  SLS Quo Vadis Meeting on Magnetism and Magnetic Materials, Unterwasser, 11.1.08.
- T. Greber: **Hexagonal boron nitride nanomesh as a template for molecular arrays**
  Marie-Curie Network NANOMATCH Workshop, Universität Zürich, 13.2.08.

16.2.5 Miscellaneous

Article

- **Stability of Skyrmions in discrete arrays of spins with Heisenberg and truncated RKKY-interaction and single-spin anisotropy**
  Franz Waldner, Journal of Magnetism and Magnetic Materials **320** (2008) 379-385.

Invited lecture

- H. Keller: **Was ist Licht?**
  Kinderuniversität, Universität Zürich, Zürich, Switzerland, May 9, 2007.